UNIVERSITY OF OKLAHOMA

GRADUATE COLLEGE

INTERFERENCE MITIGATION USING RECONFIGURABLE RF COMPONENTS

A THESIS

SUBMITTED TO THE GRADUATE FACULTY

in partial fulfillment of the requirements for the

Degree of

MASTER OF SCIENCE

By

RYAN BROWN
Norman, Oklahoma
2017

INTERFERENCE MITIGATION USING RECONFIGURABLE RF COMPONENTS

A THESIS APPROVED FOR THE
SCHOOL OF ELECTRICAL AND COMPUTER ENGINEERING

BY

Dr. Hjalti Sigmarsson, Chair

Dr. Jorge Salazar-Cerreño

Dr. Mark Yeary

Dedicated to my wife and children

JMJ + AMDG

Acknowledgements

I would like to thank Tinker Air Force Base and the Long-Term Training Program for funding my studies at the University of Oklahoma. I would like to thank my advisor, Dr. Hjalti Sigmarsson, for the opportunity to study with him and for all of his guidance and help during this effort. I would also like to thank Dr. Jorge Salazar and Dr. Mark Yeary for serving on my committee and for their guidance. I would like to thank Dr. Jessica Ruyle for her guidance and suggestions regarding the antenna-related portions of this work. I would like to thank Jason Brand, Nicholas Peccarelli, Christopher Walker, Garrett Robinson, Dr. Nafati Aboserwal, and Dr. Shahrokh Saeedi for their helpful suggestions and discussions, and for their invaluable help during the fabrication and measurement stages of this project. I would also like to thank Rogers Corporation for providing the microwave substrates used in this work. I would like to thank my parents for the love and support they have given me over the years, and for instilling in me a love for learning and discovery. Finally, I would like to thank my wife, Maddie, and my children for their unfailing love, patience, and support; I know this journey has been long and trying, and I could not have achieved this without all of you.

Table of Contents

List of Tables

List of Figures

Abstract

The need for efficient spectrum management continues to grow as the number of users of wireless technologies continues to increase. Solutions to this problem include cognitive radio systems, which aim to adaptively reduce interference by seeking less-crowded frequency bands, and smart antenna systems, which attempt to reduce interference by directing energy toward desired users and placing nulls in the directions of interferers.

While seeking to adapt to the challenges posed by frequency spectrum crowding, designers are also tasked with minimizing the size, weight, power consumption, and cost of components. Minimizing these parameters helps manufacturers to reduce their costs and provide more capable systems to their users, which is important in both the consumer and military domains.

This work investigates the design of a tunable filtering antenna for interference mitigation applications. The filtering antenna concept offers several benefits over traditional antennas, such as increased impedance bandwidth, the elimination of reflections at device ports, and reduced size. The design methods for filtering antennas presented in the literature are reviewed and used. A new filtering antenna is developed which achieves center frequency tuning in the S-band, making it a candidate for integration into cognitive radio systems. The realized filtering antenna provides increased impedance bandwidth and aids in maintaining input impedance matching across the tuning range when compared to the reference antenna.

Chapter 1

Introduction

The field of electromagnetics has given rise to many technologies that are ubiquitous in the modern world. By far, the two that are most common in daily life are communications and remote sensing. Wireless communication enables us to bridge distances that once presented almost absolute separation from friends and family. Remote sensing allows us to monitor the weather, study distant planets, manage air traffic, and secure our airspace from hostile forces.

As in every industry, designers in the remote sensing and communications domains want to minimize size, weight, power consumption, and cost (SWaP-C) without sacrificing performance. Reducing SWaP-C helps to lower prices of systems and enables device miniaturization, among many other benefits. In particular, much work has been done to improve the components in radio frequency (RF) front-ends to reduce costs and meet increasingly tighter size constraints. RF front-ends, as illustrated in Figure 1.1, provide the interface between the signal processing back-end of an RF system and the environment outside the system.

As shown in Figure 1.1, the front-end generally includes all the components from the antenna up to the baseband system: the antenna, filter, amplifier, and mixer. While attempting to minimize SWaP-C, RF front-end component designers must also deal will the problem of frequency spectrum crowding. When multiple

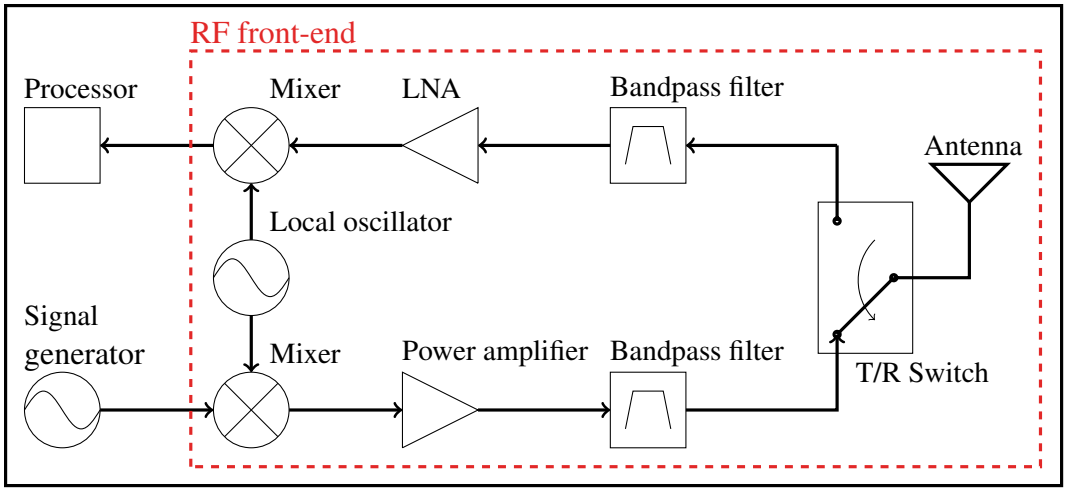

Figure 1.1: Generic RF system block diagram

systems operate in a frequency band, a given system must distinguish signals of interest (SOI) from signals not of interest (SNOI) [1]. Signals from other systems and users interfere with the signals of interest, which reduces system performance [1]. As more users vie for limited bandwidth, spectrum management frameworks, such as smart antenna systems and cognitive radio, are becoming more necessary and common [1], [2]. Smart antenna systems seek to reduce interference by re-configuring their antenna patterns to direct more energy toward signals of interest and place nulls in the direction of interferers [1]. Cognitive radio refers to radio systems that can sense the frequency spectrum and adapt their parameters to meet some pre-determined performance criteria [2]. Cognitive radio systems that change their operating frequency will seek frequency bands were there is less traffic; such systems typically use RF front-ends with wider bandwidth than is required by the signal so that the operating frequency can be selected from a wide range. However, the wideband front-end raises the noise floor of the system, as noise is directly proportional to bandwidth [3]. Tunable front-end components with bandwidths comparable to the signal bandwidth can be employed to remedy this problem and enhance the capabilities of cognitive radio systems.

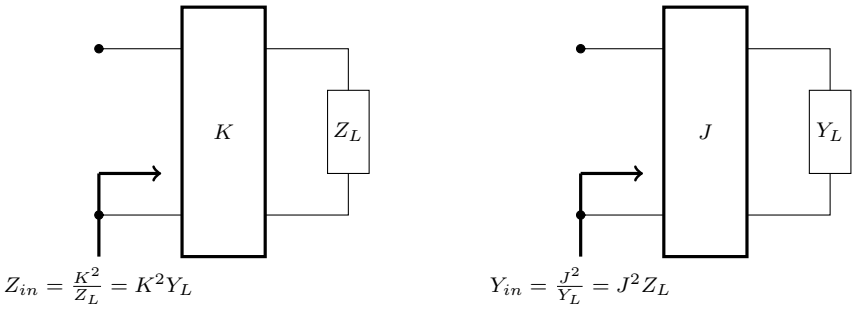

Figure 1.2: Inverter representations and functions [5]. (a) Impedance inverter. (b) Admittance inverter.

Traditionally, the filter and antenna of a system are impedance-matched to transmission lines with standard characteristic impedances, such as 50 Ω or 75 Ω. Generally, there is some impedance mismatch between the filter and the line and the antenna and the line; these mismatches cause signal reflection and losses in the system. One of the concepts that has emerged from the need for reduced SWaP-C is the filtering antenna, or filtenna [4]. A filtenna eliminates the connection between the filter and antenna, thereby reducing the losses in the RF system and potentially reducing the required space. To demonstrate the concept of a filtenna, some background theory from filters and antennas is necessary. A filter network can be realized using lumped-element resonators connected to each other in series or shunt and finally to a load impedance. The resonators consist of inductors and capacitors in either series or parallel combinations. Filter response synthesis often results in inductor and capacitor values that are not physically realizable; thus, the circuit components known as inverters are needed. Inverters, as their name implies, convert impedance to admittance (K inverters), or admittance to impedance (J inverters) [5]. This idea is illustrated in Figure 1.2.

Inverters can help convert unrealizable lumped-element values into realizable ones. More details on inverters, such as their use in filters and their realization,

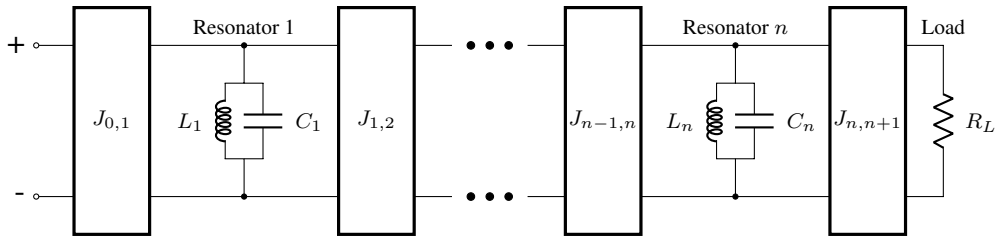

Figure 1.3: Filter example: shunt resonators consisting of parallel inductors and capacitors connected with J inverters. [5]

will be provided in Chapter 2. A filter network can be represented as resonators of a single type (series or parallel) connected to each other and to input and output ports with inverters, as shown in Figure 1.3. The resonators of the filter provide the poles of the filter frequency response. The inverters control the transfer of energy between resonators and provide matching between the impedance of the filter and the input and output ports.

The aspect of antenna theory that is important to filtennas is the circuit-model representation of an antenna. An antenna can be represented as either a series or parallel resistor-inductor-capacitor (RLC) circuit. The resistance represents the loss resistance and the radiation resistance of the antenna. These are the equivalent resistances in which the ohmic power loss and radiated power loss occur [6]. The circuit model of an antenna indicates that antennas can be resonant structures whose resonant frequencies are determined by the inductive and capacitive components of the antenna's impedance.

The concept of a filtenna, defined by Abbaspour-Tamijani *et al.* in [4], is illustrated in Figure 1.4: the final resonator, output inverter, and load of a filter network are replaced with a radiating element. The resonator is provided by the resonant component of the antenna, while the load is provided by the antenna's resistance [4].

One of the key concepts of filtennas is that the antenna, acting as a resonator,

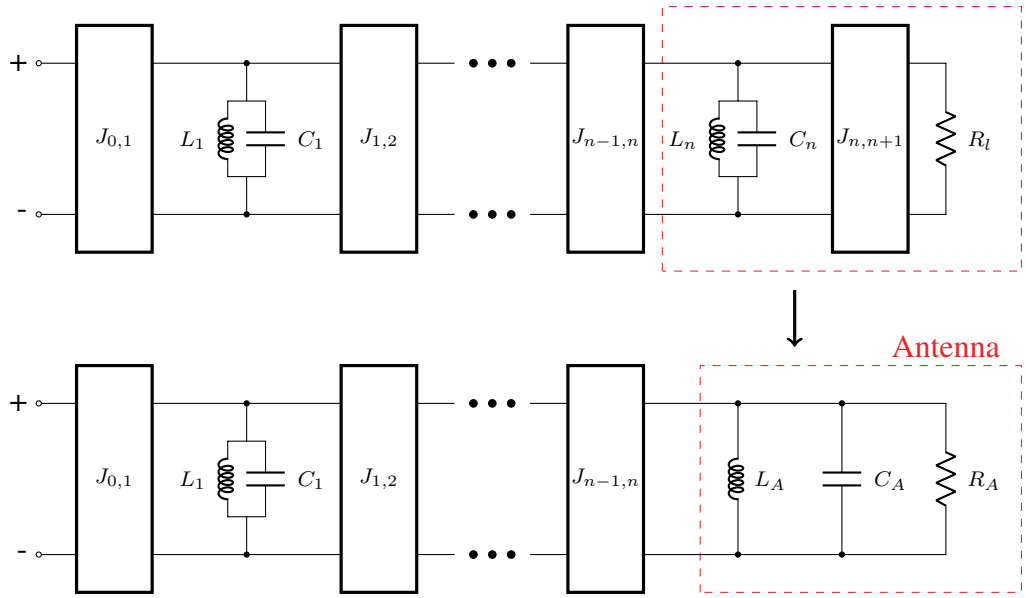

Figure 1.4: Filtenna concept: antenna replaces the final resonator, output inverter, and load [4], [5]

provides one of the poles of the filter response. Designs satisfying this condition are filtennas in the strictest sense, as the filtering and radiating components are truly integrated into a cohesive unit. This will be taken as the definition of the term *filtenna* in this work.

As mentioned before, the integration of filtering and radiating structures in a filtenna can reduce the losses associated with port reflections by eliminating the ports between the filter and antenna and the transmission line that traditionally connects them [7]. Reducing the port mismatch losses helps to improve the noise figure of receiver systems, as the first component in the receiver dominates the overall receiver noise figure [8]. Further, reduced losses are beneficial to phased array systems, where lossy components, particularly phase shifters, already limit the system noise figure and degrade beamforming performance [9].

Filtennas also help reduce the overall design size, as the radiating element is now more closely integrated with the filtering components in a physical sense [10].

Further, eliminating the transmission line that typically connects the antenna and filter reduces the overall space requirement. The reduced size of a filtenna makes it an attractive option for consumer electronics, where designers are always aiming to increase circuit density to provide more functionality to their users.

Filtennas generally have wider impedance bandwidths and higher selectivity than their corresponding isolated antennas due to the fact that the radiating element in a filtenna is electromagnetically coupled to filter resonators [11]. This coupling induces new modes on the antenna element, which is the same mechanism that controls the bandwidth of filters based on coupled resonators [12]. The new modes on the antenna will occur at different resonant frequencies. The separation between the resonant frequencies, and therefore the bandwidth of the filtenna, can be controlled by designing the filtenna to achieve a certain coupling strength between the antenna element and the previous resonator.

While filtennas can help improve SWaP-C, they do not address the issue of spectrum crowding. This can be remedied by incorporating a common spectrum management strategy: frequency tuning and diversity. Tunable and reconfigurable components have become popular for spectrum management [13]. A tunable filtenna offers the flexibility of tunable components as well as the improved performance and reduced size of a filtenna. Tunable filtennas have cognitive radio applications, where reconfigurable and tunable components are already being used to adaptively improve radio system performance [14], [15].

1.1 Previous Work

Numerous filtenna designs have been presented in the literature with varying degrees of fidelity to the filtenna definition of Abbaspour-Tamijani *et al.* [4]. Many designs have been presented that do not satisfy the strict definition of a filtenna, but do provide a degree of integration that eliminates the standard interfaces from the filter and antenna designs. These loosely-integrated filtennas generally involve designing the filter and antenna separately and then connecting them with minimal or no transmission lines, or transmission lines with non-standard characteristic impedances. Because the antenna and filter were designed independently, the antenna does not act as a resonator and, therefore, does not provide an additional pole to the filter response. Tawk *et al.* presented an ultra-wideband Vivaldi antenna with an integrated tunable filter for cognitive radio [16]. The combined filter and antenna are shown in Figure 1.5. The tunable filter was integrated into the transmission line of the antenna and both the filter and antenna used standard 50-Ω ports.

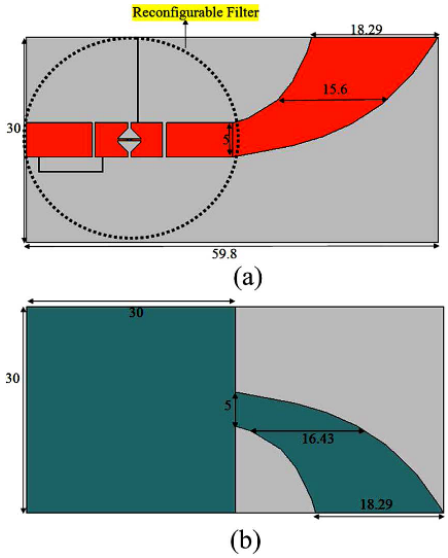

Figure 1.5: Connected filter and antenna geometry from Tawk *et al.* [16]. (a) Top layer with reconfigurable filter and upper half of Vivaldi antenna. (b) Bottom layer (ground).

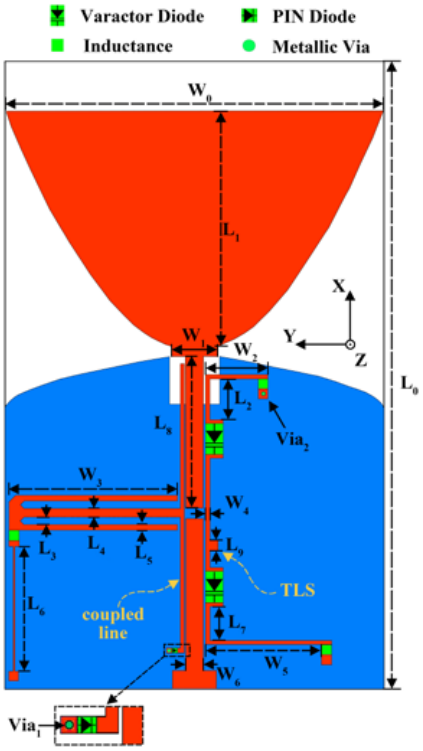

Figure 1.6: Connected filter and monopole antenna from Tang *et al.* [15]. Top layer (red) showing monopole in upper half of figure and filter in the lower half. Bottom (ground) layer in blue.

Another design that loosely integrated a reconfigurable filter with an antenna was presented by Tang *et al.* [15]. The filter is connected directly to the input port of a wideband monopole antenna, but the characteristic impedance of the input and output ports of the filter and monopole are both stated to be 50 Ω. While this does not violate the definition of a filtenna, it is indicative of the fact that the filter and antenna were designed separately. The response of the connected filter and antenna does not appear to be of a higher order than that of the original filter. The geometry of the filter connected to the antenna is shown in Figure 1.6. Other loosely integrated filtering antenna designs can be found in the literature [17]–[19]. These will not be treated further as they do not illustrate important filtenna design concepts. There are also many designs that adhere to the strict definition of a filtenna. Gong *et*

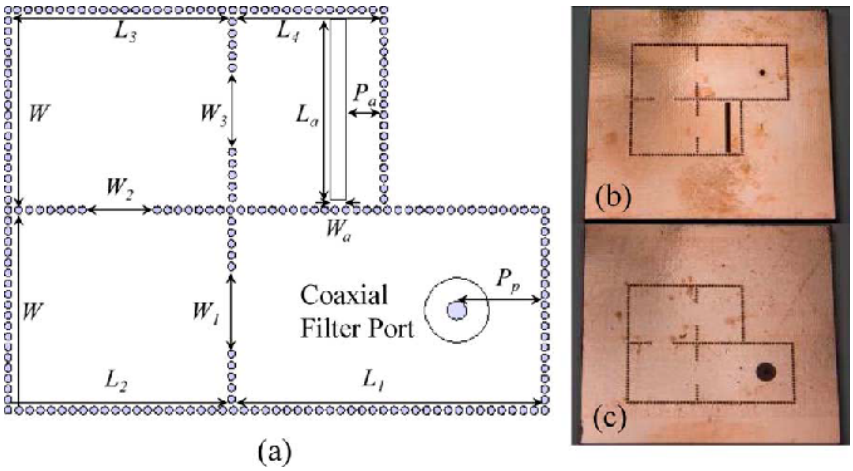

Figure 1.7: Filtenna geometry from Yusuf and Gong in [21] and [22]. (a) Geometry schematic showing SIW cavities and slot antenna. (b) Top view of fabricated design showing slot antenna. (c) Bottom view of fabricated design showing coax port.

al. showed the integration of a slot antenna with an electromagnetic band-gap metamaterial substrate [20] to create a second-order response. The metamaterial acted as the first resonator, while the slot antenna acted as the second resonator. Yusuf and Gong demonstrated a filtenna design procedure to integrate substrate-integrated waveguide (SIW) cavity resonators with a slot antenna [21], [22]. The geometry of the filtennas treated in these works is show in Figure 1.7. The slot antenna acts as the final resonator and load of the filter, making these designs true filtennas. The equivalent circuit model of the cavity resonators coupled to the slot antenna was used to co-design the antenna and filter. The authors detailed how the circuit model parameters were extracted and the slot antenna size and placement were adjusted to provide the reactive frequency response necessary for the antenna to act as a filter resonator [22]. Yusuf and Gong have also shown the integration of a patch antenna with SIW cavity resonators [23]. In this work, the authors discussed how the antenna's bandwidth determines its role in the filter network: an antenna with a bandwidth wider than the filter can act as a load, while an antenna with a bandwidth equal to or smaller than the filter can act as a resonator and load, thereby meeting

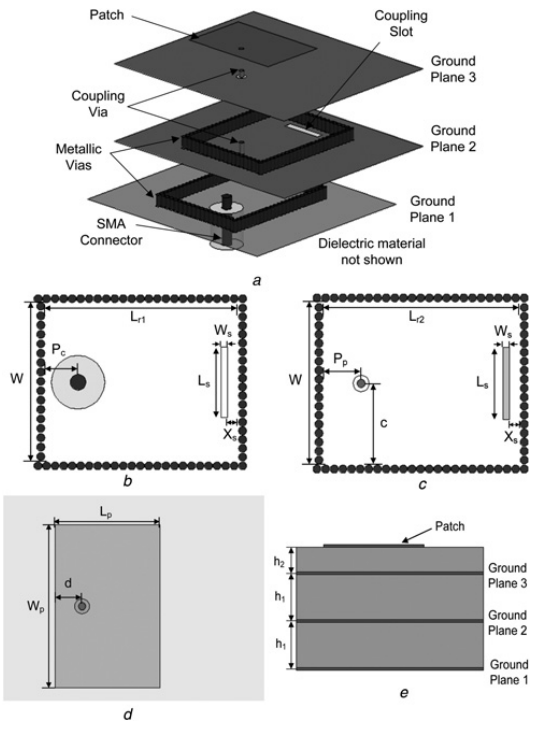

Figure 1.8: Filtenna presented by Yusuf *et al.* in [7]. (a) Exploded view of the metal components of the filtenna design. (b) Geometry of the first cavity resonator with coax port and slot coupling to second resonator. (c) The geometry of the second cavity resonator with coupling slot from first resonator and probe coupling to patch. (d) Geometry of patch antenna on top layer. (e) Full design stack-up.

the definition of a filtenna [23]. In another work with vertically-stacked SIW cavity resonators integrated with a patch antenna, Yusuf *et al.* discussed the relationship between the external quality factor, Q_{ext}, of the filter and the radiation quality factor, Q_{rad}, of the antenna [7]. The geometry of the filtenna is shown in Figure 1.8. The Q factor is the ratio of stored energy to lost energy, which makes it an important figure of merit for resonators. The required radiation Q factor for the antenna was derived from the lumped-element model of the filter with the desired response. The radiation Q factor of an antenna is the ratio of the energy stored in the reactive near-fields of the antenna to the energy radiated by the antenna [24]. The output external Q factor ($Q_{ext,out}$) derived from the filter, which determines the amount of

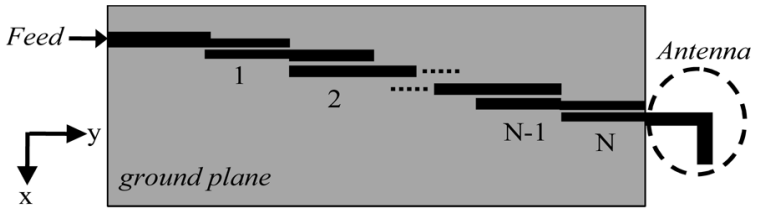

Figure 1.9: Geometry of the filtenna by Chuang and Chung in [29]. The inverted-L antenna acts as a series resonator coupled to the $N-1$ half-wave resonators.

output coupling for the filter, was used to determine the dimensions of the patch antenna. Li *et al.* showed that a filtenna can be used as an element in a phased array to achieve higher bandwidth and improved active reflection coefficient performance [25]. The integration of an SIW cavity resonator with a patch antenna improves the bandwidth of the antenna element without the need to increase the thickness of the substrate. Larger substrate thicknesses allow surface waves to propagate on the array aperture, which increases mutual coupling and degrades the array's scan performance [26]. Using filtennas as array elements improved the bandwidth without increasing the substrate thickness, thereby preventing increased mutual coupling. Dr. Gong's group at the University of Central Florida has demonstrated similar filtenna co-design techniques in several other publications [11], [27], [28].

Chuang and Chung have demonstrated a successful microstrip filtenna consisting of coupled parallel half-wavelength resonators and an inverted-L antenna [29]. The geometry of the filtenna is shown in Figure 1.9. The circuit parameters of the antenna were extracted using a full-wave simulator and the dependence of the circuit model on the geometry of the antenna was characterized. The quality factor of the antenna was characterized in terms of the circuit model and then the antenna geometry. The antenna was then designed to achieve $Q_{rad} = Q_{ext,out}$. The resulting design achieved the filter response of the specified order with the antenna acting as the last resonator. The design also demonstrated improved performance over the

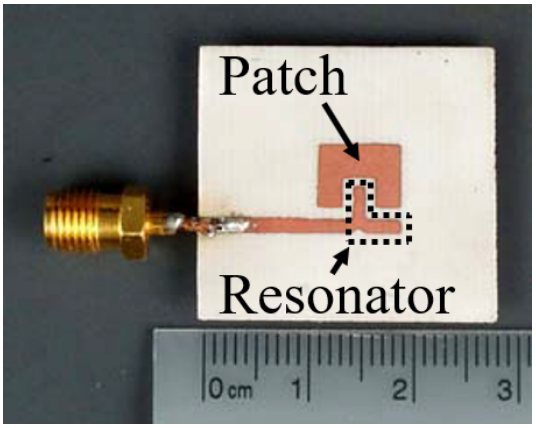

Figure 1.10: The realized patch with intruded half-wave resonator filtenna from Lin and Chung in [10]. Annotations added.

corresponding antenna in cascade with a filter of one order less [29]. Chuang and Chung also presented a microstrip filtenna synthesized from a Γ-shaped microstrip antenna and a coupled-line microstrip resonator [30]. Unlike the filtenna in [29], the resonator and antenna in this design were directly connected, so the filtenna was created using a filter network without inverters. A second-order filter response was achieved as intended. Lin and Chung demonstrated a filtenna with a second-order response designed with a microstrip patch coupled to a half-wavelength resonator [10]. The geometry of the fabricated filtenna is shown in Figure 1.10. The half-wavelength resonator was bent such that it could be tapped near the bend and one end of the bend could be edge-coupled to the patch antenna through an inset in the patch. The filtenna achieved the desired second-order filtering response in a small circuit area (approximately $0.6\lambda_g \times 0.6\lambda_g$).

Kufa *et al.* synthesized an aperture-fed patch antenna array using filter theory to determine the dimensions of the antenna elements, which acted as the filter resonators, and the geometry of the array feed line [31]. The geometry of the array is shown in Figure 1.11. The authors derived a new set of lowpass filter prototype coefficients (g coefficients) based on antenna array theory. The g coefficients were

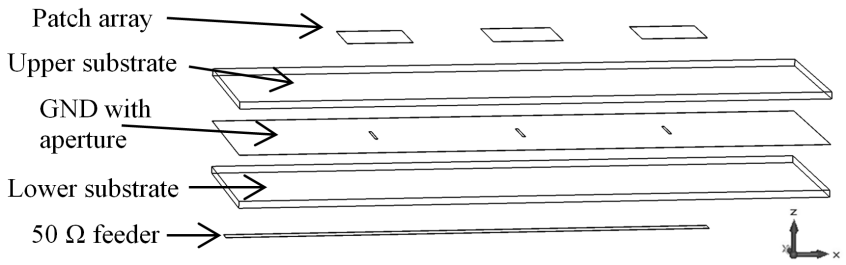

Figure 1.11: The geometry of the filtenna by Kufa *et al.* in [31]. The dimensions of the patches control their resonator properties, while the dimensions of the apertures in the ground plane control the coupling between the patches.

then used to design parallel RLC resonators and admittance inverters (J inverters) to achieve the desired filter response. These J inverter values were related to the design of the feeding apertures, while the RLC values were related to the patch antenna dimensions. The resulting array achieved the desired frequency and radiation responses.

There are other filtenna design approaches presented in the literature, but these are not covered here due to the increased complexity of their methods [32]–[34].

1.1.1 Previous Tunable Filtenna Designs

Lovato *et al.* presented a patch antenna/hairpin resonator second-order filtenna that was electrically tuned using varactor diodes [35]. Both the hairpin resonator and the patch antenna were end-loaded with varactors to make both components frequency-tunable, enabling the filtenna to tune its center frequency. The geometry of the tunable filtenna is shown in Figure 1.12. The simulated results showed that the filtenna achieved the desired second-order response and was able to tune its center frequency; however, the authors did not fabricate the design. This means that no considerations were made for applying direct current (DC) voltages to bias the varactors, which controls the amount of capacitance supplied by each varactor and, therefore, the center frequency of the filtenna. No further tunable filtenna designs

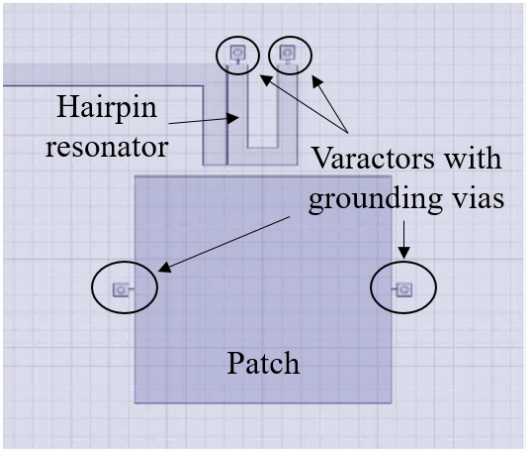

Figure 1.12: Geometry of tunable microstrip hairpin/patch filtenna by Lovato *et al.* from [35]. Annotations added to clarify geometry.

were found which satisfy the definition of a filtenna from [4].

1.2 Objectives

The design investigated in this work is a microstrip filtenna consisting of combline resonators and a capacitively-loaded patch antenna element. To date, there do not appear to be any references in the literature to a filtenna synthesized from tunable microstrip combline resonators and a tunable microstrip patch antenna; thus, this is a novel implementation of a filtenna. Further, there are few published tunable filtennas that meet the definition of a filtenna set forth in [4]. The filtenna demonstrated in this work is able to tune its center frequency.

Based on the review of previous work in this field, the key concepts seen in successful filtenna designs are:

- The antenna bandwidth must be less than or equal to the filter bandwidth to act as a resonator [23]
- $Q_{rad} = Q_{ext,out}$ [7], [29]

- The equivalent circuit model of the antenna relates the antenna geometry to the antenna radiation Q factor [7], [29]

- The output external quality factor from the filter design determines the antenna geometry [7], [29]

These principles provide the general guide for this work. The desired filter response provides the design parameters for the antenna; namely, the radiation quality factor and the coupling of the antenna to the previous resonator. The circuit model for the microstrip patch determines the physical dimensions of the antenna that achieve the specified frequency response.

This thesis demonstrates a novel, single-layer microstrip filtenna design with center frequency tuning for interference mitigation applications by following the co-design methods documented in the literature. The filtenna is realized using microstrip combline resonators and a microstrip patch antenna and is able to continuously tune its center frequency in the S-band using varactor loading. The antenna is designed to be as structurally similar to the resonators as possible. The S-band is targeted because the resulting designs are not so small as to be difficult to fabricate, but also not so large as to be cumbersome. Varactors and other components that operate in the S-band are also readily available. A combline filter and reference microstrip patch are designed and the filtenna is compared against these baseline designs.

Chapter 2

Theory from Filters and Antennas

2.1 Filters

Filters are RF devices which pass signals in a specific frequency range and reject signals outside that range. This allows systems to isolate signals in the frequency bands where they operate and avoid interference from nearby bands, which enables channelized communication in consumer products, allows for suppression of mixer intermodulation products in radar and communication systems [3], and helps protect against wideband jamming in military applications.

When designing a filter, it is typical to start with a lowpass filter prototype consisting of a ladder network of inductors and capacitors [5]. The values of the inductors and capacitors are determined by the lowpass filter prototype coefficients, also known as g coefficients, for the desired filter response, such as Butterworth or Chebyshev. These coefficients can be calculated for a specific response based on the properties of the underlying polynomial function [5]. Examples of such ladder networks are shown in Figure 2.1. Generally, the coefficient of the source resistance, g_0, is 1. The coefficient of the load resistance, g_{n+1}, may not be 1, depending on the filter response type and the order of the filter. The number of inductors and capacitors is determined by the order of the filter, where each additional component

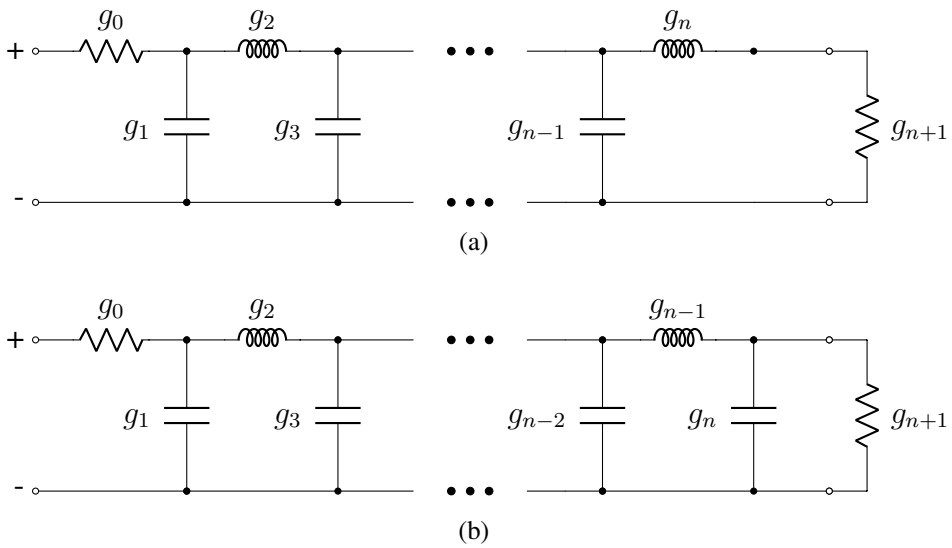

Figure 2.1: Example of ladder network filters using lumped elements. (a) An even-order filter with equal numbers of inductors and capacitors. (b) An odd-order filter with one more capacitor than inductors.

adds an order to the filter response. In the examples of Figure 2.1, the filters are of order n, meaning they have n poles. Once the lowpass filter prototype has been designed, frequency response transforms, such as lowpass-to-highpass or lowpass-to-bandpass, are applied. These transforms will convert the inductors and capacitors to the appropriate element or elements, depending on the transform. For example, if a lowpass-to-bandpass transform were applied to either filter in Figure 2.1, each inductor would be transformed into a series combination of an inductor and capacitor, and each capacitor in the original network would be transformed into a parallel combination of an inductor and capacitor. The values of these new components are determined by the characteristics of the new response: the cutoff frequency for lowpass and highpass filters, and the center frequency and bandwidth for bandpass and bandstop filters. Once the frequency transform has been applied, the element values can be scaled to the impedance of the new system, which is typically a standard transmission line impedance such as 50 Ω or 75 Ω.

Frequency transformations and impedance scaling can sometimes result in el-

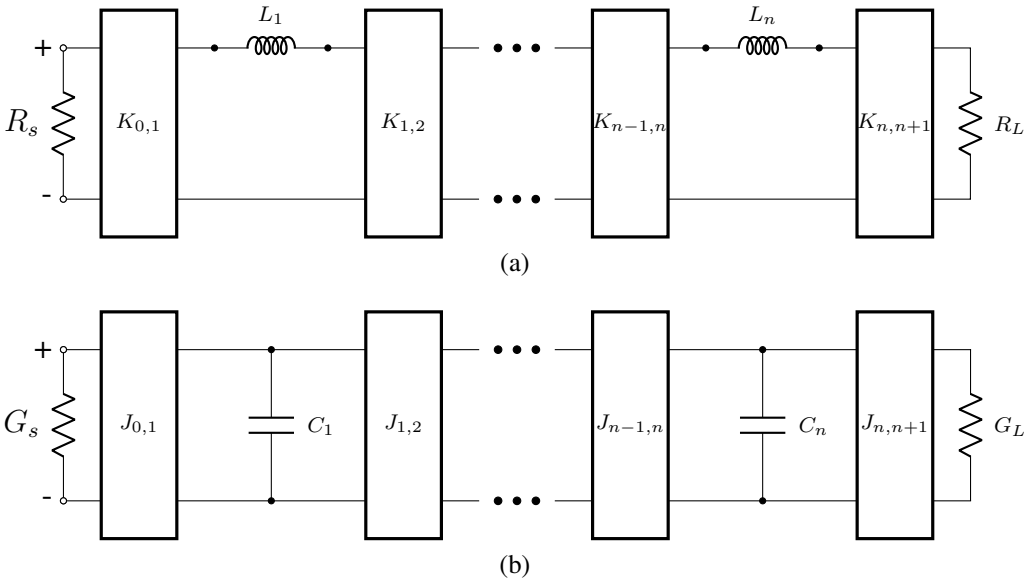

Figure 2.2: Possible inverter-based implementations of a filter [12]. (a) Series inductors with impedance inverters. (b) Shunt capacitors with admittance inverters.

ement values which are too small or too large to be physically realizable. In such cases, the filter can realized by converting the ladder network to a network of inverters and either inductors or capacitors only. Thus, the network from Figure 2.1 could converted to either of the networks in Figure 2.2. The values of the K inverters in Figure 2.2a can be calculated using [12]:

$$K_{01} = \sqrt{\frac{R_s L_1}{g_0 g_1}} \tag{2.1}$$

$$K_{i,i+1} = \sqrt{\frac{L_i L_{i+1}}{g_i g_{i+1}}} \quad \text{for } i = 1, 2, \ldots, n-1 \tag{2.2}$$

$$K_{n,n+1} = \sqrt{\frac{L_n R_L}{g_n g_{n+1}}} \tag{2.3}$$

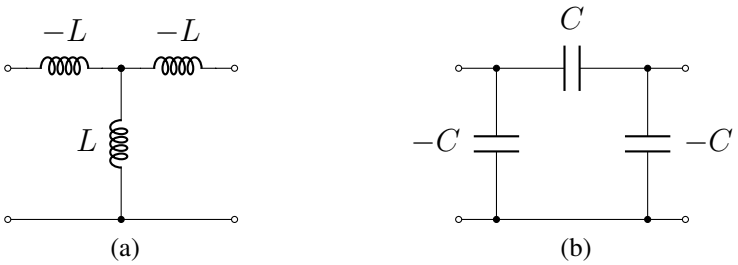

Figure 2.3: Inverter realizations. (a) K inverter. (b) J inverter.

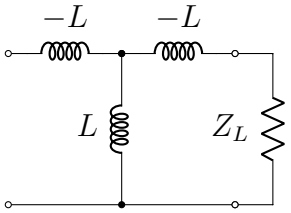

Figure 2.4: Loaded K inverter

Similarly, the values of the J inverters in Figure 2.2b can be calculated as [12]:

$$J_{01} = \sqrt{\frac{G_s C_1}{g_0 g_1}} \tag{2.4}$$

$$J_{i,i+1} = \sqrt{\frac{C_i C_{i+1}}{g_i g_{i+1}}} \quad \text{for } i = 1, 2, \ldots, n-1 \tag{2.5}$$

$$J_{n,n+1} = \sqrt{\frac{C_n G_L}{g_n g_{n+1}}} \tag{2.6}$$

The values of L_i and C_i can be chosen as any convenient values, thereby removing the issue of unrealizable filter elements. Inverters can be realized using T- and pi-networks of inductors or capacitors, as shown in Figure 2.3. The inverting property of the K inverter in Figure 2.3a can be verified if a load impedance is connected to the inverter, as in Figure 2.4, and the input impedance is calculated. The input

impedance to the circuit in Figure 2.4 is

$$Z_{in} = -j\omega L + \frac{j\omega L(Z_L - j\omega L)}{j\omega L + Z_L - j\omega L} = -j\omega L + \frac{j\omega L Z_L + \omega^2 L^2}{Z_L}$$

$$= -j\omega L + j\omega L + \frac{(\omega L)^2}{Z_L} = \frac{(\omega L)^2}{Z_L} = \frac{K^2}{Z_L} \tag{2.7}$$

This shows that the circuit in Figure 2.3a acts as an impedance inverter with $K = \omega L$ [5]. The inverting property of the circuit in Figure 2.3b can be similarly demonstrated, and it can be shown that $J = \omega C$ [5]. Both inverters can also be realized by replacing each component by its dual, forming a T-network of capacitors for the K inverter with $K = 1/\omega C$ and a pi-network of inductors for the J inverter with $J = 1/\omega L$. In a ladder network, the negative inductors and capacitors can be absorbed by combining them with series inductors and shunt capacitors, respectively, that already existed in the network.

2.1.1 Coupled Resonator Filters

A common filter implementation is that of coupled resonators, which can be implemented in a variety of technologies and offer flexibility in achieving the desired filter response [36]. The coupling between resonators can occur through the electric fields or the magnetic fields, or both, around the resonators, and can be represented by an inverter of either type. Coupled resonators act as filters by allowing only specific frequencies to pass. As each resonator is excited by incoming energy, it couples to nearby resonators, thereby propagating energy through the filter. Because the energy transfer occurs through the resonators, only those frequencies that excite resonance will pass through the filter. Thus, the coupled resonator architecture is suitable for the design and realization of filters.

The coupling between resonators causes even- and odd-mode resonances to oc-

cur in each resonator [12]. These modes occur at different frequencies, thereby allowing a certain band of frequencies to excite the resonators and pass through the filter. The separation between the even- and odd-mode resonant frequencies is controlled by the strength of the coupling between two resonators: the stronger the coupling between two resonators, the wider the separation between the resonant frequencies. The coupling between two resonators can usually be controlled by one or more physical parameters, such as the distance between coupled transmission lines or the size of a coupling iris between two cavity resonators. Thus, bandpass filters with specified bandwidths can be designed by adjusting the coupling between resonators to achieve the required bandwidth.

The external quality factor, Q_{ext}, of the input and output resonators of a filter control how much energy is coupled into and out of the filter. The external quality factor controls the flatness of the insertion loss response, because the strength of the input and output coupling controls the impedance match at the ports of the filter.

Coupled resonator filters can be designed analytically, but this approach is generally complex and time-intensive. For resonators made with practical RF technologies, such as microstrip line and cavity resonators, precise mathematical models describing the coupling between resonators can be difficult to derive and use. For this reason, simpler and faster methods of designing coupled resonator filters have been developed. Dishal describes a method of converting the lowpass prototype filter coefficients (g coefficients) into internal coupling coefficients, k_{ij}, which dictate the strength of the coupling between given resonators [37]:

$$k_{i,j} = \frac{\Delta}{\sqrt{g_i g_j}} \tag{2.8}$$

where Δ is the fractional bandwidth of the filter, and g_i is the i^{th} lowpass filter

coefficient. The fractional bandwidth of a filter is defined as

$$\Delta = \frac{\omega_{c2} - \omega_{c1}}{\omega_0} = \frac{f_{c2} - f_{c1}}{f_0} \tag{2.9}$$

where f_{c1} is lower cutoff frequency and f_{c2} is the higher cutoff frequency of the filter.

Swanson showed how Dishal's method can be used to rapidly design a filter using numerical electromagnetics software to characterize the coupling between resonators [38]. The internal coupling is extracted by simulating the even- and odd-mode resonant frequencies of two resonators that are weakly externally-coupled. The coupling coefficient is then calculated as

$$k = \frac{f_2^2 - f_1^2}{f_2^2 + f_1^2} \tag{2.10}$$

where f_1 is the lower resonant frequency and f_2 is the higher resonant frequency [38]. The required external Q factors of the filter are given by [38]:

$$Q_{ext,in} = \frac{g_0 g_1}{\Delta} \tag{2.11}$$

$$Q_{ext,out} = \frac{g_N g_{N+1}}{\Delta} \tag{2.12}$$

The external quality factors can be extracted with the doubly-loaded resonator method described by Hong [12]. In this method, the coupling of a single resonator to two ports is simulated, and the external quality factor is extracted from the insertion loss curve as

$$Q_{ext} = \frac{2f_p}{f_u - f_\ell} \tag{2.13}$$

where f_p is the frequency corresponding to the peak of S_{21}, and f_ℓ and f_u are the lower and upper frequencies, respectively, where S_{21} is reduced by 3 dB from its

peak. The factor of 2 is due to the fact that the resonator is loaded with two ports [12]. Once the internal and external coupling have been extracted using an electromagnetics simulator, the appropriate geometry for the filter can be determined.

2.1.2 Tunable Filters

Many tunable filter designs can be found in the literature [39]–[43]. A range of tuning mechanisms is available, but one of the simplest to fabricate for planar designs is tunable capacitive loading [40]. For microstrip filters, capacitively loading resonators with varactor diodes is a popular tuning method. The tunable capacitance of the varactor is used to tune the resonant frequency of the microstrip resonators, thereby tuning the center frequency of the filter. The tunable capacitance combines with the inherent capacitance of the resonator to change the resonant frequency, which is given by

$$\omega_0 = \frac{1}{\sqrt{LC}} \tag{2.14}$$

where L and C are the inductance and capacitance of the resonator, respectively. By adding a tunable capacitance, typically in parallel with the inherent capacitance, this becomes

$$\omega = \frac{1}{\sqrt{L(C + C_L)}} \tag{2.15}$$

where C_L is the tunable loading capacitance. By varying C_L, the center frequency of the resonator can be changed.

2.2 Antennas

2.2.1 Antennas as Resonators

Antennas are structures that act as matching networks between guided waves on transmission lines to waves propagating in free space. The antennas of concern in this work are known as *resonant* antennas, as their voltage and current distributions can be represented by standing-wave patterns [44]. Because these antennas are resonant structures, they can be represented by the equivalent circuit of a resonator: a parallel or series RLC circuit. As mentioned in Chapter 1, this is the basis of the filtenna concept. By coupling an antenna to a filter resonator, the antenna can provide one of the poles of the filter response. This will also improve the bandwidth of the antenna, as the coupling between the antenna and the resonators will cause the poles of the frequency response to separate, as with a coupled resonator filter.

The equivalent resonant circuit model parameters of an antenna can be obtained from simulations using reactance or susceptance slope parameters [36]. These parameters can be used to describe how similarly two resonators behave near their resonant frequencies. When dealing with series RLC resonators, the reactance slope parameter is used, whereas the susceptance slope parameter is used for parallel resonators. The susceptance slope parameter is defined as

$$b = \frac{\omega_0}{2} \left. \frac{dB(\omega)}{d\omega} \right|_{\omega=\omega_0} \tag{2.16}$$

where $B(\omega)$ is the susceptance of the antenna as a function of angular frequency and ω_0 is the resonant angular frequency. The reactance slope parameter is defined similarly using the derivative of the reactance instead of the susceptance. For a

parallel resonator, the susceptance slope parameter is equal to $\omega_0 C$ [12]:

$$b = \frac{\omega_0}{2} \left. \frac{d(\omega C - 1/(\omega L))}{d\omega} \right|_{\omega=\omega_0} = \frac{\omega_0}{2} \left. \left(C + \frac{1}{\omega^2 L} \right) \right|_{\omega=\omega_0} = \frac{\omega_0}{2} \left(C + \frac{1}{\omega_0^2 L} \right)$$

$$= \frac{\omega_0}{2} \left(C + \frac{LC}{L} \right) = \frac{\omega_0}{2}(2C) = \omega_0 C \tag{2.17}$$

The reactance slope parameter of a series resonator can similarly be shown to be $x = \omega_0 L$ [12]. The inductance of the parallel model can be found from (2.14) after the resonant frequency is found and the capacitance is extracted using (2.17). Thus, by calculating the appropriate slope parameter for an antenna, based on the type of resonance displayed by the input impedance, the inductive and capacitive components of the antenna's equivalent circuit model can be obtained. The resistive component is the real part of the input impedance at resonance, which is the combined radiation and loss resistances of the antenna [45].

The radiation quality factor of the antenna, Q_{rad}, plays the part of the output external quality factor of the filter, $Q_{ext,out}$, in filtennas [7]. Thus, the antenna element in a filtenna is designed to achieve a specific radiation quality factor. The radiation quality factor can be obtained from simulations by extracting the equivalent circuit of a lossless model of the antenna. If the dielectric and conductive losses of the simulated antenna model are set to zero by setting the loss tangent of the dielectric materials to 0 and making all metals perfect electrical conductors, then the resistance in the extracted circuit model will be the radiation resistance of the antenna [7]. Q_{rad} can be calculated using the typical formulas for the Q factor: $Q_{rad} = \omega_0 RC$ for parallel resonators and $Q_{rad} = \omega_0 L/R$ for series resonators [5]. By extracting the radiation Q-factor as a function of some antenna geometry parameter, the antenna can be designed for integration into a filtenna.

2.2.2 Antenna Polarization

Polarization is an antenna property that describes the orientation of the electric field vector radiated by the antenna. The polarization may be referenced to the surface of the earth, in which case the polarizations are typically called *horizontal*, if the electric field vector is parallel to the surface of the earth, and *vertical*, where the electric field vector is perpendicular to the surface of the earth.

An antenna's polarization can also be referenced to another antenna. When the electric field vectors of two antennas are co-linear, the antennas are said to be *co-polarized*. If the vectors are perpendicular to each other, the antennas are said to be *cross-polarized*. This concept is illustrated in Figure 2.5.

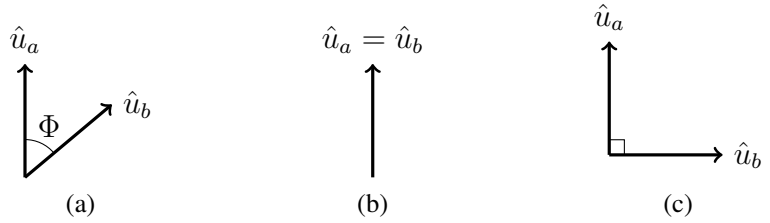

Figure 2.5: Illustration of antenna polarization. Vectors $\hat{u}_a$ and $\hat{u}_b$ are unit vectors. (a) The general case with some angle, Φ, between the antenna polarization vectors. (b) The co-polarized case where $\Phi = 0^o$. (c) The cross-polarized case where $\Phi = 90^o$.

The relative polarization of two antennas impacts the amount of energy that can be transferred between them. Because antennas are reciprocal devices, meaning that they transmit and receive power the same way in a given direction, the polarization of an antenna not only indicates the orientation of the electric field that the antenna radiates, but also the orientation of incident electric fields that can excite currents on the antenna and transfer power to the antenna's terminals. If a wave is incident on an antenna such that the waves' electric field forms some angle Φ with the polarization vector of the antenna, the field that excites the antenna is the projection of the wave

polarization unit vector onto the antenna's polarization unit vector [44]. Because the power transmitted to the antenna is proportional the the magnitude of the field squared [44], the power transfered to the antenna is

$$P_r = P_i |\cos \Phi|^2 \tag{2.18}$$

where P_r is the power received by the antenna and P_i is the power carried by the incident wave. Theoretically, if two antennas are cross-polarized, the power transmitted between them is 0, because $\Phi = 90^o$, making the projection of the polarization vectors 0. This is not the case in practice due to non-idealities. Real antennas have volumes and incident electric fields that are not polarized in alignment with the polarization of the antenna can excite currents on the antenna volume. Some of these current will result in power transfer to the antenna. Further, in real antennas, the shape of the antenna does not perfectly match the ideal shape that theoretically produces a single polarization, thus the fields around the antenna are perturbed by the imperfections of the antenna and other polarizations appear. The imperfections in the antenna's shape are generally due to fabrication tolerances and error. The description of polarization given here is a simplified two-dimensional case; for a real system, the polarization vectors of the antennas will have components in three dimensions.

Given that the fields of an antenna are measured using a second antenna, and the terms *co-polarization* and *cross-polarization* are dependent on the relative polarizations of the antennas, it is necessary to define standards for measuring the co- and cross-polarized fields of an antenna. Ludwig defines several important standards used in antenna measurements [46]. The standard used in this work to define co- and cross-polarization is known as *Ludwig III*, as it most closely matches the antenna patterns measured in an anechoic chamber [46], and coincides with the

antenna geometry in this work.

2.2.3 Antenna Gain

One important antenna parameter is the antenna's gain. The gain is the product of the antenna's efficiency with its directivity [44]:

$$G(\theta, \phi) = e_{cd} D(\theta, \phi) \tag{2.19}$$

The term e_{cd} is the combined efficiency due to conductive and dielectric losses on the antenna structure [44]. The directivity is "equal to the ratio of [the antenna's] radiation intensity in a given direction over that of an isotropic source" [44]. An isotropic source is a non-realizable source which radiates energy equally in all directions. The directivity is, therefore, a measure of how well an antenna directs energy in a specific direction. Thus, the gain describes not only how well an antenna directs energy, but also how efficiently it radiates. A related concept is *realized gain*, which also accounts for the impedance mismatch seen at the antenna terminals. The realized gain is given by [44]:

$$G_r(\theta, \phi) = (1 - |\Gamma|^2) G(\theta, \phi) \tag{2.20}$$

where Γ is the voltage reflection coefficient at the antenna terminals. The reflection coefficient is the ratio of the amplitude of the voltage wave reflected from the terminals of the antenna to the amplitude of the voltage wave incident on the terminals of the antenna [6]. As the reflected voltage can never be greater than the incident voltage for a passive device, such as the antenna and filtenna in this work, Γ is in the range of 0 to 1, inclusive [5]. This means that the realized gain is always less than or equal to the gain.

Note that in this work, unless otherwise specified, the term gain is used to denote realized gain. The realized gain is used because this is the quantity measured in the anechoic chamber when the radiation performances of the patch and filtenna are characterized.

There are numerous methods to measure the gain of an antenna, but the one used in this work is known as the *gain transfer method* [44]. This method calculates the gain of an antenna using a known reference antenna and applications of the Friis Transmission Equation. The Friis Transmission Equation describes the power received by an antenna as a function of the power transmitted by the source (which is usually also an antenna), the antenna gains, and signal path geometry. The Friis equation is given by [44]:

$$P_r = P_t \left(\frac{\lambda_0}{4\pi R} \right)^2 G_t G_r \tag{2.21}$$

where P_r is the power received at the receiving antenna, P_t is the power transmitted by the transmitting antenna, λ_0 is the free-space wavelength of the signal, R is the transmission path distance between the antennas, and G_t and G_r are the gains of the transmitting and receiving antennas, respectively. The form in (2.21) assumes that the antennas are co-polarized, aligned in the direction of each antenna's maximum gain, and well-matched to their feed lines. In the gain transfer method, the antenna under test (AUT) is measured in an anechoic chamber as usual. The far-field anechoic chamber uses a network analyzer to measure the power transmitted between two antennas, the AUT and a measurement probe antenna. The term *far-field* refers to the region where rays originating from the extents of the largest antenna dimension, D, appear approximately parallel to an observer [6]. The far-field begins at a distance, R, between the antenna and observer such that $R \geq 2D^2/\lambda_0$ [6]. The goal in a far-field anechoic chamber test is to measure the far-fields radiated or re-

ceived by an antenna as a function of angle relative to the AUT. Thus, an ideal measurement only captures the fields transmitted between the AUT and probe on the direct, or *line-of-sight*, path between the antennas. The anechoic chamber is a room with metallic walls that isolate the antennas inside from signals outside the chamber; however, because the walls are metal, they reflect the signal transmitted in the measurement. This causes the receiving antenna to receive both the signal from the direct path and the signals from the reflected paths, an issue known as *multipath*. To remedy this, the walls of the anechoic chamber are lined with a material that absorbs RF signals. The absorbing material dissipates the multipath signals so that the network analyzer measures, to the greatest extent possible, only the power that is transmitted between the antennas on the direct path. Once the AUT has been measured, a standard gain antenna, an antenna with a known gain, is measured in the chamber. Then the Friis equation can be applied to the two measurements to find the gain of the AUT. Both measurements can be described by the Friis equation as:

$$P_{AUT} = P_t \left(\frac{\lambda_0}{4\pi R} \right)^2 G_t G_{AUT} \tag{2.22}$$

$$P_S = P_t \left(\frac{\lambda_0}{4\pi R} \right)^2 G_t G_S \tag{2.23}$$

where the *AUT* subscripts represent the measurement of the AUT, and the *S* subscript represents the measurement of the standard gain antenna. The gain transfer method assumes that measurement frequency, distance between the probe antenna and the measured antenna, the transmit power, and the probe antenna itself do not change between the two measurements [44]. Here, the probe antenna is assumed to be the transmitting antenna in the Friis equation. Both equations can be re-arranged to give

$$\frac{P_{AUT}}{G_{AUT}} = P_t \left(\frac{\lambda}{4\pi R} \right)^2 G_t = \frac{P_S}{G_S} \tag{2.24}$$

which can be re-arranged as

$$G_{AUT} = G_S \frac{P_{AUT}}{P_S} \tag{2.25}$$

The power levels P_{AUT} and P_S are the measurements obtained from the AUT and standard gain antenna. Thus, the gain of the AUT can be calculated with the two measurements and the known gain of the standard gain antenna. As anechoic chamber measurements are usually taken in decibels, it is convenient to work with (2.25) on a logarithmic scale:

$$G_{AUT,dB} = G_{S,dB} + 10\log\left(\frac{P_{AUT}}{P_S}\right) = G_{S,dB} + P_{AUT,dB} - P_{S,dB} \tag{2.26}$$

This is the method used to calculate antenna gains in this work.

2.2.4 Tunable Antennas

Tunable antennas have the ability to change their resonant frequency. This can be achieved in a microstrip antenna with the same mechanism often used for microstrip resonators: variable capacitive loading using varactor diodes [13]. As with the microstrip resonator, the loading capacitance changes the total capacitance of the antenna, causing a shift in the antenna's resonant frequency. Generally, the change in resonant frequency alters the current distributions on the antenna, meaning that the input impedance of the antenna changes. This usually results in an increase in the reflection coefficient [47]–[51]. Changing the current distributions on the antenna will also alter the far-field patterns of the antenna, as the far-field patterns are related to the current distribution by a spatial Fourier transform [44].

2.3 Co-Designed Filter-Antenna Structures

As discussed in Chapter 1, a filtenna is a filter network where the last resonator, output inverter, and load have been replaced with an antenna element. The antenna element must act as a resonator in the filter circuit to provide one of the poles of the filter response [4]. The antenna element is designed to provide a radiation quality factor that matches the output external quality factor of the filter on which the design is based [7]. The coupling between the adjacent resonator and the antenna must also match the coupling designed for that resonator and the resonator that the antenna replaces [7]. The filtenna can provide a number of advantages, including the elimination of the ports and transmission lines between the filter and antenna [4], reduced physical size by integrating two components into one [10], and improved bandwidth and frequency selectivity over stand-alone antenna elements [11].

In measuring the filtenna and comparing it to a filter, the gain of the filtenna as a function of frequency is typically used as an analog for the insertion loss of the filter. This is due to the fact that the gain accounts for the losses in the filtenna.

2.3.1 Tunable Filtennas

The mechanisms that are applied to filters and antennas to achieve frequency tuning can, theoretically, also be applied to filtennas. Because the antenna element is coupled to the filter's resonators, it should be possible to leverage the strategy used in tunable filters of controlling the coupling between the resonators and antenna to achieve the desired return loss over a wider bandwidth than that of the antenna alone. This is one of the goals of this work: to study how the incorporation of tuning mechanisms into a filtenna affect the filtenna's performance and what level of tuning can be achieved.

Chapter 3

Design Procedure

3.1 Combline Filter Design

The combline filter is a filter topology consisting of coupled lengths of transmission line loaded with capacitors at one end, as shown in Figure 3.1. The capacitive

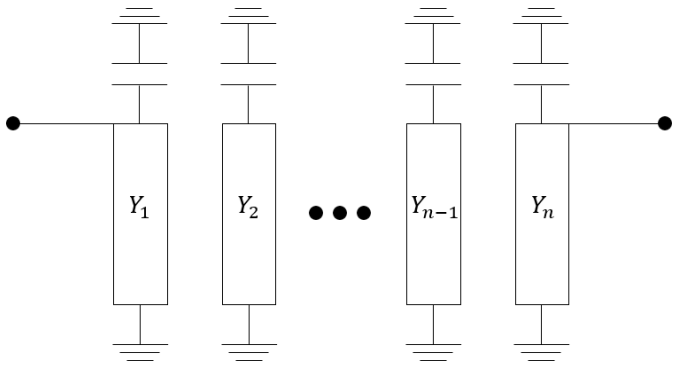

Figure 3.1: Combline filter illustration [40]. Each transmission line has a characteristic admittance of Y_i.

loading allows the lines to be shortened to less than $\lambda_g/8$ [40], thereby reducing the size of the filter. The basic combline can be made tunable by using tunable loading capacitances, such as varactor diodes, in the place of fixed capacitive loads [40]. Intuitively, it seems feasible to convert a tunable microstrip combline filter into a tunable filtenna by removing the output port and replacing the last resonator with a tunable microstrip antenna. This idea is the basis for the filtenna developed here.

3.1.1 Combline Filter Implementation

Before the filtenna was synthesized, a tunable combline filter was designed for comparison. The filter was designed to have a second-order bandpass Chebyshev response with a 15 dB passband return loss ripple, which corresponds to a 0.1396 dB insertion loss ripple. The fractional bandwidth of the filter was chosen to be 6%. The resulting lowpass prototype filter coefficients, corresponding to those illustrated in Figure 2.1, are given in Table 3.1.

Table 3.1: Chebyshev Lowpass Filter Prototype Coefficients

Coefficient	Value
g_0	1
g_1	0.9301
g_2	0.6493
g_3	1.4326

The ideal Chebyshev response, shown in Figure 3.2, was calculated in MATLAB for reference. The internal and external coupling values given by (2.8)-(2.12) are shown in Table 3.2.

Table 3.2: Filter Coupling Parameters

Design Parameter	Value
$Q_{ext,in}$	15.5
k_{12}	0.0772
$Q_{ext,out}$	15.5

Having defined the filter specification and derived the required coupling values, the next step was to design the microwave resonators for the filter.

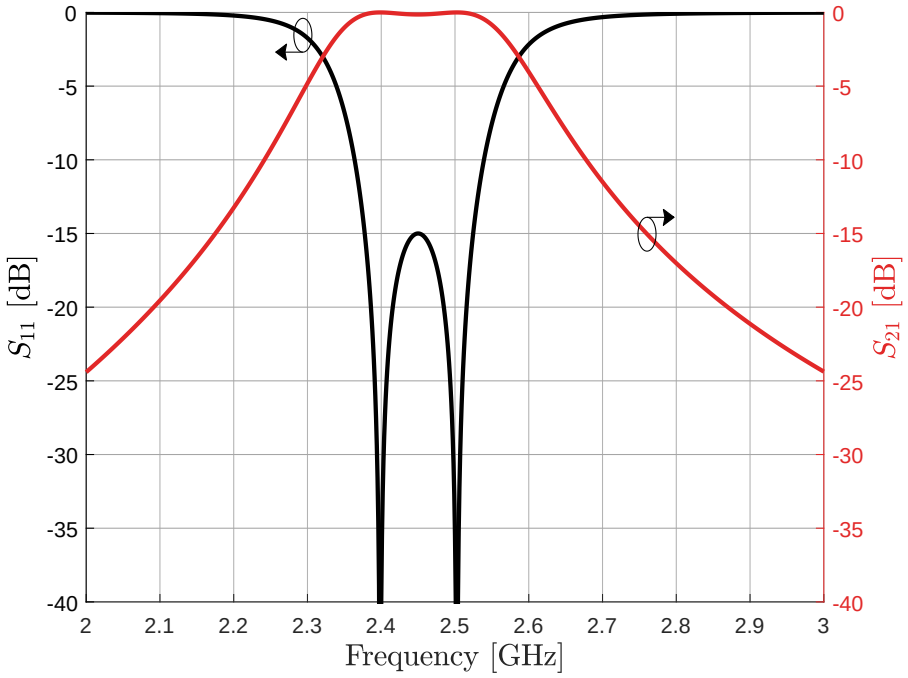

Figure 3.2: Ideal Chebyshev response calculated in MATLAB for reference

Resonators

The combline resonators were designed in ANSYS High-Frequency Structure Simulator (HFSS). The filter was designed for a 60 mil-thick Rogers RO 4350B substrate with a dielectric constant, ϵ_r, of 3.66 and a loss tangent, $\tan\delta$, of 0.0031. The design recommendation in Matthaei states that characteristic impedances around 70 Ω provide good performance for combline filters [36]. The characteristic impedance of the microstrip line used for the resonators was chosen to be 74 Ω. This value was chosen based on the design recommendation and for its closeness to the real part of the input impedance of the original antenna element, a half-wave dipole, which is 73 Ω [6]. Using the TXLine tool in National Instruments' Microwave Office (MWO, also known as AWR), the width of the microstrip resonators, w_r, was determined to be 1.62816 mm. The microstrip with its varactor diodes was modeled in HFSS and an Eigenmode simulation was used to determine the appropriate length.

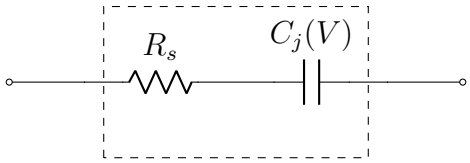

Figure 3.3: Series RC varactor model used in HFSS

The varactors were modeled using *Lumped RLC* boundaries in HFSS. A simple series RC varactor model, shown in Figure 3.3, was used to keep simulation run-times reasonable. In Figure 3.3, $C_j(V)$ is the junction capacitance of the varactor and R_s is the series resistance from the varactor contacts and semiconductor [52]. The varactor selected for this design was the Skyworks SMV1405-040LF [53]. This diode can provide capacitance in the range of 0.63 pF to 2.67 pF, which makes the center capacitance 1.65 pF. Thus, the resonators were designed to resonate at the design center frequency of 2.45 GHz when the varactors were biased for a capacitance of 1.65 pF to allow the filter to tune above and below the nominal center frequency. Two varactors are connected in series from the end of the microstrip to a grounding via, which allows the bias voltage for the varactors to be applied to the pad between them. However, this also halves the total loading capacitance, as the varactors are connected in series. Unless otherwise noted, all capacitances referenced in this work will refer to the junction capacitance of a single varactor, not the total loading capacitance. The Eigenmode simulations from HFSS indicated that the loaded resonators should have a length, ℓ_r, of 6.4 mm. The HFSS model for the resonator Eigenmode simulation is shown in Figure 3.4.

The values of the dimensions illustrated in Figure 3.4b are given in Table 3.3. Once the resonator design was complete, the effect of varying the loading capacitance was studied to ensure that the resonant frequency could be tuned. The center frequency of the resonator as a function of the loading capacitance is shown in Figure 3.5.

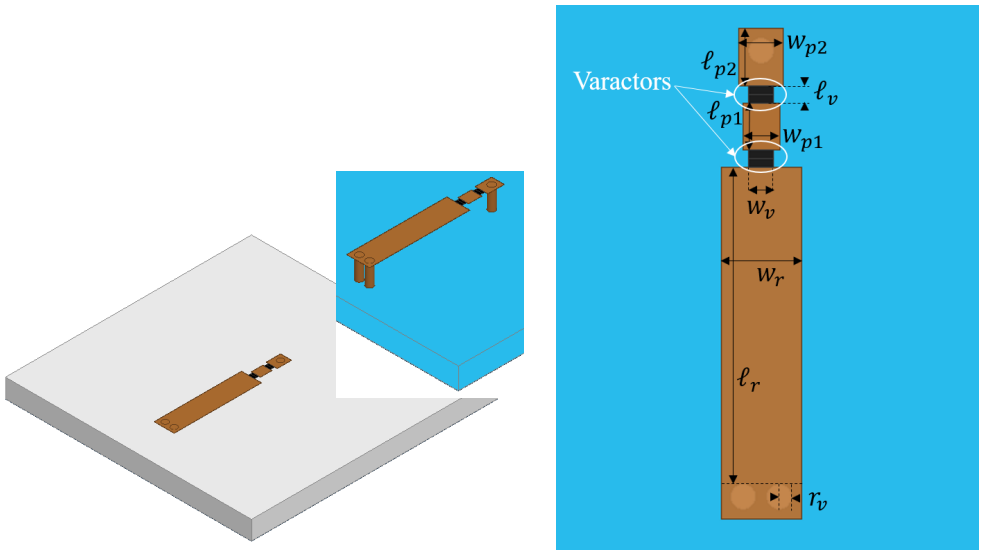

(a) (b)

Figure 3.4: HFSS model for resonator design. (a) Isometric view of resonator simulation model; substrate made transparent to show grounding vias in inset. (b) Top-down view of resonator with dimensions illustrated.

Table 3.3: Resonator Dimensions

Dimension	Value
w_r	1.62816 mm
ℓ_r	6.4 mm
w_d	0.5 mm
ℓ_d	0.35 mm
w_{p1}	0.75 mm
ℓ_{p1}	0.94 mm
w_{p2}	0.9 mm
ℓ_{p2}	1.17 mm
r_v	0.25 mm

The circuit model curve in Figure 3.5 was generated by extracting the equivalent circuit model of the resonator. The loading capacitance adds in parallel with the inherent capacitance of the resonator, as the capacitance of the resonator circuit model arises from the electric fields between the microstrip line and the ground plane and the loading capacitance stores additional electrical energy between the

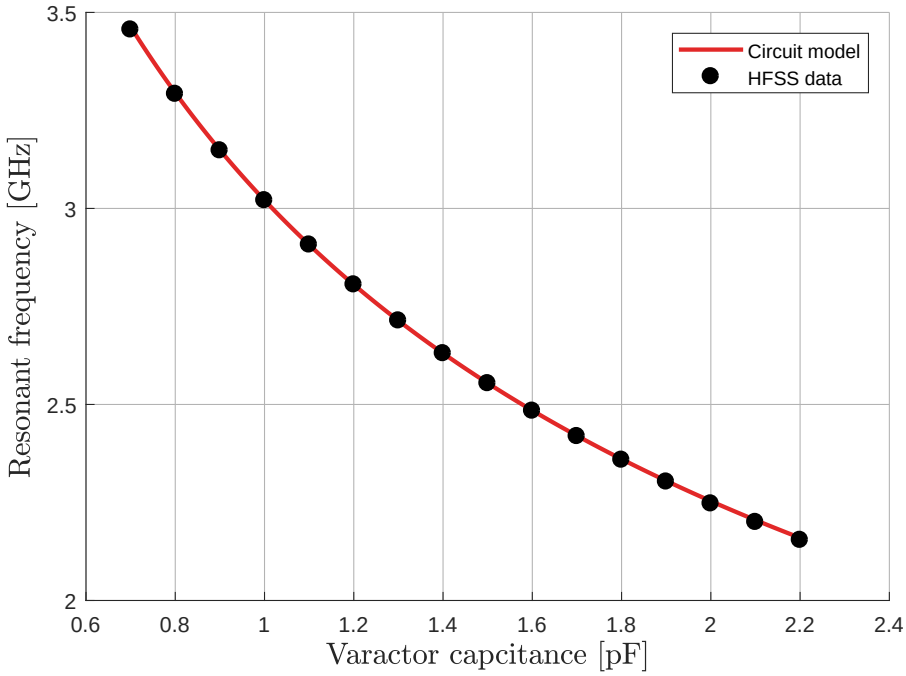

Figure 3.5: Variation of resonator center frequency with single-varactor capacitance

same circuit nodes. A transmission line model of the capacitive loading is shown in Figure 3.6, where C_0 is the inherent capacitance of the line and C_L is the total loading capacitance.

The circuit model can be extracted from the simulation data using a method similar to that of Luther *et al.* [45]. If multiple loading capacitances are used, the equivalent circuit model values can be extracted by comparing two different loading values. First, the equivalent inductance is extracted by comparing the resonant frequencies of two different loading values and the difference between the loading

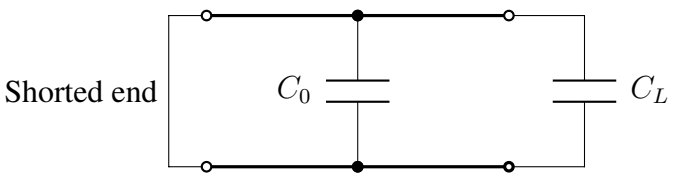

Figure 3.6: Transmission line model for the capacitive loading of the resonators

values using (3.1)-(3.4) as follow:

$$\omega_1^2 = \frac{1}{L(C_0 + C_{L1})} \rightarrow L(C_0 + C_{L1}) = \frac{1}{\omega_1^2} \tag{3.1}$$

$$\omega_2^2 = \frac{1}{L(C_0 + C_{L2})} \rightarrow L(C_0 + C_{L2}) = \frac{1}{\omega_2^2} \tag{3.2}$$

Since the total loading capacitances are under the designer's control, let $C_{L2} = C_{L1} + \Delta C$ and let $\Delta C > 0$, such that C_{L2} is greater than C_{L1}. Then substitute this value for C_{L2} into (3.2):

$$\begin{aligned} L(C_0 + C_{L1} + \Delta C) &= \frac{1}{\omega_2^2} \\ L(C_0 + C_{L1}) + L\Delta C &= \frac{1}{\omega_2^2} \\ \frac{1}{\omega_1^2} + L\Delta C &= \frac{1}{\omega_2^2} \end{aligned}$$

$$L = \frac{1}{\Delta C}\left(\frac{1}{\omega_2^2} - \frac{1}{\omega_1^2}\right) \tag{3.3}$$

The condition $C_{L2} > C_{L1}$ ensures that $\omega_2 < \omega_1$, and therefore $\frac{1}{\omega_2^2} > \frac{1}{\omega_1^2}$. This guarantees that the difference term on the RHS of (3.3) is positive and, therefore, results in a physically realistic inductance. Once L has been extracted using (3.3), C_0 can be found by solving (3.1) or (3.2):

$$C_0 = \frac{1}{L}\left(\frac{1}{\omega_j^2} - LC_{Lj}\right) \tag{3.4}$$

Because more than two loading capacitances were simulated, multiple circuit models are possible depending on which two points are used for the extraction procedure. The permutations that satisfy the condition $C_{L2} > C_{L1}$ were tested using MATLAB and the circuit model that produced the best fit to the simulated data points in a least-squared-error sense was selected. The resulting circuit model

had inductor and capacitor values of 4.425 nH and 1.272 pF, respectively. The extracted circuit model matches the simulated data very well; the norm of the errors was approximately 13.8 MHz. The circuit model can be used to determine the loading capacitance required for the combline resonators to achieve a given resonant frequency. The resonant frequency will control the center frequency of the filter and filtenna, so the circuit model of the resonator will be useful for tuning the later designs to a given center frequency.

Note that the circuit model extraction procedure described here is valid for both series and parallel resonators, provided that the loading capacitance is parallel to the inherent capacitance. This is due to the fact that the resonant frequency of a microwave resonator is given by (2.14) regardless of the resonator type [5].

Coupling

The internal coupling and external quality factor for the filter were extracted using HFSS. The internal coupling was extracted using Eigenmode simulations to characterize the characteristic modes of two resonators as the distance between them was varied. The HFSS model for the internal coupling extraction is shown in Figure 3.7.

The coupling between the resonators was calculated for multiple values of resonator separation, d_{12}. The resulting design curve is shown in Figure 3.8. The points around the desired coupling value were fit with a polynomial so that the resonator separation could be calculated. From the polynomial, the resonator separation was calculated to be $d_{12} \approx 2.12$ mm.

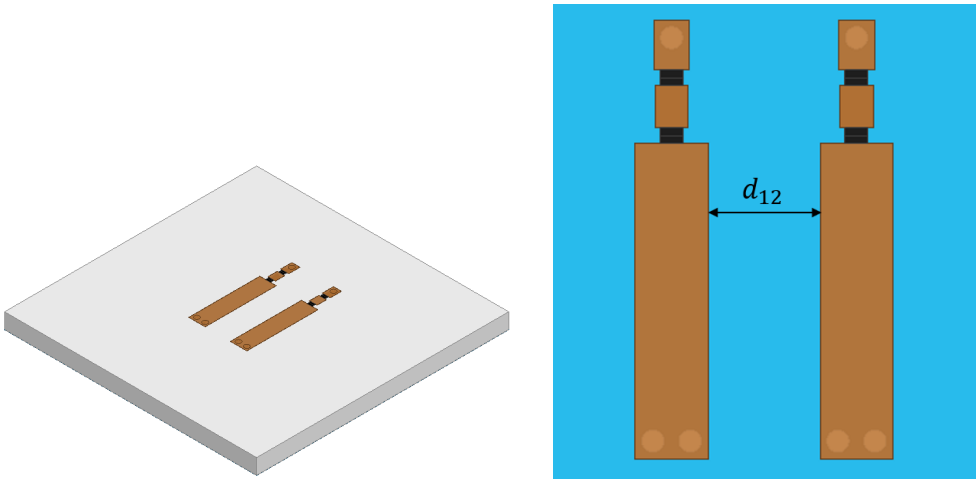

(a) (b)

Figure 3.7: HFSS model for internal coupling extraction. (a) Isometric view of Eigenmode simulation model. (b) Top-down view of model with d_{12} illustration.

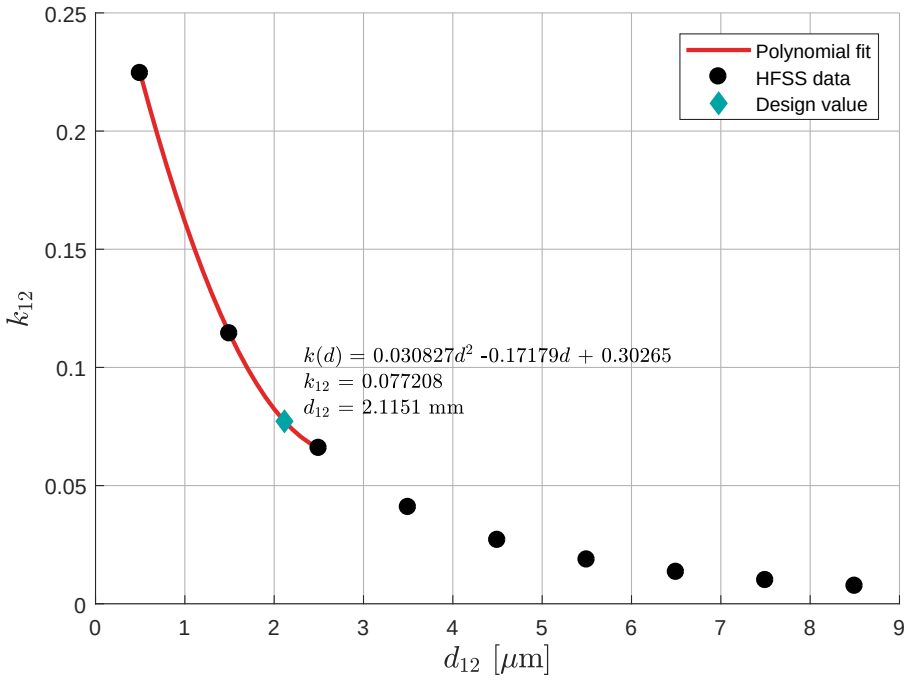

Figure 3.8: Internal coupling design curve extracted using HFSS

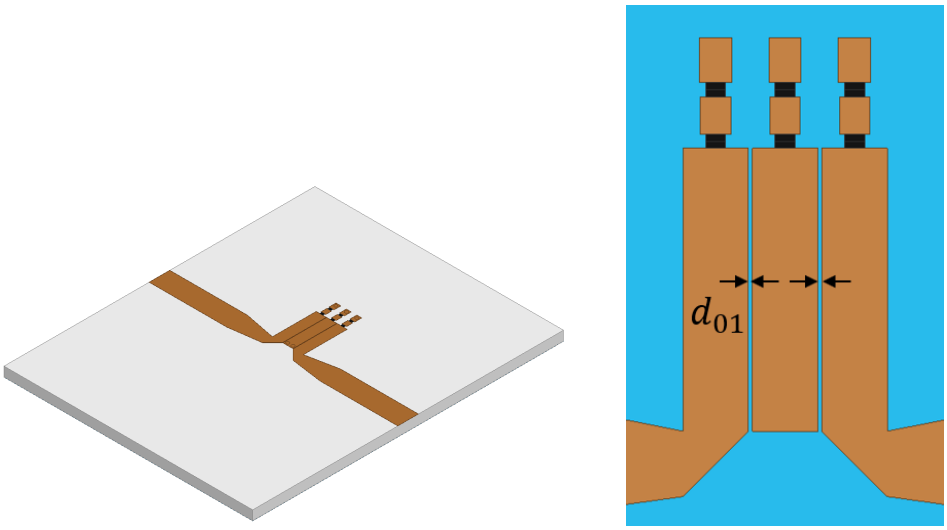

(a) (b)

Figure 3.9: HFSS model for external quality factor extraction. (a) Isometric view of simulation model. (b) Top-down view of model with d_{01} illustration.

The external quality factor was also extracted using HFSS. The doubly-loaded resonator method described in [12] was used; the HFSS model for the external quality factor extraction is shown in Figure 3.9.

The external quality factor for each d_{01} value was calculated from the HFSS results and the external coupling design curve, shown in Figure 3.10, was generated. A polynomial was fit to the data and the port-resonator separation was determined to be $d_{01} \approx 394$ μm. The extracted spacing values were used to model a full second-order combline filter. High-impedance DC bias lines with 1 MΩ SMD resistors were added so that bias voltages could be applied to the pads between the varactor diodes. The HFSS model for the combline filter is shown in Figure 3.11.

The substrate width, w_s, is 40 mm, and the substrate length, ℓ_s, is 30 mm. The input and output lines at the edges of the board were designed to have characteristic impedances of 50 Ω. The bias lines were designed to have minimal effect on the performance of the filter, which meant that the lines needed to be as narrow as

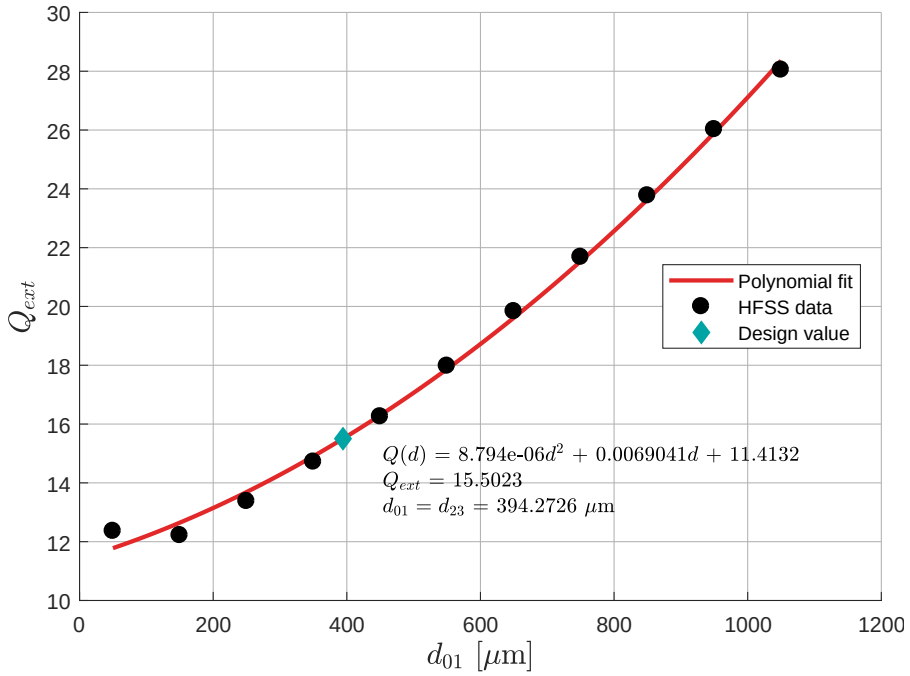

Figure 3.10: External quality factor design curve extracted from HFSS

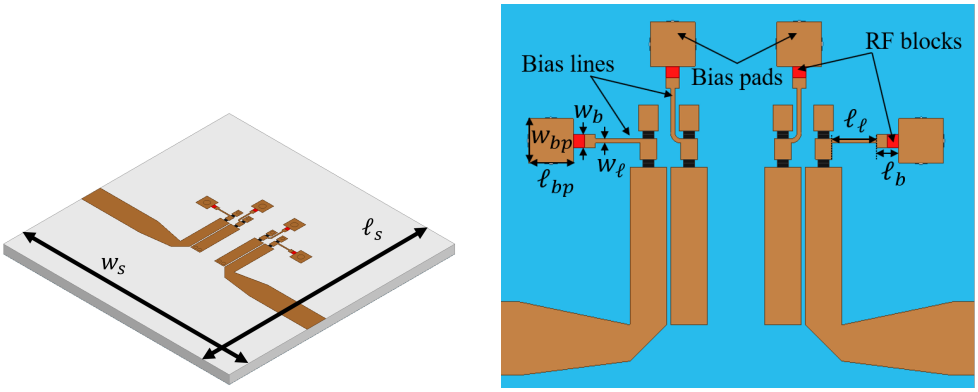

(a) (b)

Figure 3.11: Combline filter model. (a) Isometric view of simulation model with substrate dimension illustrations. (b) Top-down view of model with illustration of dimension parameters.

possible so that the RF path would present the highest possible input impedance. The width of the lines was set to 200 μm, which was as narrow as the planned fabrication process, printed circuit board (PCB) milling, would comfortably allow. Making the bias lines any narrower would run the risk of accidental line break-

age during PCB milling or soldering. The lengths of the bias lines would typically be set at $\lambda_g/4$, where λ_g is the guided wavelength on the bias line at the design frequency. Using a quarter-wavelength transformer would allow the bias line to be shorted to RF ground, which would then appear as an open circuit at the input of the bias line. However, due to the fact that this design is tunable, a quarter-wavelength transformer is not applicable, as the fixed line length would no longer be a quarter wavelength long as the center frequency of the filter was tuned away from the nominal center frequency. Thus, the bias lines were terminated with large SMD resistors connected to bias pins which were isolated from RF ground to present a near open circuit at the input of the lines. The line length had to be long enough to place the bias pins far enough from the resonators and the input and output lines to avoid impacting the filter performance. Simulations showed that making the lines too long introduced additional coupling which significantly degraded the performance of the filter, so the final line length was chosen by comparing simulated results of various lengths and selecting the one that had a minimal impact on the filter's performance. The values of the dimensions defined in Figure 3.11 are given in Table 3.4. Other dimensions are as defined in Table 3.3.

Table 3.4: Combline Filter Dimensions

Dimension	Value
w_s	40 mm
ℓ_s	30 mm
w_ℓ	200 μm
ℓ_ℓ	2 mm
w_b	0.6 mm
ℓ_b	1 mm
w_{bp}	2 mm
ℓ_{bp}	2 mm

It was found that the loading capacitance on the input and output ports should be larger than that of the resonators to improve the input and output coupling. This corresponds to the ports being electrically longer than the resonators, as mentioned in [12]. Loading the ports with larger capacitances provided better performance. Based on a suggestion by Nicholas Peccarelli, it was found that maintaining a constant ratio of port loading capacitance to resonator loading capacitance helped achieve center frequency tuning; the relationship between the port loading capacitance and the resonator loading capacitance is given by

$$C_p = C_r \frac{C_{p0}}{C_{r0}} \tag{3.5}$$

where C_p is the port loading capacitance, C_r is the resonator loading capacitance, and C_{p0} and C_{r0} are the port and resonator loading capacitances, respectively, that tune the filter to a center frequency of 2.45 GHz. Since the port loading capacitance must be larger than the resonator loading capacitance, C_{p0} is greater than C_{r0}. This also implies that when the center frequency of the filter is tuned by changing the loading capacitance, the port loading capacitance will reach the maximum loading capacitance the varactors can provide before the resonators will; thus, the port loading capacitance places an upper limit on the resonator loading capacitance. The limit on C_r is obtained by substituting the maximum loading capacitance the varactors can provide for C_p and solving for C_r:

$$C_{r,max} = C_{max} \frac{C_{r0}}{C_{p0}} \tag{3.6}$$

For the Skyworks SMV1405-040LF varactors used in this work, the maximum available capacitance is 2.67 pF. C_{p0} was chosen to be 1.9 pF at the center frequency, which limits the maximum resonator loading capacitance to approximately

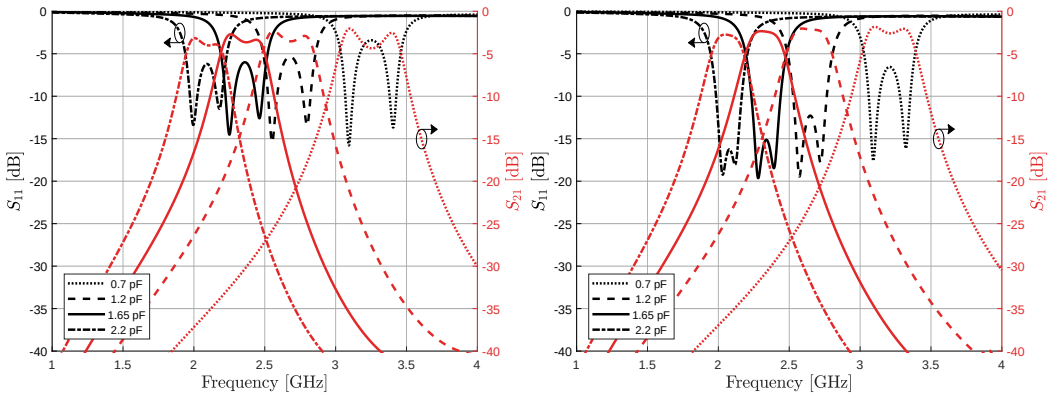

(a) (b)

Figure 3.12: Combline filter performance for multiple varactor capacitances using (a) raw extracted design values and (b) adjusted design values.

2.32 pF. This value provided good performance without severely limiting the center frequency tuning range.

The simulated response of the filter using the extracted values of d_{01} and d_{12} is shown in Figure 3.12a. The extracted values of d_{01} and d_{12} did not achieve the return loss ripple specification, so the filter model was adjusted to improve performance. The adjusted values are $d_{01} = 200$ μm and $d_{12} = 2.6$ mm. Further, the length of the input and output coupling lines was increased by 0.2 mm. This adjustment was made based on the findings related to the relative loading of the coupling line and resonators discussed previously. Increasing the coupling line loading effectively increases the lines' electrical lengths, so a similar performance improvement can be achieved by increasing the physical length of the lines. The performance of the adjusted design is shown in Figure 3.12b.

The filter using the raw extracted spacings has a tuning range of 1.16 GHz (43.4%), while the adjusted filter has a tuning range of 1.13 GHz (42.8%). The 15 dB return loss bandwidth, return loss ripple, and insertion loss at the center frequency of the adjusted filter as functions of center frequency are shown in Figure 3.13.

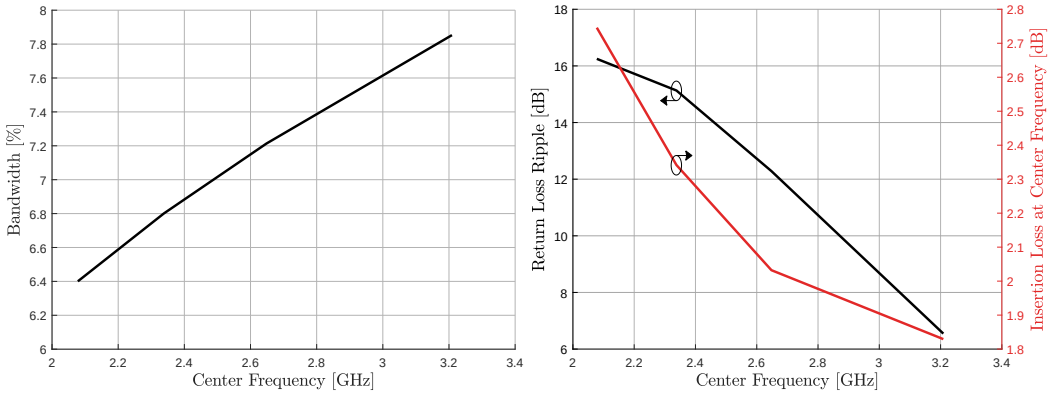

(a) (b)

Figure 3.13: Summary of simulated filter performance. (a) Bandwidth as a function of center frequency. (b) Return loss ripple and insertion loss as functions of the filter center frequency.

Even after the design was adjusted to improve the performance, the filter response still degraded at higher frequencies. The bandwidth varied from 6.4% to 7.85% as the filter tuned to higher center frequencies, indicating that the internal coupling increases with the center frequency. The return loss ripple decreased as the filter tuned to higher frequencies, indicating that the external coupling was too low. This means that maintaining a constant port-to-resonator loading capacitance ratio did not provide the correct external coupling as the filter tuned. This could be remedied by adjusting the port loading capacitance further, but this was left as a task to be accomplished during measurement of the fabricated filter as the port loading can be quickly adjusted by changing the port bias voltage on the real filter. This option was chosen instead of running more time-consuming simulations with discrete capacitance values. Thus, the design of the filter was deemed an acceptable baseline for the filtenna design.

3.2 Microstrip Patch Antenna

The antenna element chosen for this work was a microstrip patch. The original design concept used coupled halfwave resonators for the filter design and a halfwave dipole for the antenna, but the resonators were changed to combline resonators to reduce the design size and add tunability. The antenna element was changed to a narrow patch for the sake of design simplicity and space savings, and to maintain structural similarity to the resonator elements.

The microstrip patch antenna has a sinusoidal current distribution that is maximum at the center of the patch's length and zero at the ends of the patch, as is required at an open-circuit boundary. Thus, the voltage along the length of the patch also varies sinusoidally with maxima at the ends of the patch and a zero in the center. The patch's simplicity and ease of fabrication make it an ideal candidate for this filtenna design. Further, the patch can easily be made tunable by loading it with varactors at its ends like the combline resonators.

3.2.1 Antenna Design

The initial patch design had the same width as the filter resonators and was fed with a proximity-coupled line on a single-layer substrate. The length was determined using the TXLine calculator in MWO, then the patch was loaded with varactors at either end and its length was reduced until the simulated results indicated resonance at 2.45 GHz. Like the combline resonators, a biasing pad was placed between two varactors and the second varactor was connected to ground through a via. As the design was refined, the patch was made wider to increase the gain. Because the patch was loaded at its ends, the varactors were capturing and storing some of the fringing fields responsible for the patch's radiation, causing a reduction in efficiency and gain. Thus, widening the patch increased the available aperture for

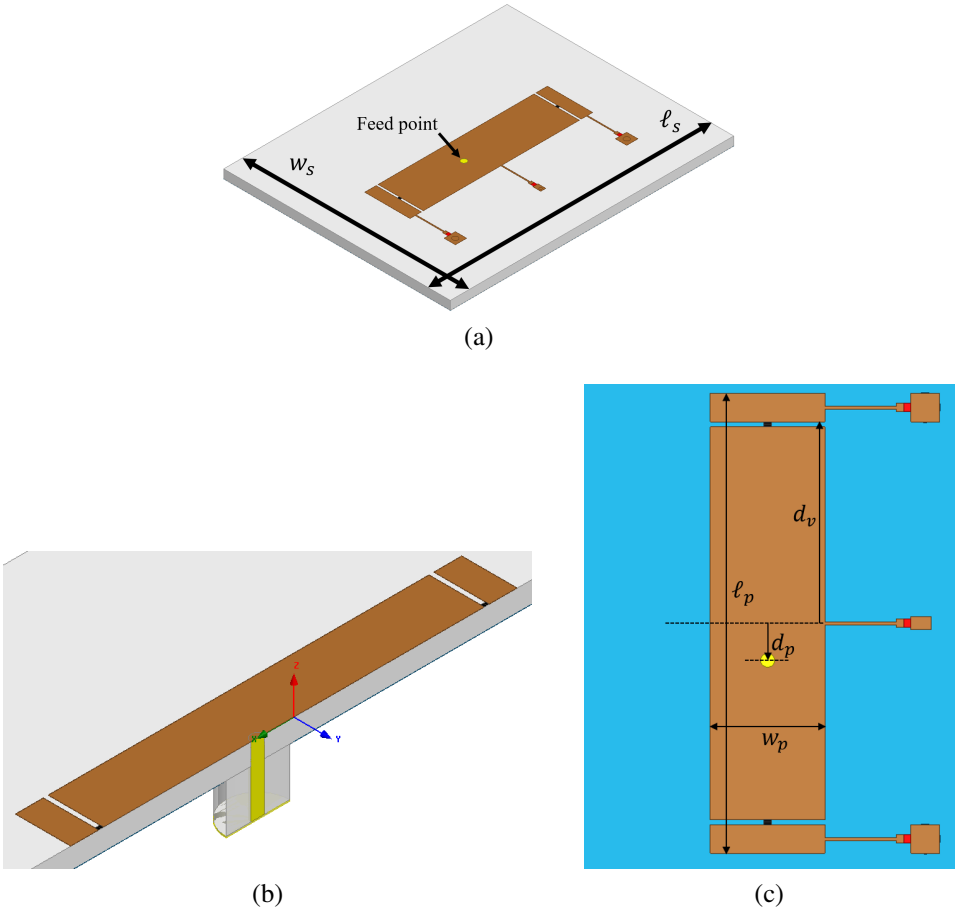

Figure 3.14: The segmented narrow microstrip patch. Varactors and SMD resistors are represented as in Figure 3.11b. (a) Isometric view with illustrations of substrate dimensions. (b) Cross-section along length of patch to show coax feeding structure in backplane. (c) Top-down view illustrating dimensions of patch.

fringing electric fields to radiate away from the antenna. However, even after the patch was widened, the end-loaded configuration severely degraded the efficiency of the antenna; the vias at each end of the patch provided a path for currents to flow in a loop across the antenna and then along the ground plane. The RF energy was dissipated in the ground currents and little energy was radiated. To remedy this problem, Dr. Jessica Ruyle suggested that the patch could be divided into three segments and diodes could then be placed across the gaps between the segments, as shown in Figure 3.14.

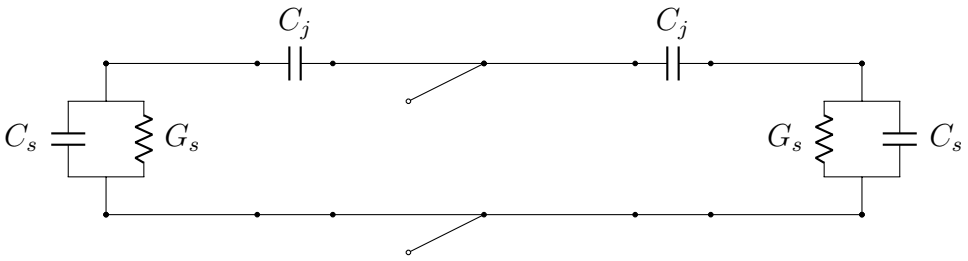

Figure 3.15: Transmission-line model of the series-loaded patch [44]

The feed structure was also changed from a coupled line to a 50-Ω coax probe for ease of input impedance matching. The location of the probe along the length of the patch was adjusted to match the input impedance of the patch to the impedance of the feed structure, as is common with microstrip antennas [44].

As a result of the varactors being placed across gaps between patch segments, the loading capacitance of the patch was no longer in parallel with the inherent capacitance of the patch. The series-loaded varactor tuning mechanism used for this patch design achieves tuning by providing a variable impedance between the inner patch segment and the outer segments. The transmission line model for the series-loaded patch is shown in Figure 3.15. G_s is the conductance of the radiating slot formed by the end of the patch and the ground plane, and C_s is the capacitance of the slot [44]. The series impedance of a capacitor is $1/(j\omega C)$; thus, at a given frequency, sufficiently small loading capacitances, C_j, appear as open circuits and sufficiently large capacitances appear as short circuits. Therefore, the center frequency of the patch will be between two limiting resonant frequencies: the resonant frequency of the full length of transmission line when the center and end segments are connected, and the resonant frequency of the center segment coupled to the end segments when the segments are disconnected. The equivalent transmission line models are shown in Figure 3.16.

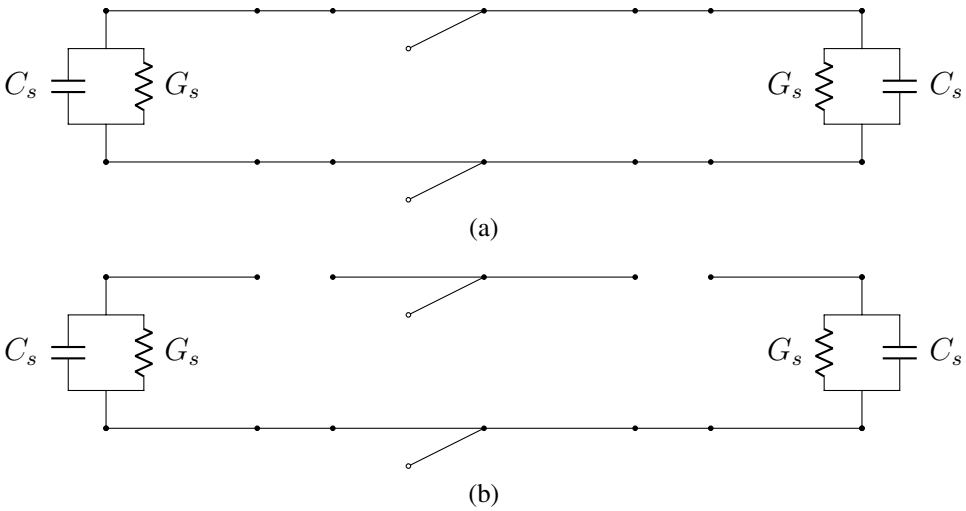

Figure 3.16: Limiting cases of varactor loading. (a) Large capacitance values appear as short circuits. (b) Small capacitance values appear as open circuits [44].

Given that the first case makes the antenna electrically longer, the resonant frequency should decrease as the varactor is biased to provide higher capacitance and appears more like a short circuit. When the varactor is biased for low capacitance and appears closer to an open circuit, the resonant frequency will be primarily determined by the length of the center segment. Further, the tuning range of the patch should be directly proportional to the ratio of the full length to the center segment length. As the cuts separating the segments of the patch are moved closer to the center of the patch's length, the center segment will be a small fraction of the total length. This means that the upper resonant frequency will increase and move farther from the lower resonant frequency as the cuts move toward the center, thereby increasing the tuning range.

A parametric study was conducted to observe how the center frequency, tuning range, and broadside gain of the patch varied as a function of the location of the segment cuts for a fixed patch length. The gain simulated here is the efficiency-directivity product, not the realized gain. The gain without regard for the input matching was used to study how the changes in the antenna geometry affect the

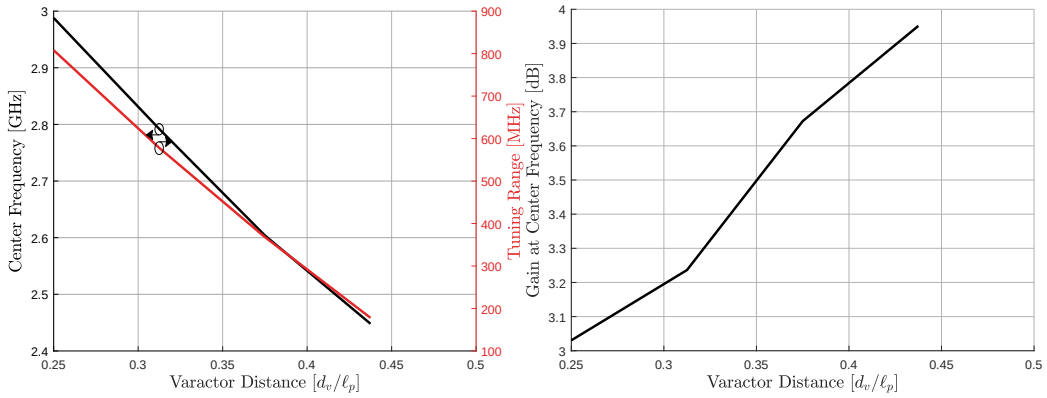

(a) (b)

Figure 3.17: Results of the varactor position parametric study. (a) Variation of center frequency and tuning range as functions of varactor placement. (b) Variation of gain as a function of varactor placement.

energy-directing properties of the antenna. It was expected that the input matching would degrade as the segment cuts moved, and that the input match would be re-established by adjusting the position of the feed probe after the segment cut locations were chosen. Thus, including the effects of the input match would skew the results of the study. The results are shown in Figure 3.17.

As expected, the study indicates that the tuning range decreases as the cuts move toward the ends of the patch and the center segment becomes longer. The resonant frequency also decreases as the cuts move toward the ends, reflecting the fact that the center segment becomes longer as the cuts move outward. The gain varied by approximately 0.92 dB, so the primary tradeoff was between miniaturization and tunability. To maintain a relatively small footprint and achieve higher gain, the patch length was fixed at 32.25 mm and the cuts were placed at $\frac{7}{16}\ell_p$, which should provide 178 MHz (7.17%) of tuning bandwidth and higher gain than the other configurations. The dimensions defined in Figure 3.14 are given in Table 3.5.

Table 3.5: Dimensions of Microstrip Patch Antenna

Dimension	Value
ℓ_p	32.25 mm
w_p	8 mm
d_v	14.109375 mm
d_p	2.6 mm
ℓ_s	50 mm
w_s	40 mm

The ground plane of the patch was kept relatively small in anticipation of the integration of the patch into the filtenna. The goal here was to maintain a small design footprint when the patch was integrated into the filtenna; thus, designing and tuning the patch's performance on a smaller ground plane prevented significant performance impacts when the patch was integrated into the filtenna.

Bias lines and pins were included in the patch model earlier than those in the filter model, so the effects of the bias circuitry could be accounted for before the patch was finely tuned. The design is configured such that bias voltages will be applied to the end segments and the center segment is connected to DC ground through a high-impedance line. Thus, the cathode of each diode was connected to an end segment and the anodes to the center segment. The bias line for the center segment is connected to the center of the length of the segment, which is the location of the current maximum on the patch. Generally, it is preferred to connect the bias lines to points on the antenna structure where the current is low so that minimal RF current can flow through the bias circuitry. In this case, the bias line was placed in the center for the sake of symmetry; placing a single bias line at one of the ends of the center segment would cause an uneven perturbation of the antenna patterns. Bringing the center bias line in proximity with either of the end segment bias lines could have also caused unwanted coupling. This would affect the tuning of the patch as coupling between bias lines at one end of the patch would change how the

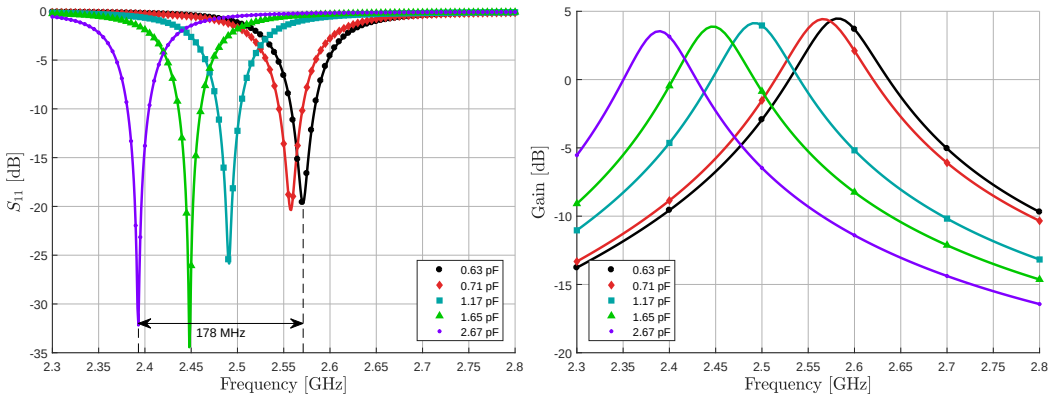

(a) (b)

Figure 3.18: Simulated performance of microstrip patch tuned to various center frequencies. (a) Return loss. (b) Realized gain.

center segment is connected to the end segment at that end of the patch. Thus, the center segment bias line was left at the location of the current maximum to maintain symmetry and avoid potential coupling issues.

Having determined the geometry of the antenna, the performance of the antenna over its tuning range was simulated. The simulated return loss and gain of the patch for various tuning capacitances are shown in Figure 3.18. The tuning bandwidth is 178 MHz, or 7.17%, as indicated by the varactor placement study. The variation of the impedance bandwidth, return loss at resonance, and gain of the patch as functions of the center frequency is shown in Figure 3.19. The patch has a return loss greater than 10 dB, the level at which an antenna is considered matched to its feed line, across the tuning range, and the gain varies by less than 1 dB. The 10 dB return loss bandwidth varied from approximately 0.96% to 1% across the tuning range of the patch.

While the antenna is matched over the tuning range, the return loss decreases with increasing center frequency. This de-tuning is a common problem with varactor-loaded microstrip antennas that degrades the antenna performance over the tuning range [47]–[51].

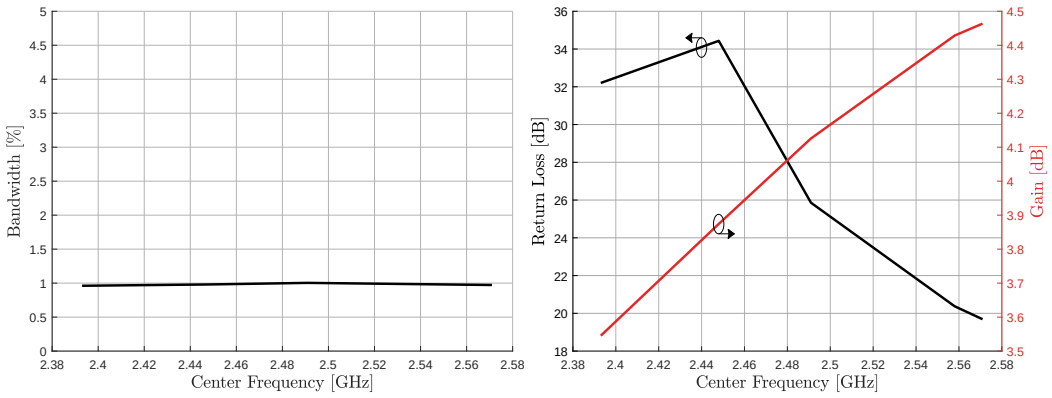

(a) (b)

Figure 3.19: Simulated performance parameters of the microstrip patch as functions of center frequency. (a) Impedance bandwidth. (b) Return loss at resonance and gain.

The patterns of the patch were simulated to study the effects of the frequency tuning. The simulated antenna patterns are shown in Figure 3.20. As the patch is planar and lies in the x-y plane, the E-plane is the x-z plane (or any plane containing the length of the patch), and the H-plane is the y-z plane.

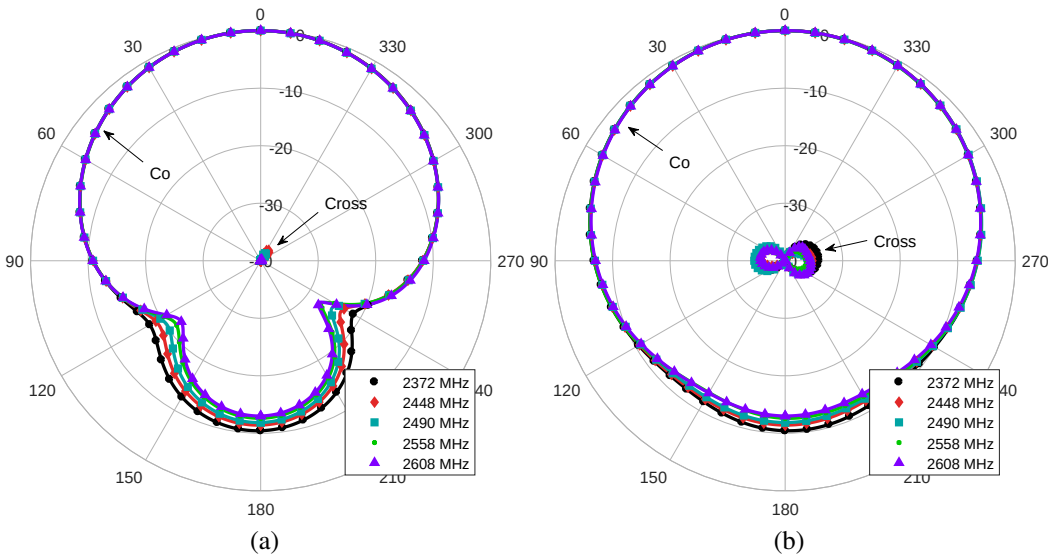

(a) (b)

Figure 3.20: Simulated antenna patterns of the microstrip patch tuned to various center frequencies. (a) E-plane patterns. (b) H-plane patterns.

Figure 3.20 shows that there is not significant variation in the patterns of the patch over its frequency tuning range. The co-polarized E-plane pattern shows some change in the backlobe of the antenna, but this will only reduce the broadside gain of the antenna as the backlobe increases, which is not of great concern. Thus, the patch design was deemed ready for integration into the filtenna.

3.3 Filtenna Design

Once the filter and patch designs were completed, they were integrated to form the filtenna. When the filtenna was designed, the bias lines used in the filter and patch were left intact so that the response of the filtenna could be adjusted to improve its performance and the addition of the bias lines later would not alter the behavior. First, the coupling between the resonator and the patch was extracted using Eigenmode simulations. The bias lines were not included in the Eigenmode simulation model as they should not affect the coupling significantly and their small features introduce numerous modes which obscure the even and odd modes arising from coupling. The model used for the coupling extraction is shown in Figure 3.21.

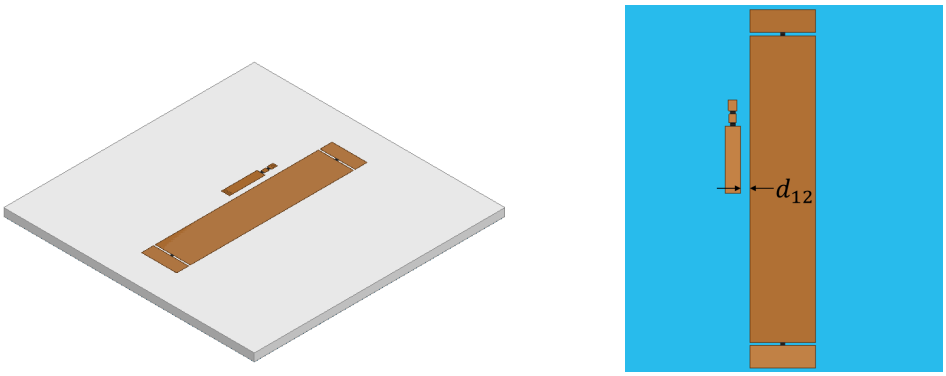

(a) (b)

Figure 3.21: Resonator-patch internal coupling extraction model. (a) Isometric view of simulation model. (b) Top-down view with illustration of d_{12}.

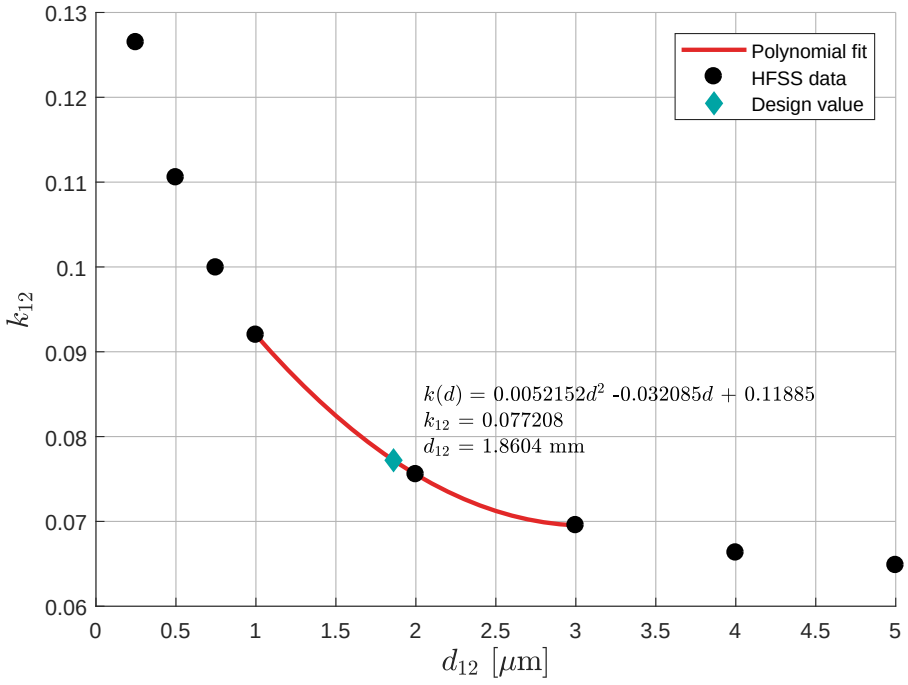

Figure 3.22: Internal coupling design curve for resonator and patch

The initial results showed that the coupling between the resonator and patch was too strong even as d_{12} was increased. So, the lengths of the patch and resonator were adjusted to bring the modes closer together. However, this meant that the resonator and patch no longer had the same resonant frequencies, so the internal coupling had to be calculated using a different equation [12]:

$$k = \frac{1}{2}\left(\frac{f_{01}}{f_{02}} + \frac{f_{02}}{f_{01}}\right)\sqrt{\left(\frac{f_{p2}^2 - f_{p1}^2}{f_{p2}^2 + f_{p1}^2}\right)^2 - \left(\frac{f_{02}^2 - f_{01}^2}{f_{02}^2 + f_{01}^2}\right)^2} \tag{3.7}$$

where f_{01} and f_{02} are the lower and upper resonant frequencies of the resonators, respectively, and f_{p1} and f_{p2} are the even and odd modes, respectively. The resulting extracted coupling is shown in Figure 3.22.

Issues were encountered during the Q_{rad} extraction procedure that resulted in insufficient useful data for the filtenna design. It was found that the internal coupling data provided a sufficient initial design that the lengths of the resonator and

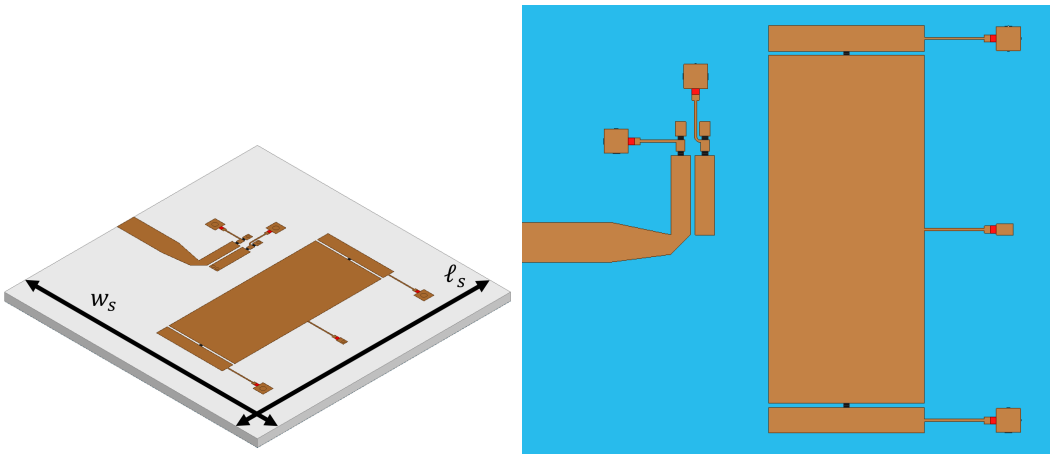

(a) (b)

Figure 3.23: Filtenna model. (a) Isometric view with substrate dimension illustrations. (b) Top-down view with dimensions as defined in previous figures.

patch, as well as the width of the patch, could be adjusted to achieve a second-order return loss response. The HFSS model of the filtenna is shown in Figure 3.23.

The substrate width, w_s, and length, ℓ_s, are both 50 mm. As with the filter, the input line is designed to have a characteristic impedance of 50 Ω. The final dimensions of the filtenna are shown in Table 3.6. All dimension variables match those provided in the dimension illustrations for the resonator, filter, and patch. Any dimensions not specified in Table 3.6 are the same as in the corresponding base design.

Table 3.6: Filtenna Dimensions

Dimension	Value
d_{01}	4.5 mm
d_{12}	395 μm
ℓ_r	5.8 mm
ℓ_d	33.9 mm
w_d	13 mm

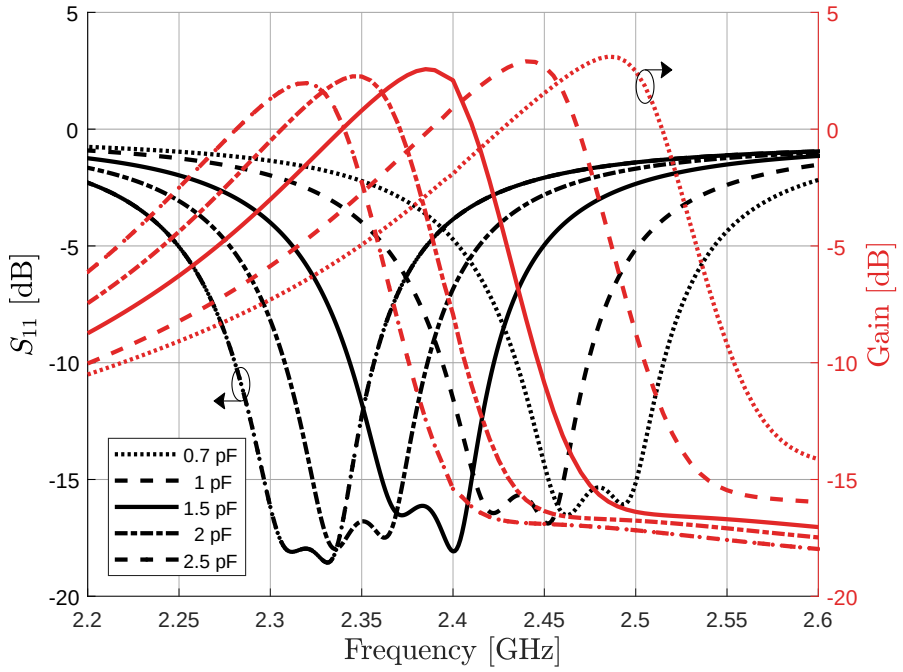

Figure 3.24: Simulated return loss and gain of the filtenna tuned to various center frequencies

The simulated filtenna return loss and gain, including center frequency tuning, are shown in Figure 3.24. The 15 dB bandwidth, return loss ripple, and gain as functions of center frequency are shown in Figure 3.25. Due to the adjustment of the resonator and antenna elements, the achieved response has a narrower bandwidth than the original filter, indicating that the internal and external coupling have changed. This is reflected in the increased spacings between the input line and resonator, and between the resonator and antenna. However, this difference does not detract from the primary goal of designing a filtenna with tunability for interference mitigation and cognitive radio applications. The simulated 15 dB fractional bandwidth is approximately 2% over the tuning range of the filtenna. The simulation indicates that the filtenna can tune its center frequency over a bandwidth of at least 161 MHz (6.71%). The full range of capacitances that the varactor can nominally provide, 0.63 pF to 2.67 pF, were not used in the filtenna simulation due to

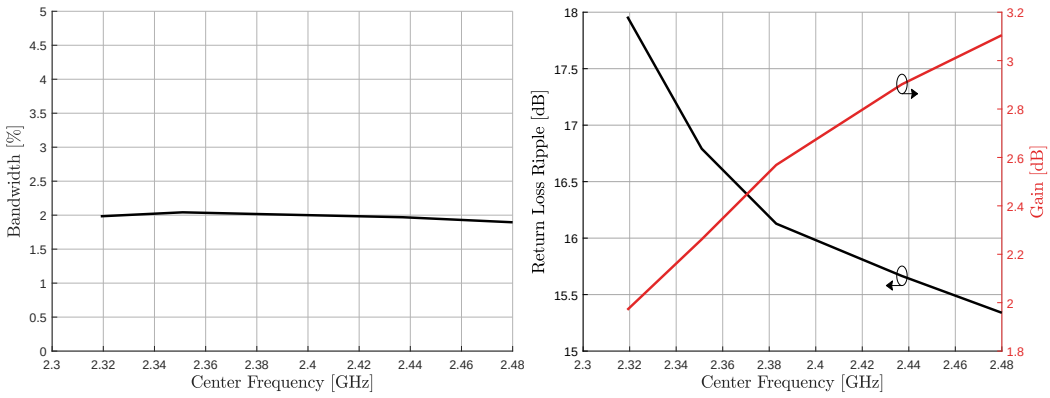

(a) (b)

Figure 3.25: Filtenna performance as functions of center frequency. (a) 15 dB bandwidth. (b) Return loss ripple and gain.

the fact that the correct resonator loading capacitance had to be found iteratively for each antenna loading capacitance. Instead, the patch was tuned using single-varactor capacitances in the range of 0.7 pF to 2.5 pF. Once it was verified that the filtenna could maintain its performance while tuning, further simulations were ceased. Thus, the realized filtenna should be able to tune over a wider bandwidth, likely close to the tuning bandwidth of the patch. A determination of the full tuning range of the filtenna was left to be accomplished using the fabricated filtenna, as little time is required to tune the realized design by adjusting the bias voltages of the varactors.

The antenna patterns for the filtenna are shown in Figure 3.26. As with the patch, the primary goal for the filtenna patterns is stable pattern shapes over the tuning range of the filtenna. The filtenna exhibits higher cross-polarization than the patch, which was expected given the presence of the filter resonator and input coupling line. However, the patterns do not change significantly over the tuning range of the filtenna, so the simulated pattern performance is acceptable.

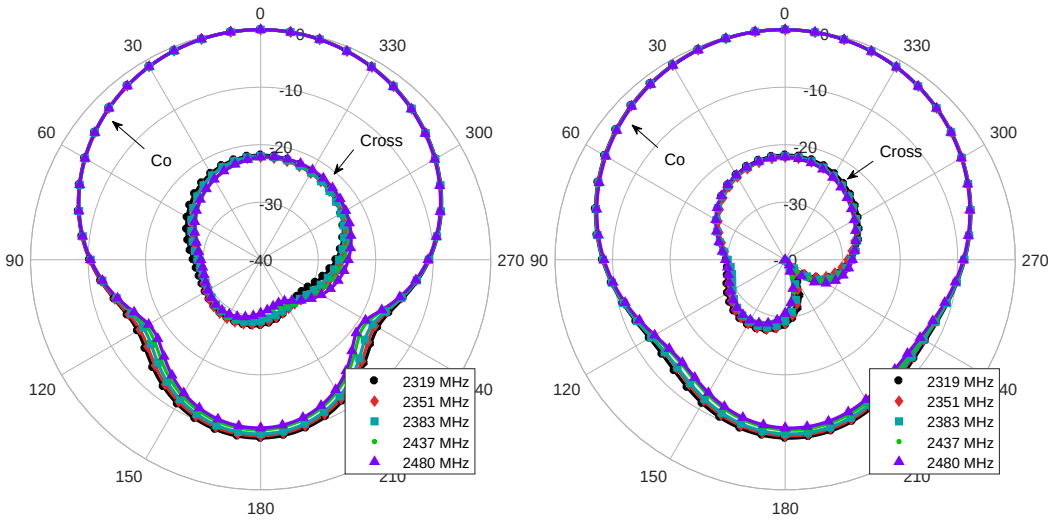

(a) (b)

Figure 3.26: Antenna patterns of the filtenna tuned to various center frequencies. (a) E-plane patterns. (b) H-plane patterns.

3.3.1 Comparison of Simulated Patch and Filtenna

The benefits of integrating the patch into the filtenna can be seen by comparing the performance of the designs as functions of center frequency, as shown in Figure 3.27.

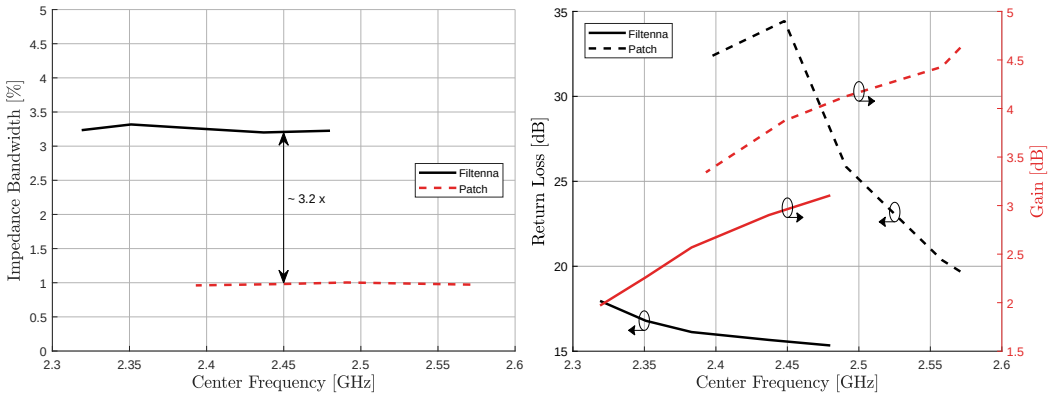

(a) (b)

Figure 3.27: Comparison of simulated patch and filtenna performance as functions of center frequency. (a) Impedance bandwidth. (b) Return loss and gain.

Figure 3.27a shows the 10 dB bandwidth of the patch and filtenna as functions of center frequency. The bandwidth of the filtenna is approximately 3.2 times wider than that of the patch. Because the patch dimensions changed during the filtenna integration, a model of the stand-alone patch with the same dimensions as the patch in the filtenna was simulated. The wider patch was found to have an impedance bandwidth of approximately 1.3% across the tuning range, which is slightly wider than that of the narrow patch, but the bandwidth of the filtenna is still approximately 2.46 times greater than that of the wide patch. Thus, the increased bandwidth of the filtenna is due primarily to the second-order filtering response and not the changes in the patch dimension.

The gains of the filtenna and narrow patch as functions of center frequency have similar slopes, but the gain of the filtenna is lower. This is due to losses in the input line and resonator that are not present in the reference patch, as well as radiative losses in the filter resonator, which is a known problem for un-enclosed microstrip resonators [54], [55]. This does not prevent accomplishment of the design goals, but it is a drawback of the single-layer, microstrip-based filtenna geometry.

Figure 3.27b shows that the return loss of the patch at resonance varies by approximately 15 dB over the tuning range, whereas the return loss ripple of the filtenna varies by approximately 2.5 dB. This is a significant improvement in the return loss variation typically seen in varactor-loaded microstrip antennas. The improved impedance matching is a result of the extra degrees of freedom offered by the tunability of the resonator and input coupling.

Based on this analysis, the simulated results indicate that the design achieves the project goals, so the design phase of the project was completed and fabrication commenced.

Chapter 4

Fabrication and Measured Results

4.1 Fabrication Method

The designs from Chapter 3 were fabricated in the Radar Innovations Lab (RIL) using PCB milling and via plating. Copies of each of the designs were placed in the HFSS Layout Editor to populate a 7" by 9" piece of substrate, as shown in Figure 4.1.

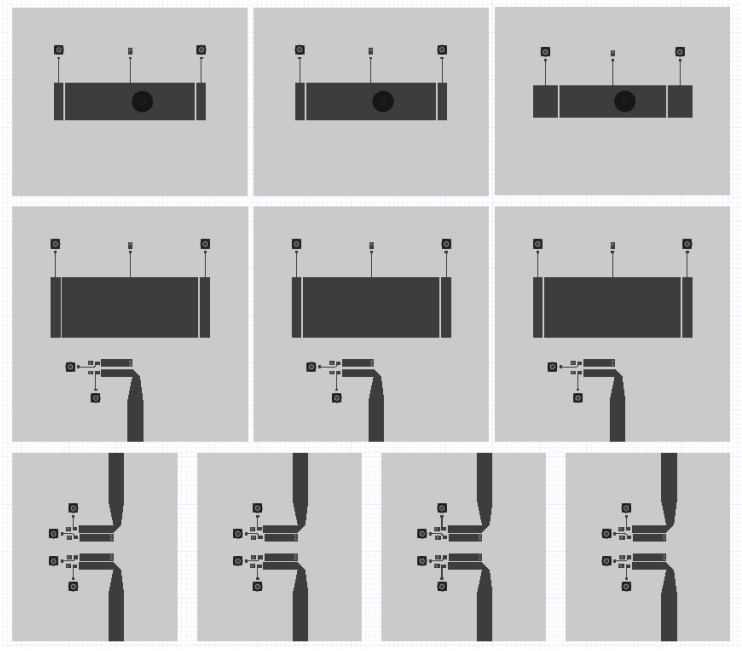

Figure 4.1: PCB layout file

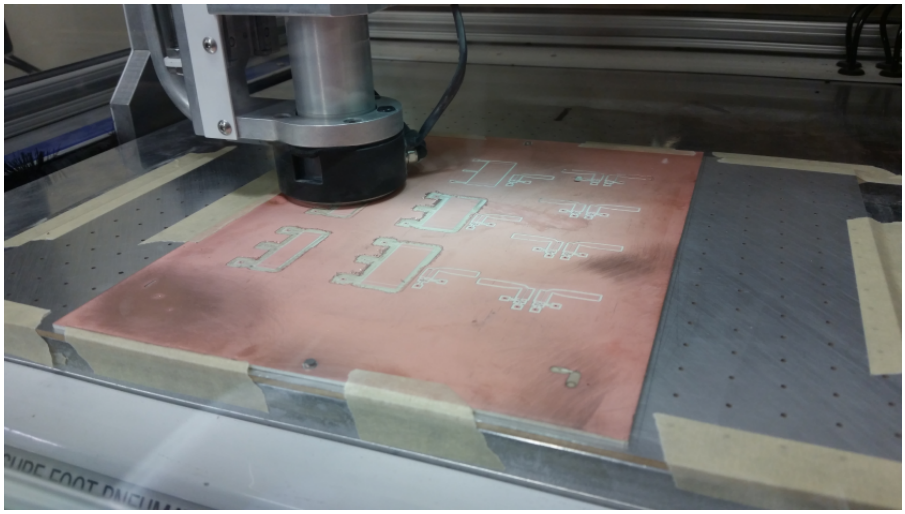

Figure 4.2: Substrate on the QCJ5 during the PCB milling process

The layout was used to produce Gerber and NCD Drill files for use with the T-Tech Quick Circuit QCJ5 PCB milling machine. The layouts were imported into T-Tech's Isopro software, which is the interface that allows users to control the QCJ5. First, the QCJ5 was used to drill the vias for each design. Once the vias were drilled, the board was plated with two copper plating processes. The first process, *electroless plating*, coated a 1.5 μm layer of copper on the non-metallic surfaces of the substrate. This step plated the vias that connect the resonators and some of the bias lines to the ground plane. The second process was standard *electroplating*, in which a 0.6 mil-thick layer of copper was deposited on all the metal surfaces of the substrate. This increased the thickness of the plating on the vias, as the electroless plating only deposited a very thin layer of copper. Once the plating was complete, Isopro was used to calculated tool paths for the QCJ5 to cut the designs into the copper of the substrate. The tool paths were checked for accuracy and then used to cut the designs. Figure 4.2 shows the substrate on the work surface of the QCJ5.

Once the designs were cut in the surface of the substrate, excess copper on the top layer was removed using a razor blade. PCB milling machines, including the

QCJ5, generally have a *rub-out* function that removes excess copper, but the designs had been sufficiently isolated from the excess copper that it was much faster and cleaner to peel the copper away manually. This also removed an issue that was encountered during the design cutting process: the depth of the cut made by the milling machine was inconsistent due to thickness variations and warping in the substrate, and due to issues with the height calibration of the QCJ5.

After the excess copper had been peeled away, the QCJ5 was used to cut each design out of the board using a contour routing bit. The designs were cleaned of dust and prepared for soldering. The combline filter required four bias pins, eight varactors, four bias resistors, and two end-launch RF connectors. The patch required two bias pins, two varactors, three resistors, and one coax probe connector. Finally, the filtenna required four bias pins, six varactors, five resistors, and one end-launch connector. The bias pins and connectors were soldered by hand, while the varactors were soldered using lead-tin solder paste and a re-flow oven. The completed designs are shown in Figure 4.3.

4.2 Measured Combline Filter Results

The S-parameters of the combline filter were measured on Agilent N5242A and N5225A performance network analyzers (PNAs). Different PNAs were used based on equipment availability at a given time. Because the input and output coupling lines were not connected to DC ground through vias, bias tees were connected to each port of the filter so that the lines could be connected to DC ground. This was necessary to apply a reverse voltage to the varactor diodes through the bias pads, as the second varactor on the end of each line was connected to DC ground on the other side of the bias pad. A bias tee allows a DC offset, or bias, to be added to an RF signal. The basic circuit for a bias tee is shown in Figure 4.4.

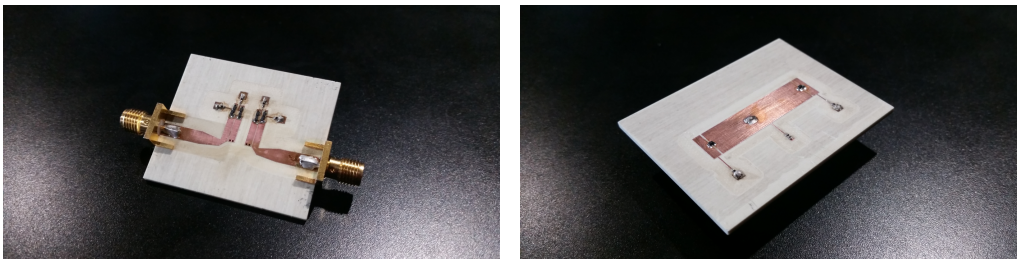

(a) (b)

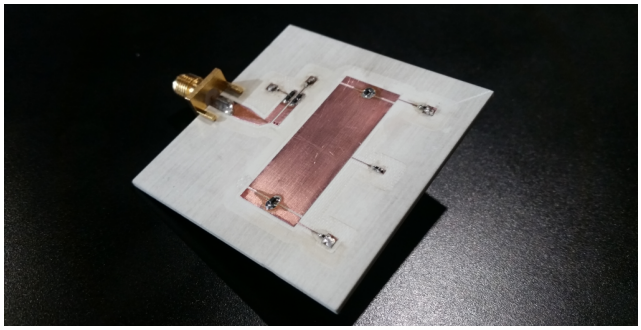

(c)

Figure 4.3: Fabricated designs. (a) Realized combline filter. (b) Realized narrow patch. (c) Realized filtenna.

The capacitor allows RF signals to pass but blocks DC signals. The inductor, likewise, blocks RF signals and passes DC signals. Thus, the RF and DC ports are isolated from each other and the combined RF signal with a DC offset appears at the port on the right.

A Rigol DP832A DC power supply was used to produce and control the DC bias voltages for the filter. In the first set of measurements, the input and output

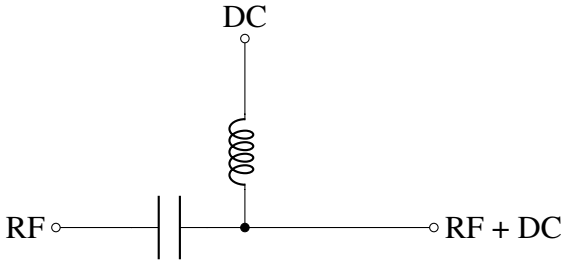

Figure 4.4: Basic circuit of a bias tee

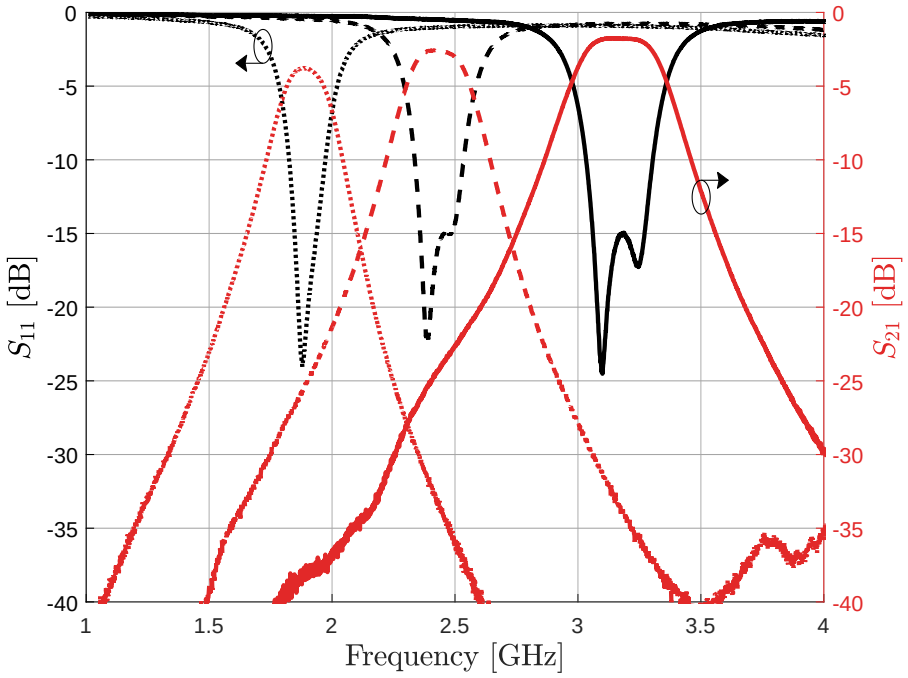

Figure 4.5: Filter response with resonators biased equally

port lines were biased with one voltage, V_p, and both resonators were biased with one voltage, V_r. The results of this configuration are shown in Figure 4.5.

The poles of the filter response collapse on each other as the filter is tuned to lower frequencies, indicating that the internal coupling between the resonators was too weak. The under-coupling between the resonators may have been due to changes in the fields around the resonators due to the presence of solder, which was not modeled in HFSS, and the varactors, which were modeled as sheets instead of three-dimensional objects. It is also possible that variations in the varactors caused the resonators to be de-tuned and moved the poles closer to each other. The under-coupling was remedied by applying independent bias voltages to each resonator, which allowed the resonators to be de-tuned from their shared center frequency or corrected the frequency shift due to the variations in the varactors. This corrected the coupling between the resonators and corrected the filter response. The measured results from independently biasing the resonators are compared against

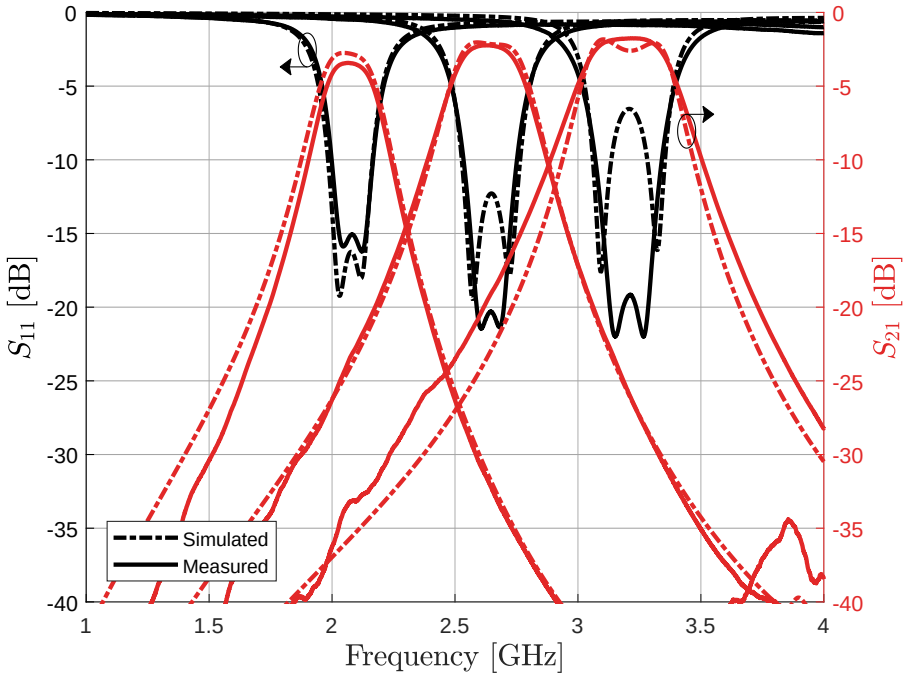

Figure 4.6: Comparison of simulated and measured filter S-parameters

simulated results in Figure 4.6. Independently biasing the resonators to correct the internal coupling significantly improved the filter's performance. By adjusting the bias voltages, the filter met or exceeded the original design specification across the simulated tuning range.

The tuning range of the fabricated filter was greater than that predicted by the simulation. The extremes of the filter's tuning range, shown in Figure 4.7, correspond to bias voltages of 0 V and 32 V, which are the biasing limits used for all the realized designs. The fabricated filter has a tuning range of approximately 1.6 GHz, or 62.7%, which is an increase of approximately 1.46 times the tuning range of the simulated filter. The realized filter has a wider tuning range than the simulated filter because the realized filter does not follow the constraint on the port loading capacitance given by (3.5). The loading of the ports in the realized filter was adjusted to provide the best match for each center frequency, rather than being determined by the resonator loading as in the simulations.

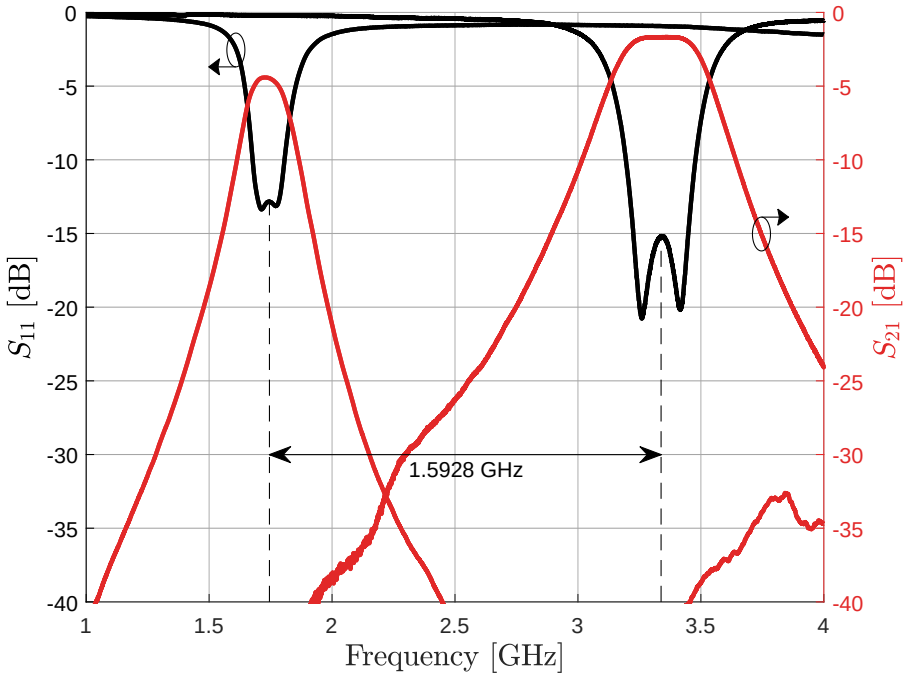

Figure 4.7: Full tuning range of fabricated filter

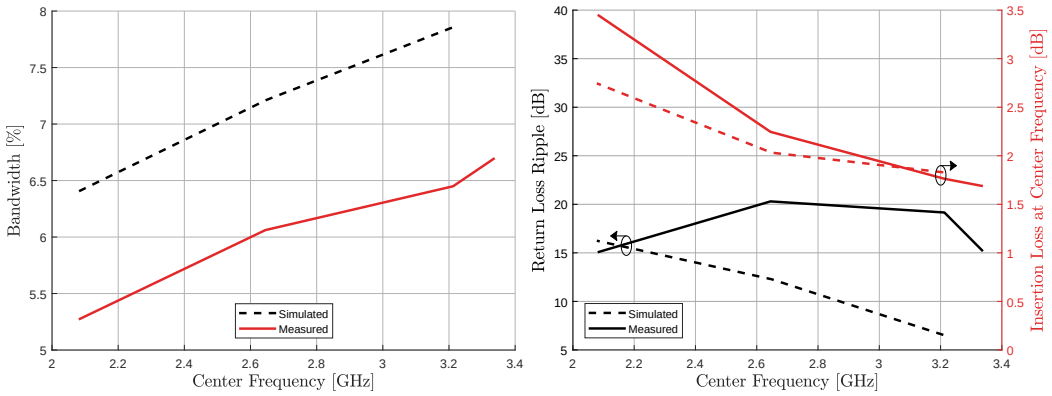

(a) (b)

Figure 4.8: Comparison of simulated and measured filter performance. (a) 15 dB bandwidth. (b) Return loss ripple and insertion loss.

The 15 dB bandwidth, return loss ripple, and insertion loss at the center frequency for the simulated and realized filters are compared in Figure 4.8. The bandwidth of the fabricated filter across the tuning range is closer to the design bandwidth of 6% than the simulated filter. This is due to the fact that the resonators

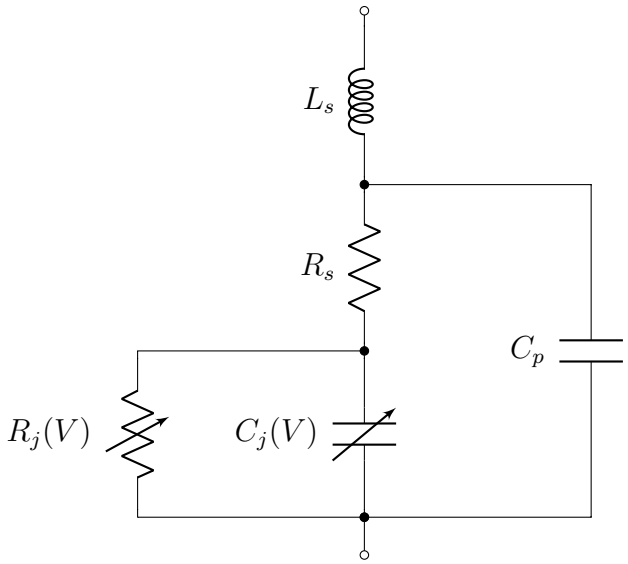

Figure 4.9: A more complete varactor model

were independently biased to control the coupling. The corrections to the coupling also resolved the decreasing return loss ripple seen in the simulations at high center frequencies.

The realized filter has lower insertion loss than the simulated filter at high center frequencies because the external coupling of the realized filter was tuned to control the flatness of the insertion loss response. However, the performance of the fabricated filter degrades at low frequencies to the extent that the filter specification is no longer met. In particular, the fabricated filter shows higher insertion loss than the simulated filter as the center frequency is tuned lower. This is due to the varactor diodes: the simple diode model discussed in Chapter 3 does not fully account for the varactors' behavior. A more complete model is shown in Figure 4.9 [52].

The series inductance L_s is due to the inductance of the metal contacts, the parasitic capacitance C_p is due to the packaging. The parallel resistance, $R_j(V)$, is the junction resistance [52]. Typically, this resistance is large under reverse bias and the series inductance and package capacitance are very small, so the simple varac-

tor model used in HFSS is sufficient [52]. However, as the varactor tends toward lower bias voltages, and therefore, large junction capacitances, the parallel resistance may become small enough to be non-negligible. When the capacitive loading of the filter is increased by lowering the bias voltage, the filter tunes to lower frequencies, which is where the insertion loss degrades the most. Thus, at low biases, the parallel resistance decreases and more energy is dissipated in the varactor, causing the insertion loss to increase. Despite the increased losses from the varactors, the fabricated filter better satisfies the return loss ripple and bandwidth specifications than the simulated filter due to the independent control over the internal and external coupling.

4.3 Measured Microstrip Patch Results

The return loss of the microstrip patch was measured using the same equipment and general setup as the combline filter. The ground plane of the patch was connected to the ground reference of the DC voltage source using an alligator clip. The same bias voltage was applied to both varactors, so the patch required only one bias voltage. The antenna patterns of the patch were measured in the far-field anechoic chamber at the RIL, and the antenna pattern measurements were used to calculate the gain of the patch using the gain transfer method. The reference antenna used for the gain transfer method was an ATM Microwave 150-441EM-NF standard horn with a nominal gain of 15 dB from 1-2.5 GHz. The standard horn's frequency response curve was used to graphically estimate the gain of the horn from 2-2.5 GHz [56]. The data used for the estimation is shown in Figure 4.10.

The gain was relatively constant at approximately 12.125 dB over that bandwidth, so this value is taken as the gain of the reference antenna in the gain transfer method calculations. Because the designs in this work can operate above 2.5 GHz,

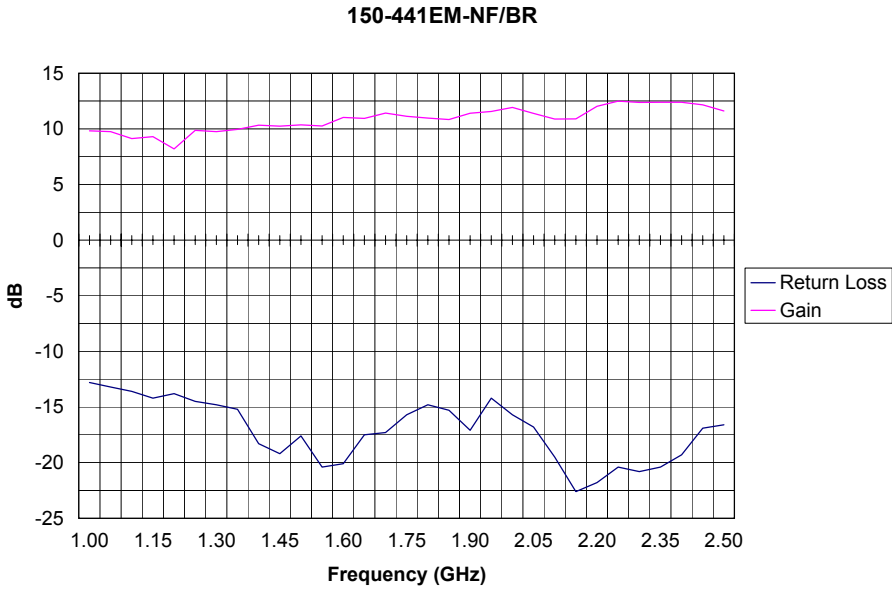

Figure 4.10: Typical data from standard gain horn [56]

any gain calculated above that frequency is contingent on the assumption that the horn has a flat gain response up to the highest frequency for which the gain is calculated. A comparison of the measured and simulated return loss and broadside gain of the patch is shown in Figure 4.11.

The measured return loss shows relatively good agreement with the simulated results over the tuning range of the patch, though the impedance matching of the fabricated antenna degrades more than the simulation indicated at higher center frequencies. This could be due to fabrication tolerances, as any change to the position of the coax probe can affect the impedance match. The 10 dB impedance bandwidth of the fabricated patch matches that in the simulation over much of the tuning range. The bandwidth, return loss at resonance, and gain of the simulated and realized patches as functions of center frequency are compared in Figure 4.12.

The impedance bandwidth of the fabricated patch is reduced at the highest center frequency due to the poorer impedance matching at that frequency. The return loss of the realized patch, like the simulated patch, decreases as the patch is tuned

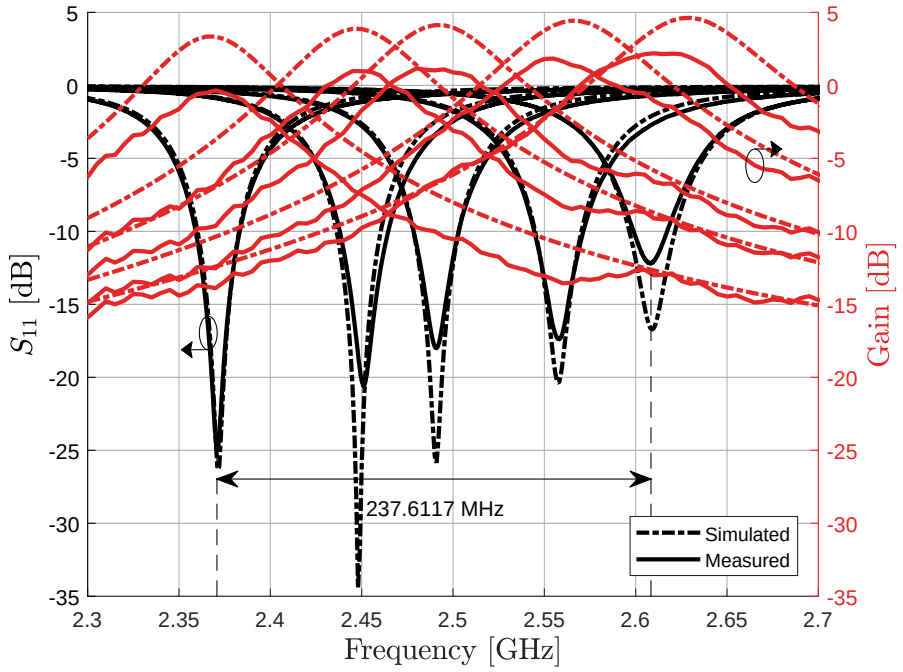

Figure 4.11: Comparison of simulated and measured patch return loss and broadside gain

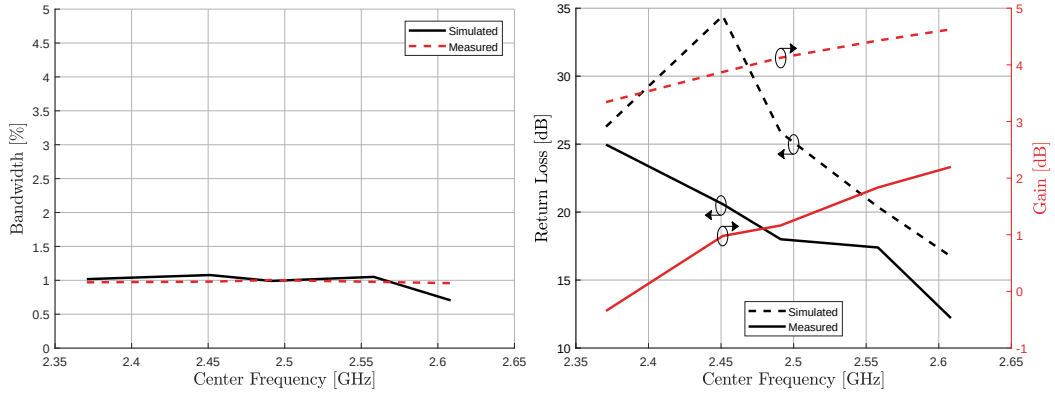

(a) (b)

Figure 4.12: Comparison of simulated and measured patch antenna performance as functions of center frequency. (a) Impedance bandwidth. (b) Return loss at resonance and gain.

toward higher center frequencies. The gain of the realized patch is lower than that of the simulated patch. For low center frequencies, this can be attributed to the additional losses in the varactors discussed previously. At higher frequencies, the

reduced gain could be a result of additional losses, such as RF current leakage into the DC biasing circuitry due to fabrication and component tolerances. The fabricated patch's tuning bandwidth is 237.6 MHz, or 9.54%. It should be noted that the fabricated patch was able to tune over a wider frequency range than that predicted by simulation, so additional simulations were run using loading capacitance values outside the varactor's nominal range to compare with the measured results.

For the antenna pattern measurements, the patch was mounted on a dielectric foam support with the DC power supply in a plastic frame below. RF absorbing materials were placed around the power supply an over the DC bias connection to prevent reflections from these components to the extent that this was possible. The pattern measurement setup is pictured in Figure 4.13.

The setup was mounted on the antenna positioner in the anechoic chamber, as shown in Figure 4.14, at which point the RF absorbing materials were placed on the sides of the DC source and on top of the DC cables. The measured antenna patterns are compared to the simulated patterns in Figures 4.15-4.19.

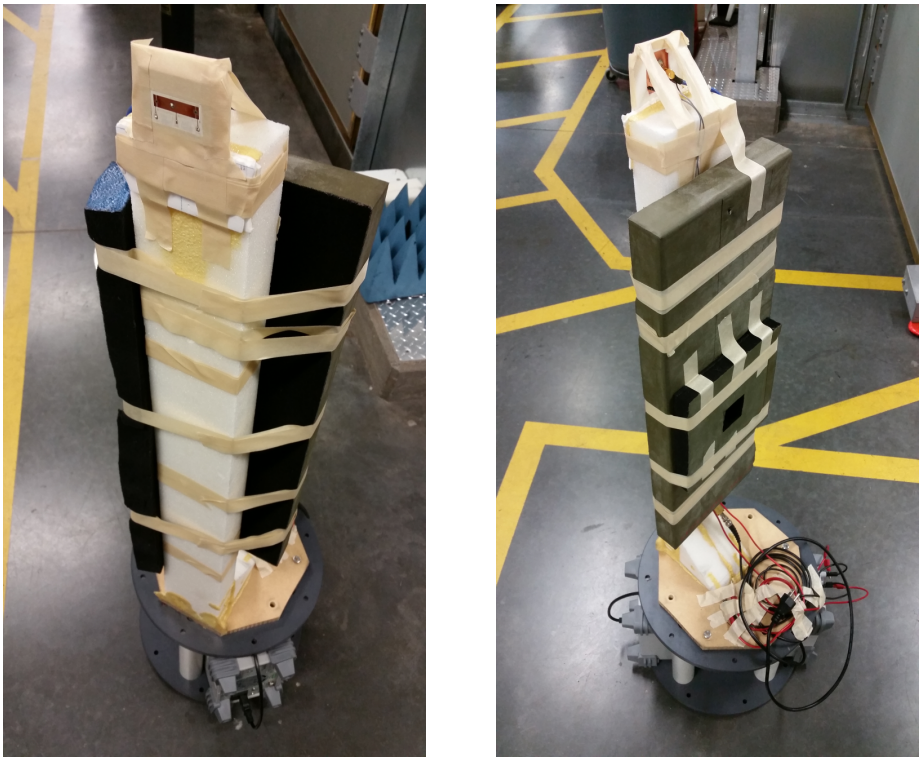

(a) (b)

Figure 4.13: Patch mounted on support structure with DC biasing circuitry. (a) Front view showing patch in E-plane measurement configuration. (b) Rear view showing absorber on dielectric post and DC cables.

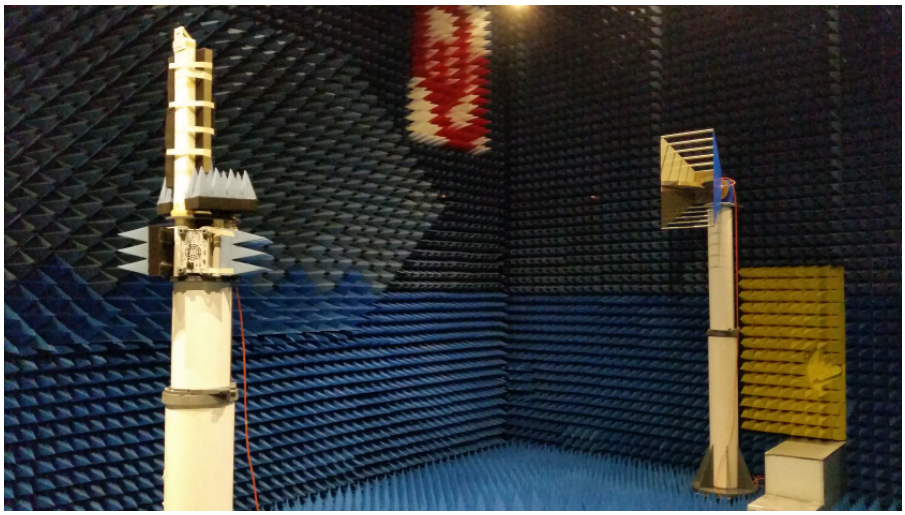

Figure 4.14: Patch antenna mounted on antenna positioner in the anechoic chamber

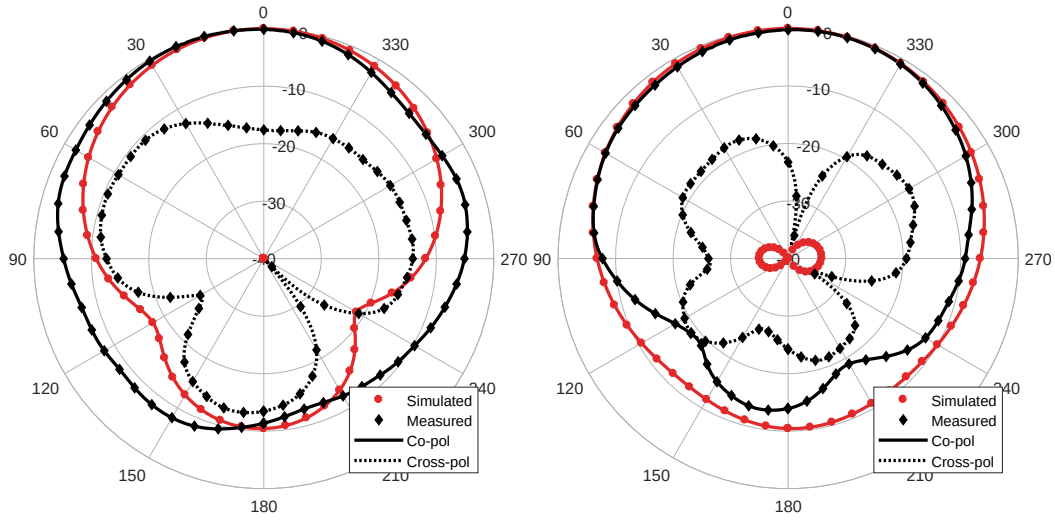

(a) (b)

Figure 4.15: Comparison of simulated and measured antenna patterns of microstrip patch tuned to f_0 = 2371 MHz. (a) E-plane patterns. (b) H-plane patterns.

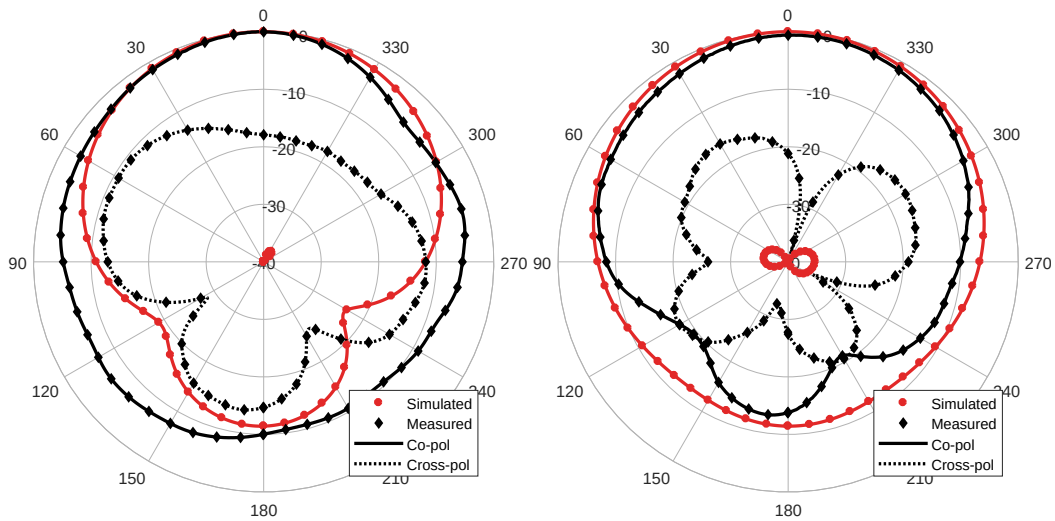

(a) (b)

Figure 4.16: Comparison of simulated and measured antenna patterns of microstrip patch tuned to f_0 = 2450 MHz. (a) E-plane patterns. (b) H-plane patterns.

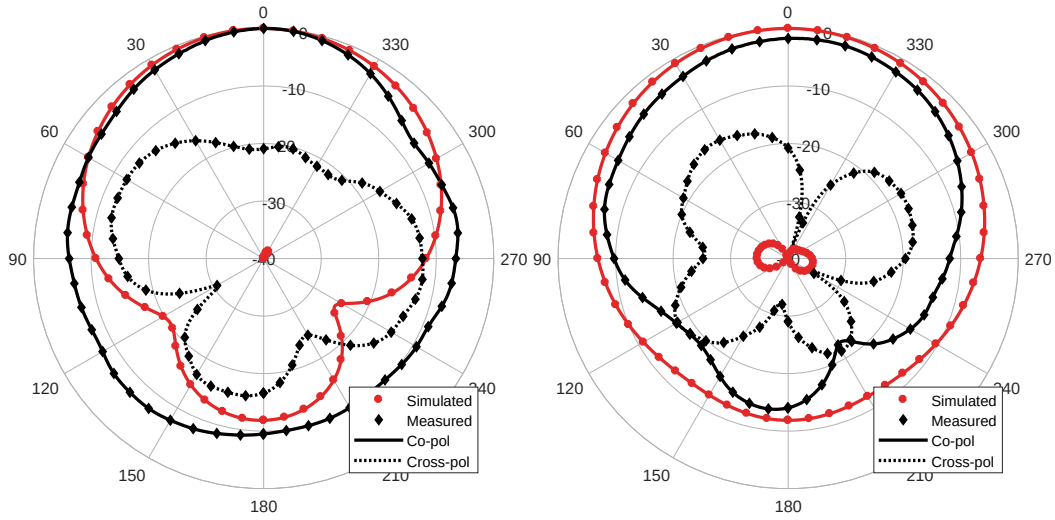

(a) (b)

Figure 4.17: Comparison of simulated and measured antenna patterns of microstrip patch tuned to f_0 = 2491 MHz. (a) E-plane patterns. (b) H-plane patterns.

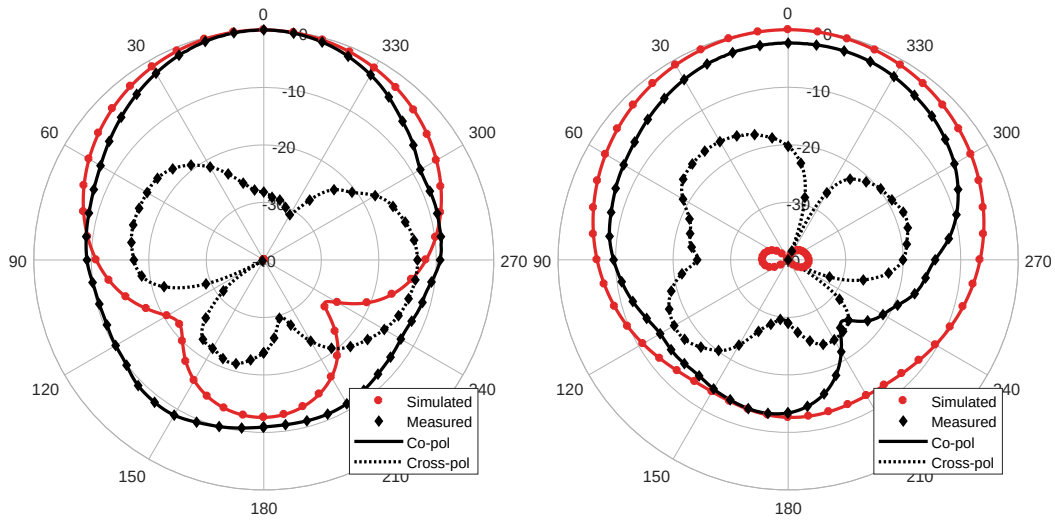

(a) (b)

Figure 4.18: Comparison of simulated and measured antenna patterns of microstrip patch tuned to f_0 = 2558 MHz. (a) E-plane patterns. (b) H-plane patterns.

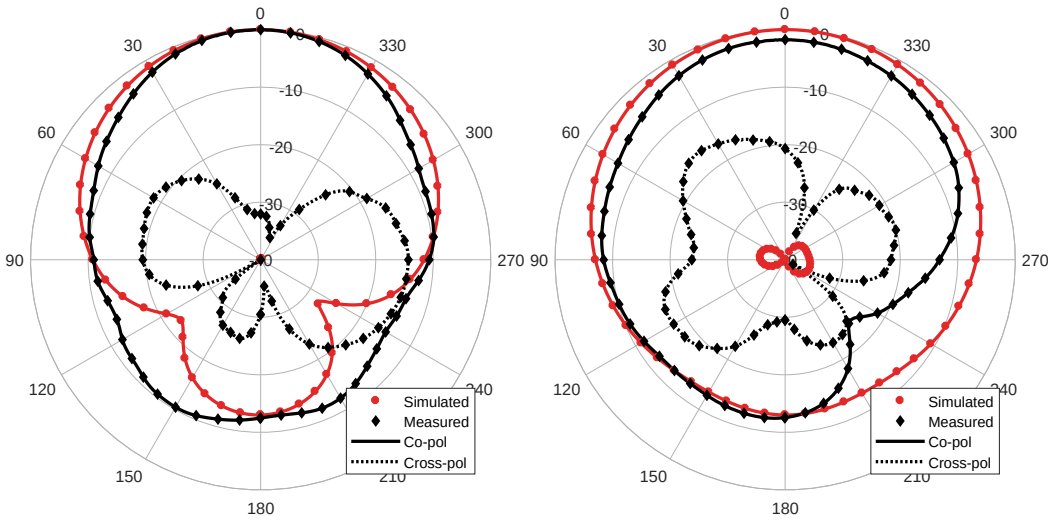

Figure 4.19: Comparison of simulated and measured antenna patterns of microstrip patch tuned to f_0 = 2609 MHz. (a) E-plane patterns. (b) H-plane patterns.

While there is general agreement between the simulated and measured patterns, there are discrepancies which arose from a number of causes. Any difference between the simulation model, which calculates the patterns of the antenna suspended in free space, and the measurement setup will introduce discrepancies. All of the factors that caused the discrepancies will be discussed in Section 4.4, as the same issues were observed with the measurement of the filtenna patterns. It should be noted that the measured patterns are less directive than the simulated patterns, which reduces the gain of the realized patch compared to the simulated patch, as was seen in Figure 4.11.

4.4 Measured Filtenna Results

The return loss of the filtenna was measured using the same equipment and a similar setup as the filter and patch. To tune the filtenna, the bias voltages of the input coupling line, resonator, and patch element were tuned independently. The same

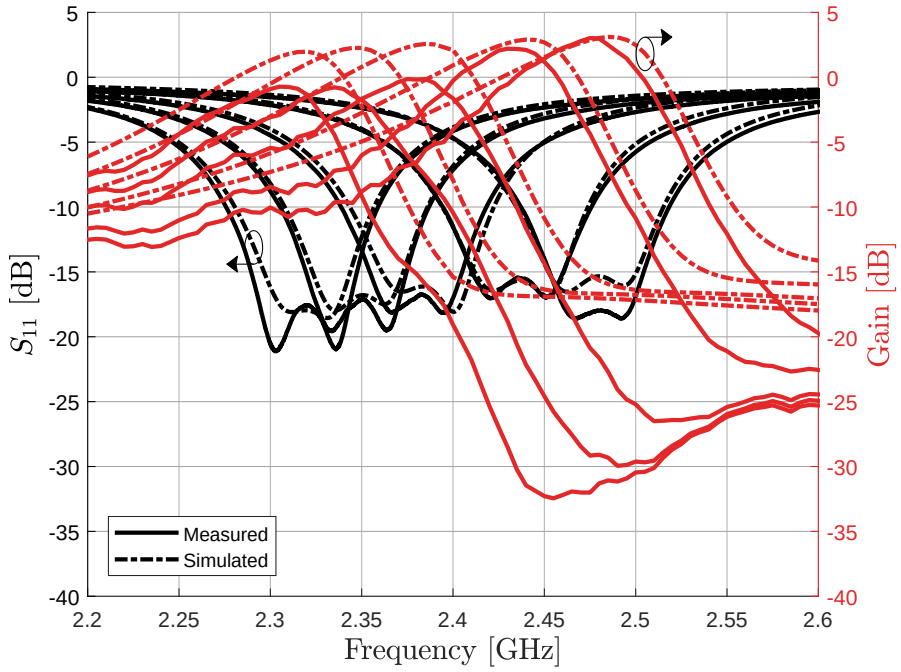

Figure 4.20: Comparison of simulated and measured filtenna return loss and gain

bias was applied to both of the varactors on the patch element in the filtenna design. The measured return loss and gain of the filtenna are compared to simulations in Figure 4.20.

The measured return loss compares well with the simulation results and exhibits better symmetry between the poles for most center frequencies. The fabricated filtenna achieves a 15 dB bandwidth that is slightly wider than the simulated results, varying from 2.05% to 2.49% over the tuning range. The measured gain agrees with the shape of the simulated gain, but shows peak values that are several decibels lower than the simulations at low center frequencies. This is due to the increased loss through the parallel resistance in the varactor diodes, as was observed with the reference patch antenna. The simulated and measured bandwidth and gain of the filtenna as functions of the center frequency are compared in Figure 4.21.

Because the simulated filtenna results did not use the full tuning range of the varactors, the full tuning range of the filtenna was determined by measurement. The

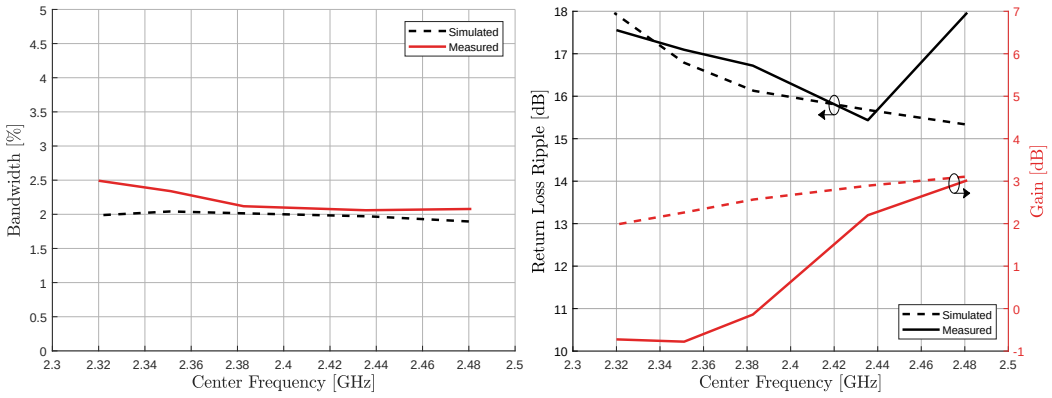

(a) (b)

Figure 4.21: Comparison of simulated and measured filtenna performance as functions of center frequency. (a) 15 dB bandwidth. (b) Return loss ripple and gain.

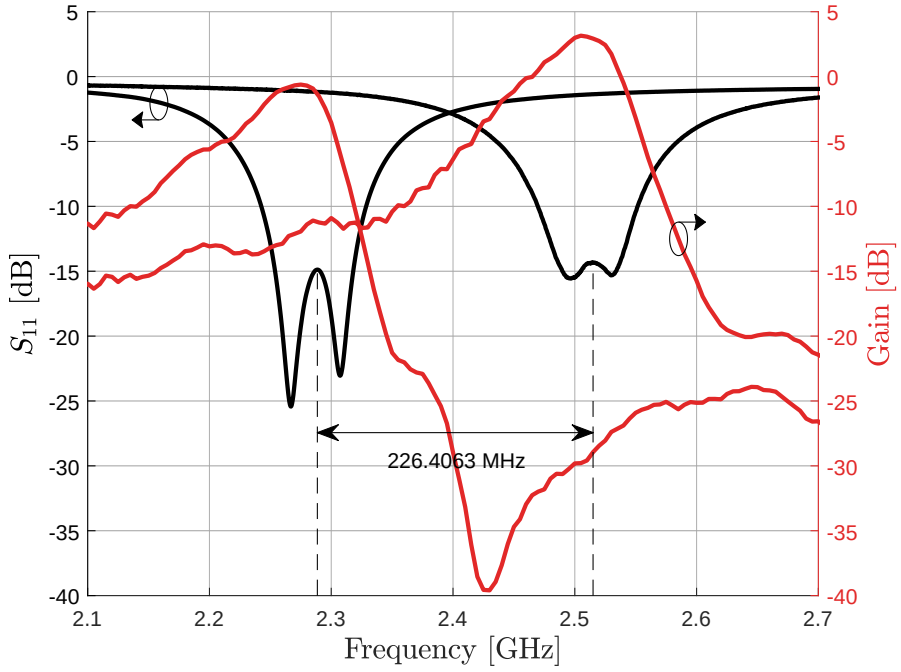

Figure 4.22: Full tuning range of the filtenna

limits of the filtenna's tuning are shown in Figure 4.22. As expected, the filtenna has a wider tuning bandwidth, 226.4 MHz or 9.43%, than predicted by the simulation. The filtenna tuning range is close to that of the patch, which was also expected as the range of the patch is the limiting factor among the tunable elements.

The antenna patterns of the filtenna were measured in the anechoic chamber using a similar setup as the patch. The filtenna mounted on its support structure is shown in Figure 4.23. The support structure was mounted on the antenna positioner system in the far-field chamber, as shown in Figure 4.24. The measured patterns are compared to the simulated patterns in Figures 4.25-4.29.

(a) (b)

Figure 4.23: Filtenna mounted on support structure. (a) Front view showing filtenna on dielectric support. (b) Rear view showing absorbing foam over DC cables on support and uncovered DC cables at base.

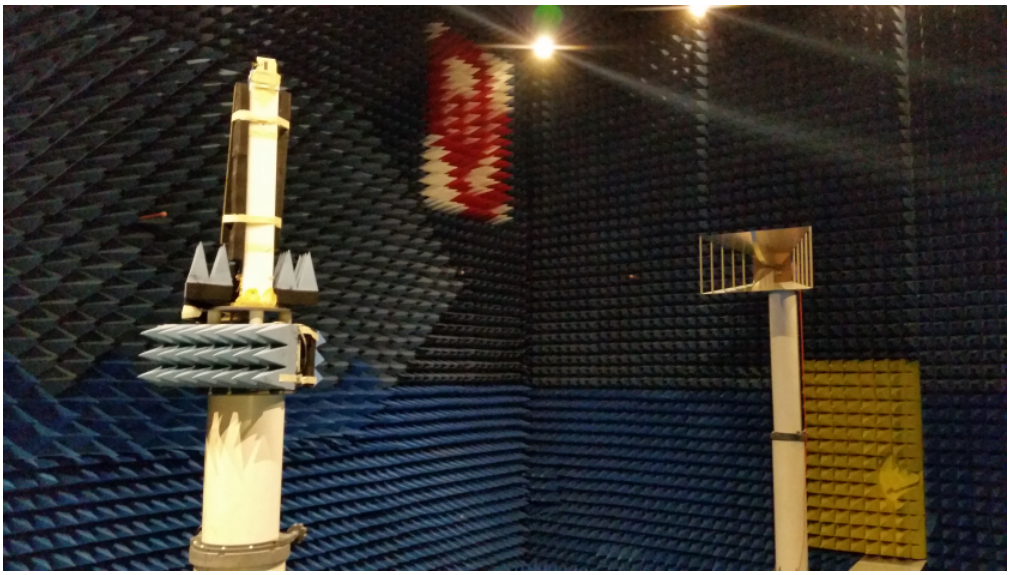

Figure 4.24: Filtenna mounted on antenna positioner in the anechoic chamber

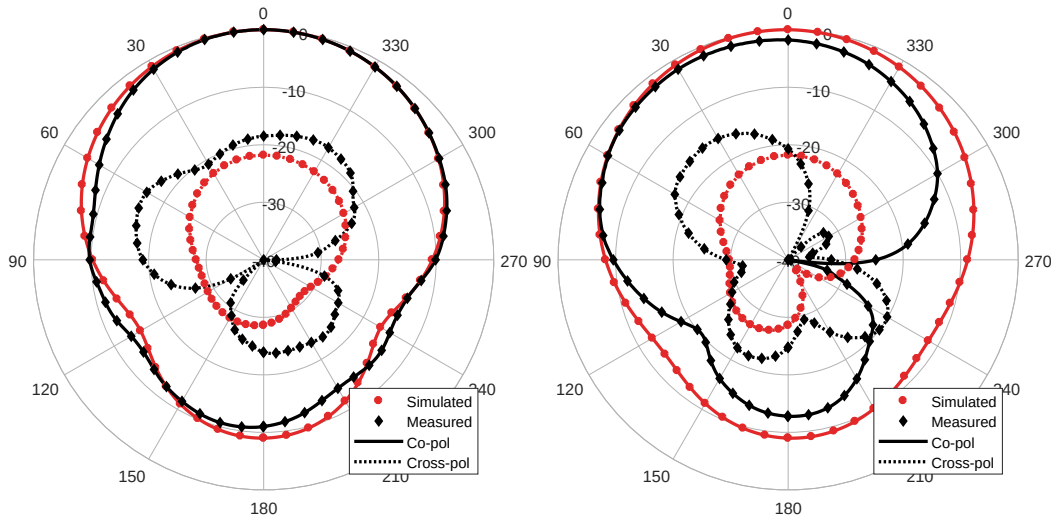

Figure 4.25: Comparison of simulated and measured antenna patterns of filtenna tuned to f_0 = 2319 MHz. (a) E-plane patterns. (b) H-plane patterns.

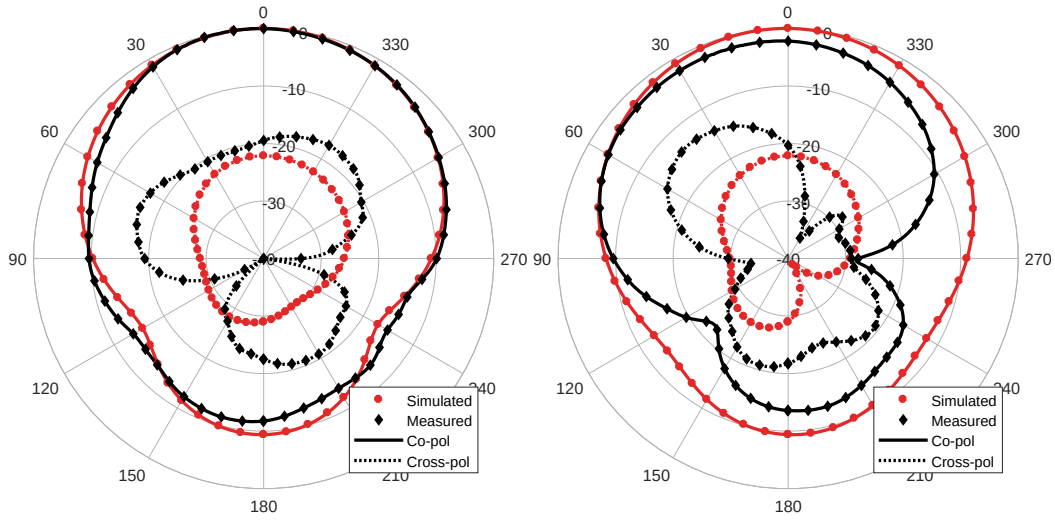

(a) (b)

Figure 4.26: Comparison of simulated and measured antenna patterns of filtenna tuned to f_0 = 2351 MHz. (a) E-plane patterns. (b) H-plane patterns.

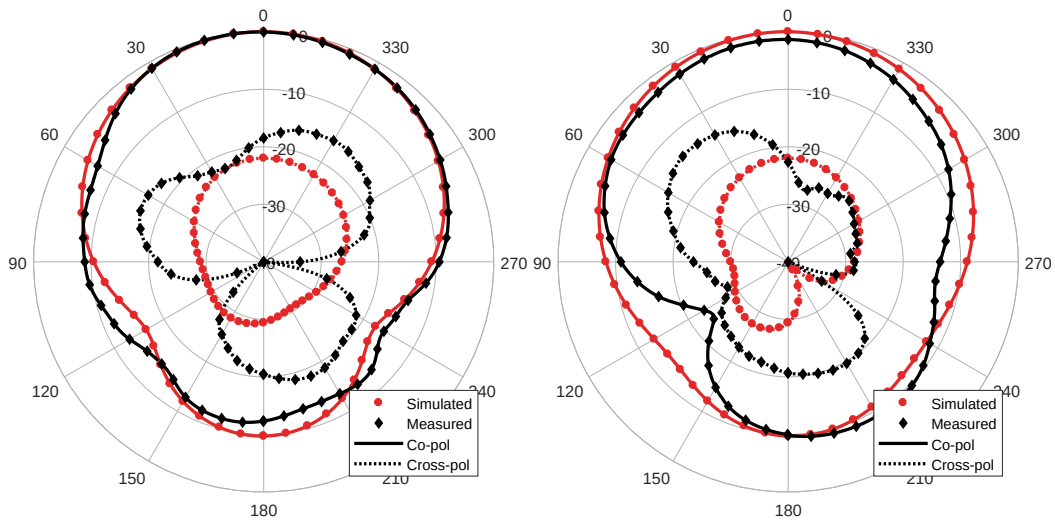

(a) (b)

Figure 4.27: Comparison of simulated and measured antenna patterns of filtenna tuned to f_0 = 2383 MHz. (a) E-plane patterns. (b) H-plane patterns.

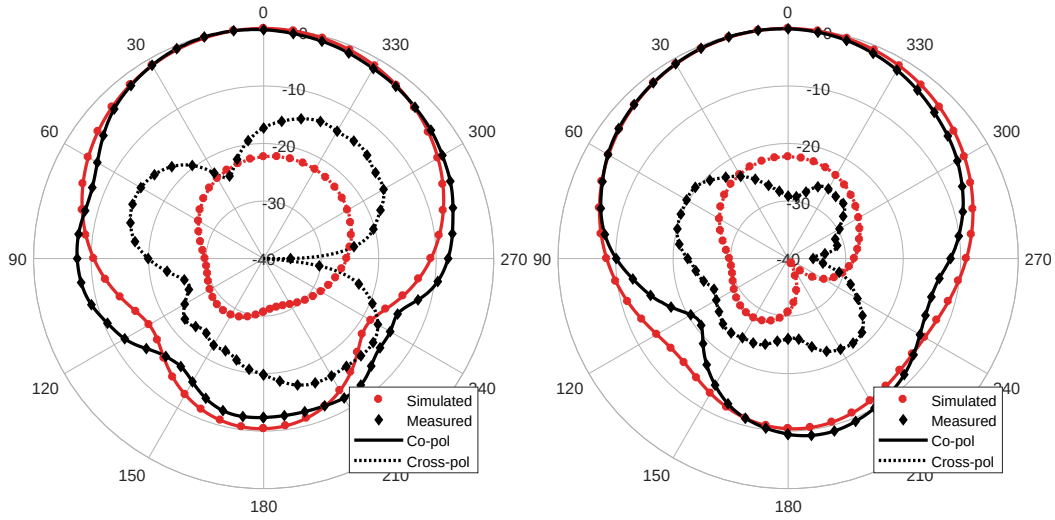

(a) (b)

Figure 4.28: Comparison of simulated and measured antenna patterns of filtenna tuned to f_0 = 2437 MHz. (a) E-plane patterns. (b) H-plane patterns.

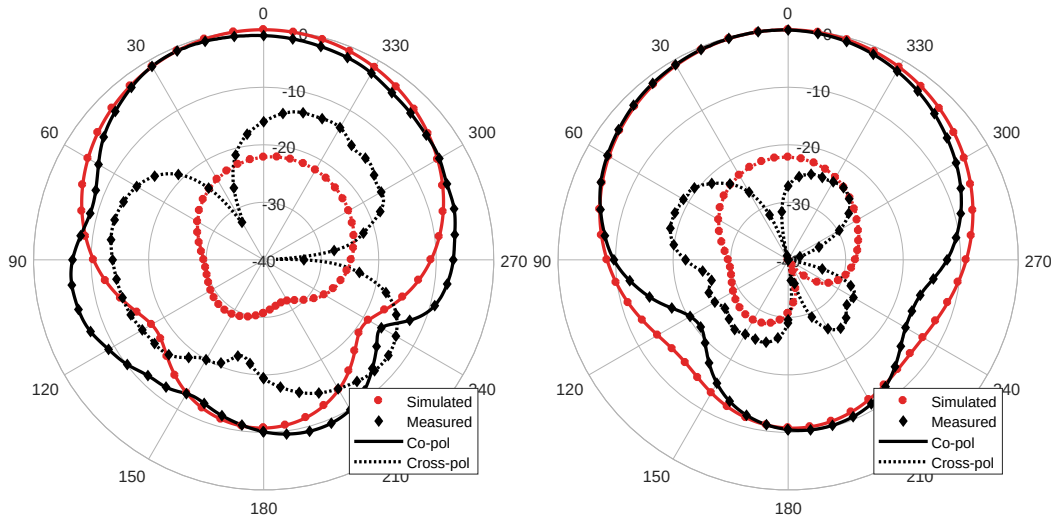

(a) (b)

Figure 4.29: Comparison of simulated and measured antenna patterns of filtenna tuned to f_0 = 2480 MHz. (a) E-plane patterns. (b) H-plane patterns.

As with the patch, the co-polarized patterns agree in general shape, but the cross-polarization is increased and shaped differently when compared to the simulation. A number of discrepancies between the simulation and the measurement caused these changes. The first issue was the presence of the DC power supply, which caused reflections that distorted the patterns, despite the RF absorbers covering the larger sides. Further, the RF absorbers used to cover the DC biasing cables also introduced discrepancies between the simulation and measurement, as they absorbed fields that contributed to the simulated patterns. Another factor was RF leakage from the connector between the chamber transmission line and the antennas. The leakage was small, so it primarily affected the cross-polarized patterns because they were on similar orders of magnitude as the leakage. The filtenna had an additional factor that did not severely affect the patch: the presence of the end-launch connector at the input feed side of the board. This connector was not modeled in the filtenna simulation, but it caused additional field disturbances, particularly in the H-plane of the filtenna, as the axial dimension of the connector was in this plane. Furthermore, it was determined after the measurements were complete that the dielectric foam used to support both the patch and the filtenna was not transparent in the S-band, but had a dielectric constant of $\epsilon_r \approx 1.6$. This also caused field disturbances that were not accounted for in the simulation. Finally, it is also possible that the patch and filtenna both de-tuned to some extent in the anechoic chamber. The return loss of the patch and filtenna was measured with a PNA on a lab bench and the bias voltages were recorded. When the patterns were measured, the same bias voltages were set for each center frequency, but the return loss was not verified in-situ. Thus, it is possible that the patch and filtenna were slightly off-frequency during the pattern measurements, which could contribute to the discrepancies.

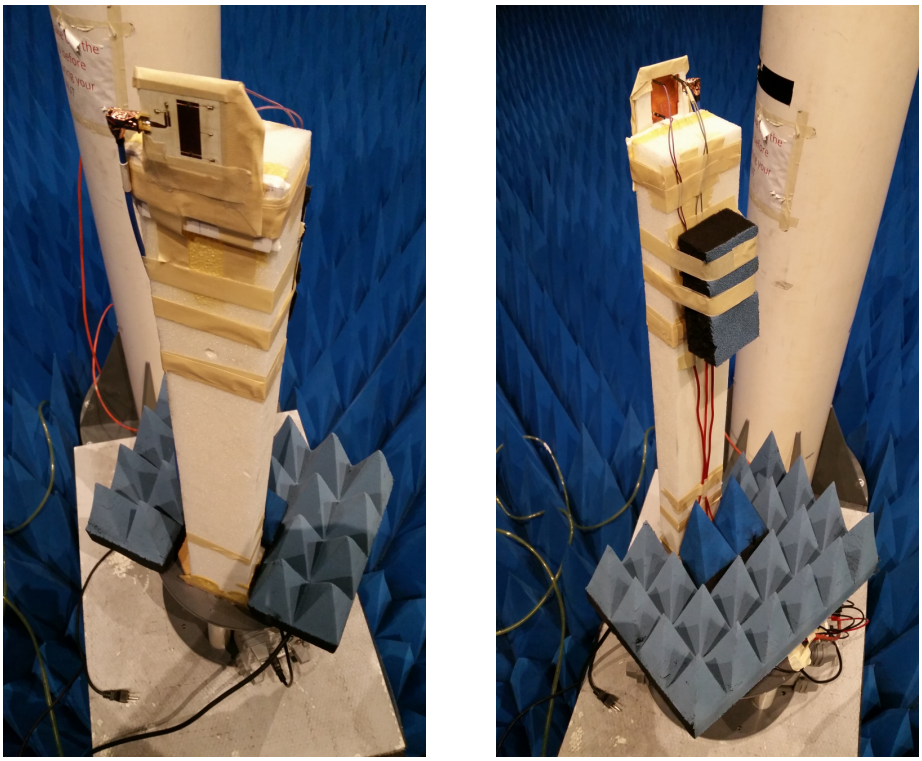

(a) (b)

Figure 4.30: Filtenna pattern measurement setup modified to reduce discrepancies between simulation and measurement. (a) Front view showing filtenna on dielectric support with copper tape on RF connector. (b) Rear view showing reduced absorbing foam on dielectric support.

To determine the impacts of some of these factors, the measurement setup was modified and the simulation model was updated. The RF absorbers were removed from the vertical antenna support structure, except for a small piece used to cover several large alligator clips in the DC bias circuit. The RF connector between the filtenna and the chamber cable was wrapped with copper tape to reduced the RF leakage. The modified measurement setup is shown in Figure 4.30, where both the change to the absorber configuration and the addition of the copper tape are visible.

The simulation was updated to include a cylinder of perfect electrical conductor to model the end-launch connector, as well as a dielectric post with the same di-

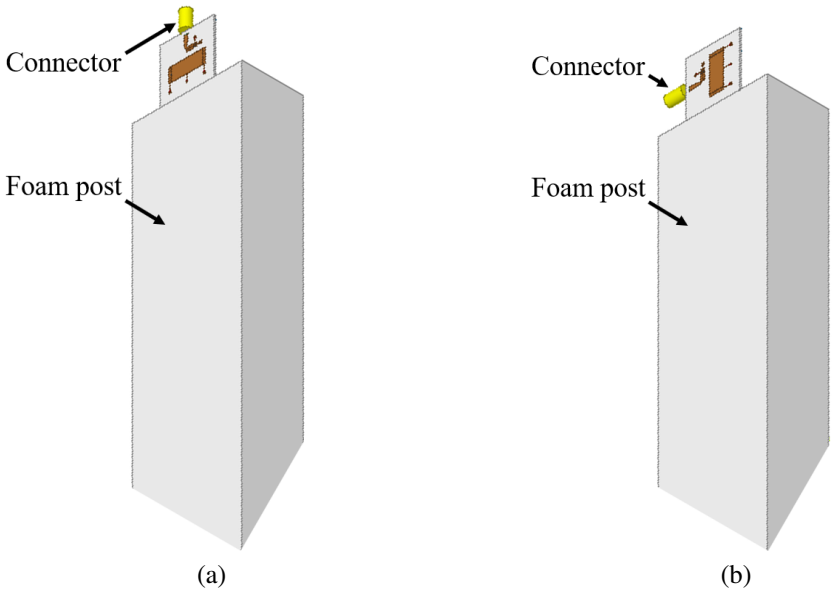

Figure 4.31: Filtenna simulation model with added end-launch connector and dielectric post. (a) Geometry for E-plane measurements. (b) Geometry for H-plane measurements.

mensions and dielectric constant as the foam support structure. The updated model is shown in Figure 4.31. Measured patterns were obtained using the modified setup for the filtenna tuned to 2480 MHz. The patterns were simulated for the same center frequency with the updated model. The results are compared in Figure 4.32.

The patterns from the modified setup and updated model show better agreement than the original measured and simulated patterns, indicating that the measured and simulated patterns could be brought into better agreement if new measurements were taken with further improvements to the setup, such as relocating the DC supply outside the chamber, and if the updated model was simulated for all center frequencies.

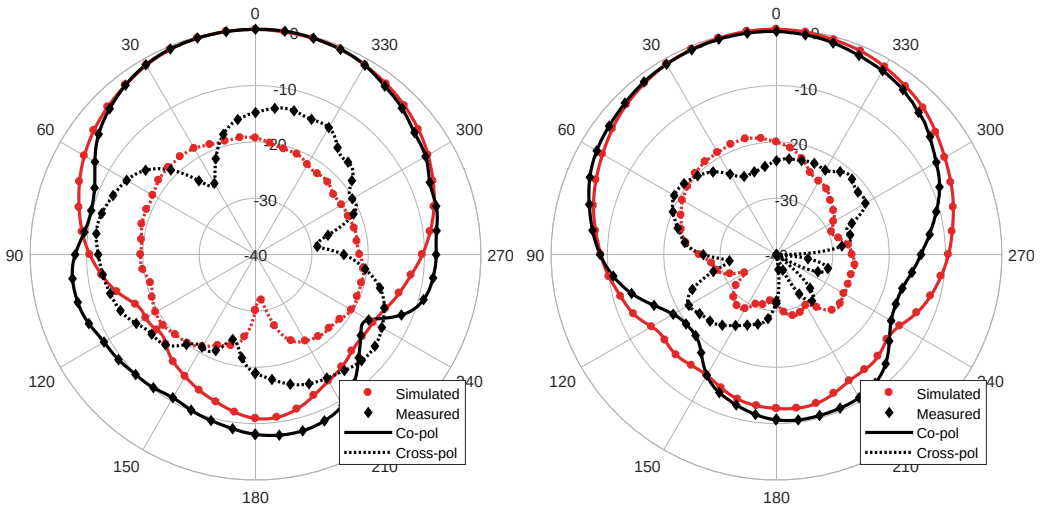

Figure 4.32: Comparison of simulated and measured patterns from modified measurement setup and simulation model with filtenna tuned to f_0 = 2480 MHz. (a) E-plane patterns. (b) H-plane patterns.

4.4.1 Comparison of Patch and Filtenna

The benefits of filtenna integration can be seen by comparing the performance of the reference patch to the filtenna. The measured impedance bandwidth of the patch and filtenna as a function of center frequency are compared in Figure 4.33. The measured 10 dB impedance bandwidth of the filtenna is approximately 3.3 times wider than that of the reference patch. This confirms the simulated results which indicated that the filtenna would provide increased bandwidth over the patch. While it is possible to increase the bandwidth of the patch by making it wider, this result shows that the bandwidth of the patch can be increased without increasing the size of the design, thereby helping to minimize SWaP-C.

The impedance matching and gain of the filtenna and patch as functions of center frequency are compared in Figure 4.34. To compare the impedance matching, the return loss of the patch at resonance is compared to the return loss ripple of the filtenna. The impedance matching of the patch degrades as the center frequency

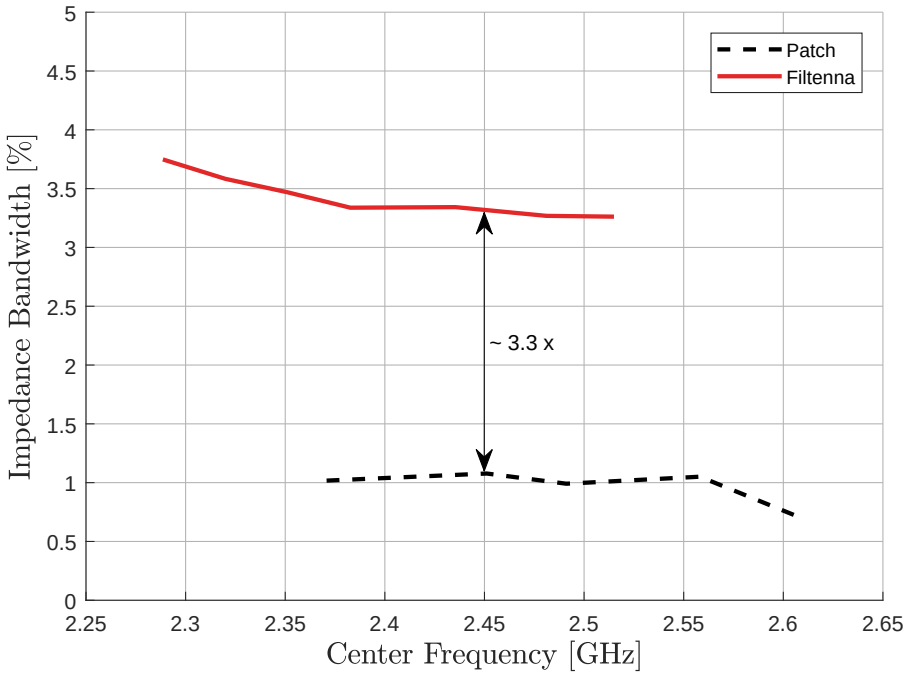

Figure 4.33: Comparison of measured patch and filtenna impedance bandwidths and gains as functions of center frequency

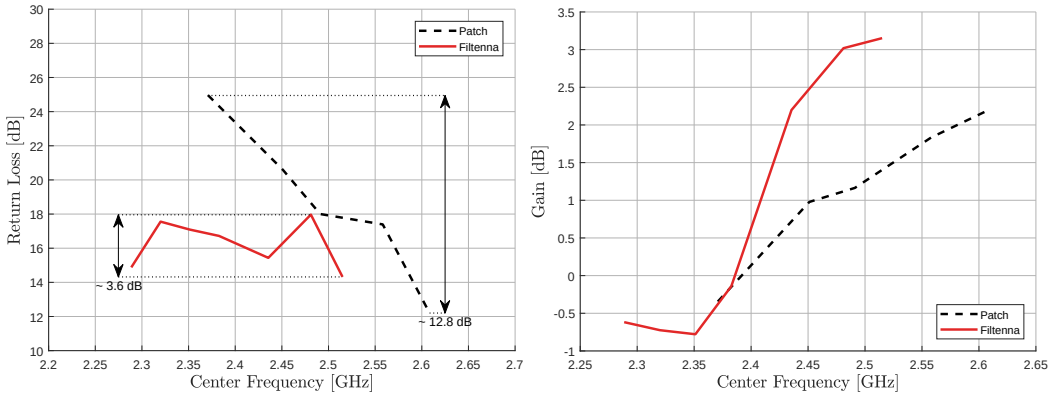

(a) (b)

Figure 4.34: Comparison of measured patch and filtenna performance as functions of center frequency. (a) Return loss. (b) Gain.

increases, varying by approximately 12.8 dB. However, the filtenna is able to maintain a relatively constant return loss across its tuning range, varying only 3.6 dB, which is 9.2 dB less than the variation in the patch. This is possible in the filtenna because of the extra degrees of freedom provided by the tunable resonator and input coupling: for a given resonant frequency of the antenna, the loading of the resonator and input line can be tuned to provide an improved impedance match.

The results presented here demonstrate that the original goal of designing a tunable filtenna for interference mitigation and cognitive radio applications has been achieved. The antenna element was successfully integrated with the filter elements such that the antenna provides a pole of the frequency response, thereby meeting the definition of a filtenna from the literature. The filtenna achieves a second-order response over its tuning range of approximately 9.43%. Compared to the reference patch antenna, the filtenna achieves a bandwidth approximately 3.3 times wider and reduces the variation in input impedance by 9.2 dB.

Chapter 5

Conclusion

This project aimed to design a filtering antenna with center frequency tuning in the S-band for interference mitigation and spectrum management systems. A design methodology was presented and a working filtenna model was created and simulated, along with a tunable filter and tunable antenna for comparison. The designs were fabricated and tested, and the measured results showed good agreement with simulated results, aside from some non-idealities which were accounted for and explained. The realized filtenna successfully integrated a microstrip combline filter resonator with a microstrip patch antenna to achieve a second-order response, thereby meeting the literature definition of a filtenna. The filtenna demonstrated center frequency tuning in the S-band with a tuning range of 226.4 MHz, making it, to the author's knowledge, the first fabricated and tested tunable filtenna. Relative to the reference patch antenna, the filtenna provides approximately 3.3 times wider impedance bandwidth and reduces the return loss variation by 9.2 dB across the center frequency tuning range. Thus, this design demonstrated increased bandwidth and impedance stability over the reference antenna, as well as center frequency tuning. This makes it a candidate for integration into cognitive radio systems to enable enhanced interference mitigation relative to wideband front-ends.

5.1 Future Work

There are several improvements that could be made to this design to increase its performance. The cross-polarization could be decreased by replacing the end-launch connector with a coax probe feed. This would place the connector in the backplane of the filtenna and prevent it from directly influencing the fields around the patch. Another possible modification would be to convert the filtenna to a multilayer design. This would constitute an almost complete re-design, as the resonator dimensions, biasing scheme, and internal and external coupling would all be affected. The filtenna could also be re-designed with an antenna element that has a larger frequency tuning range. This could be the segmented patch presented here with the segment cuts placed closer to the center of the patch, or a new antenna. The order of the filter response could be increased to achieve higher selectivity in the return loss and gain. As suggested by Dr. Jessia Ruyle, the use of a planar inverted F antenna (PIFA) would also be worth investigating, as the PIFA has the same structure as the combline resonators. Other future work would include resolving the issues encountered during the Q_{rad} extraction procedure. Finally, this design could be integrated into a cognitive radio system to perform its intended function of interference mitigation. The primary challenge of such a project would be the design of a control system that could continuously tune the filtenna to a specified center frequency, which involves adjusting the bias voltages on the input line, the resonator, and the patch independently. Thus, this project, while achieving its stated goals, provides several potential opportunities to improve the performance of the design and integrate the filtenna into practical systems.

Bibliography

[1] C. A. Balanis and P. I. Ioannides, *Introduction to Smart Antennas*, ser. Synthesis Lectures on Antennas 5. Morgan & Claypool, 2007.

[2] IEEE, "IEEE standard definitions and concepts for dynamic spectrum access: Terminology relating to emerging wireless networks, system functionality, and spectrum management", *IEEE Std 1900.1-2008*, pp. 1–62, 2008.

[3] K. Chang, *RF and Microwave Wireless Systems*. Wiley, 2000.

[4] A. Abbaspour-Tamijani, J. Rizk, and G. Rebeiz, "Integration of filters and microstrip antennas", in *Antennas and Propagation Society International Symposium*, IEEE Antennas and Propagation Society, IEEE, Jun. 2002.

[5] D. M. Pozar, *Microwave Engineering*, 4th. Wiley, 2012.

[6] F. T. Ulaby, E. Michielssen, and U. Ravaioli, *Fundamentals of Applied Electromagnetics*, 6th ed. Pearson, 2010.

[7] Y. Yusuf, H. Cheng, and X. Gong, "Co-designed substrate-integrated waveguide filters with patch antennas", *IET Microwaves, Antennas & Propagation*, vol. 7, no. 7, 2013.

[8] M. I. Skolnik, *Introduction to Radar Systems*. McGraw Hill, 2001.

[9] J. J. Lee, "G/T and noise figure of active array antennas", *IEEE Transactions on Antennas and Propagation*, vol. 41, no. 2, pp. 241–244, Feb. 1993, ISSN: 0018-926X. DOI: 10.1109/8.214619.

[10] C. K. Lin and S. J. Chung, "A compact edge-fed filtering microstrip antenna with 0.2 dB equal-ripple response", in *2009 European Microwave Conference (EuMC)*, Sep. 2009, pp. 378–380. DOI: 10.23919/EUMC.2009.5296108.

[11] Y. Yusuf and X. Gong, "A vertical integration of high-Q filters with patch antennas with enhanced bandwidth and high efficiency", in *2011 IEEE MTT-S International Microwave Symposium*, Jun. 2011, pp. 1–4. DOI: 10.1109/MWSYM.2011.5972721.

[12] J.-S. Hong, *Microstrip Filters for RF/Microwave Applications*, 2nd ed., K. Chang, Ed., ser. Wiley Series in Microwave and Optical Engineering. Wiley, 2011.

[13] J. T. Bernhard, *Reconfigurable Antennas*, ser. Synthesis Lectures on Antennas 4. Morgan & Claypool, 2007.

[14] C. G. Christodoulou, Y. Tawk, S. A. Lane, and S. R. Erwin, "Reconfigurable antennas for wireless and space applications", *Proceedings of the IEEE*, vol. 100, no. 7, pp. 225–2261, Jul. 2012.

[15] M.-C. Tang, Z. Wen, H. Wang, M. Li, and R. W. Ziolkowski, "Compact, frequency-reconfigurable filtenna with sharply defined wideband and continuously tunable narrowband states", *IEEE Transactions on Antennas and Propagation*, 2017, Accepted but not published as of 22 Aug. 2017. DOI: 10.1109/TAP.2017.2736535.

[16] Y. Tawk, J. Costantine, and C. G. Christodoulou, "A varactor-based reconfigurable filtenna", *IEEE Antennas and Wireless Propagation Letters*, vol. 11, pp. 716–719, 2012, ISSN: 1536-1225. DOI: 10.1109/LAWP.2012.2204850.

[17] A. H. Ramadan, K. Y. Kabalan, J. Costantine, Y. Tawk, and C. G. Christodoulou, "A tunable filtenna for cognitive radio applications", in *2015 9th European Conference on Antennas and Propagation (EuCAP)*, May 2015, pp. 1–2.

[18] M. Troubat, S. Bila, M. Thévenot, D. Baillargeat, T. Monedière, S. Verdeyme, and B. Jecko, "Combining of filtering and radiating functions for the design of X-band devices", in *11th International Symposium on Antenna Technology and Applied Electromagnetics [ANTEM 2005]*, Jun. 2005, pp. 1–4. DOI: 10.1109/ANTEM.2005.7852182.

[19] J. L. Durbin and M. A. Saed, "Tunable filtenna using varactor tuned rings fed with an ultra wideband antenna", *Progress In Electromagnetics Research Letters*, vol. 29, pp. 43–50, 2012.

[20] X. Gong, W. J. Chappell, and L. P. B. Katehi, "Embedded radiating filters in metamaterial substrates", in *IEEE Antennas and Propagation Society International Symposium. Digest. Held in conjunction with: USNC/CNC/URSI North American Radio Sci. Meeting (Cat. No.03CH37450)*, vol. 3, Jun. 2003, 351–354 vol.3. DOI: 10.1109/APS.2003.1219859.

[21] Y. Yusuf and X. Gong, "A new class of 3-D filter/antenna integration with high quality factor and high efficiency", in *2010 IEEE MTT-S International Microwave Symposium*, May 2010, pp. 892–895. DOI: 10.1109/MWSYM.2010.5516915.

[22] Y. Yusuf and X. Gong, "Compact low-loss integration of High-Q 3-D filters with highly efficient antennas", *IEEE Transactions on Microwave Theory and Techniques*, vol. 59, no. 4, pp. 857–865, Apr. 2011.

[23] ——, "Integrated filter/antennas with high efficiency and increased bandwidth", in *WAMICON 2011 Conference Proceedings*, Apr. 2011, pp. 1–4.

[24] W. L. Stutzman and G. A. Thiele, *Antenna Theory and Design*. Wiley, 2013.

[25] T. Li, K. Karnati, and X. Gong, "Approach to realize wide-scan-angle phased array with enhanced bandwidth and filtering function by using integrated filter/patch", in *2014 IEEE MTT-S International Microwave Symposium (IMS2014)*, Jun. 2014, pp. 1–3. DOI: 10.1109/MWSYM.2014.6848546.

[26] R. J. Mailloux, *Phase Array Antenna Handbook*, 2nd ed. Artech House, 2005.

[27] T. Li, H. Cheng, and X. Gong, "Integrated single-fed circularly-polarized patch antennas with high-Q cavity filters", in *2014 IEEE Antennas and Propagation Society International Symposium (APSURSI)*, Jul. 2014, pp. 1873–1874. DOI: 10.1109/APS.2014.6905263.

[28] R. Lovato and X. Gong, "A third-order high-Q SIW filter/antenna with two cavities and one integrated slot antenna", in *2016 IEEE International Symposium on Antennas and Propagation (APSURSI)*, Jun. 2016, pp. 1219–1220.

[29] C.-T. Chuang and S.-J. Chung, "Synthesis and design of a new print filtering antenna", *IEEE Transactions on Antennas and Propagation*, vol. 59, no. 3, pp. 1036–1042, Mar. 2011.

[30] C. T. Chuang and S. J. Chung, "A compact printed filtering antenna using a ground-intruded coupled line resonator", *IEEE Transactions on Antennas and Propagation*, vol. 59, no. 10, pp. 3630–3637, Oct. 2011, ISSN: 0018-926X. DOI: 10.1109/TAP.2011.2163777.

[31] M. Kufa, Z. Raida, and J. Mateu, "Three-element filtering antenna array designed by the equivalent circuit approach", *IEEE Transactions on Antennas and Propagation*, vol. 64, no. 9, pp. 3831–3839, Sep. 2016, ISSN: 0018-926X. DOI: 10.1109/TAP.2016.2586511.

[32] A. I. Abunjaileh, I. C. Hunter, and A. H. Kemp, "A circuit-theoretic approach to the design of quadruple-mode broadband microstrip patch antennas", *IEEE Transactions on Microwave Theory and Techniques*, vol. 56, no. 4, pp. 896–900, Apr. 2008, ISSN: 0018-9480. DOI: 10.1109/TMTT.2008.918137.

[33] H. M. Hizan, I. C. Hunter, and A. I. Abunjaileh, "Integrated siw filter and microstrip antenna", in *The 40th European Microwave Conference*, Sep. 2010, pp. 184–187. DOI: 10.23919/EUMC.2010.5616399.

[34] D. Wolansky, V. Hebelka, and Z. Raida, "Two-pole filtering antenna for body centric communications", in *2013 Loughborough Antennas Propagation Conference (LAPC)*, Nov. 2013, pp. 221–224. DOI: 10.1109/LAPC.2013.6711887.

[35] R. Lovato, T. Li, and X. Gong, "Electrically tunable integrated patch antenna with planar filter", in *2015 IEEE 16th Annual Wireless and Microwave Technology Conference (WAMICON)*, Apr. 2015, pp. 1–3. DOI: 10.1109/WAMICON.2015.7120365.

[36] G. L. Matthaei, L. Young, and E. M. T. Jones, *Microwave Filters, Impedance-matching Networks, and Coupling Structures*. Artech House Books, 1980.

[37] M. Dishal, "Alignment and adjustment of synchronously tuned multiple-resonant-circuit filters", *Proceedings of the IRE*, vol. 39, no. 11, pp. 1448–1455, Nov. 1951.

[38] D. G. Swanson Jr., "Narrow-band microwave filter design", *IEEE Microwave Magazine*, vol. 8, no. 5, pp. 105–114, Oct. 2007.

[39] J.-S. Hong, "Reconfigurable planar filters", *Microwave Magazine*, Oct. 2009.

[40] I. C. Hunter and J. D. Rhodes, "Electronically tunable microwave bandpass filters", *IEEE Transactions on Microwave Theory and Techniques*, vol. 30, no. 9, pp. 1354–1360, Sep. 1982.

[41] Y. Lian and S. Kumar, "Electronically tunable microstrip combline filter", *Canadian Journal of Electrical and Computer Engineering*, vol. 15, no. 3, pp. 123–128, 1990.

[42] G. Torregrosa-Penalva, G. López-Risueño, and J. I. Alonso, "A simple method to design wide-band electronically tunable combline filters", *IEEE Transactions on Microwave Theory and Techniques*, vol. 50, no. 1, pp. 172–177, Jan. 2002.

[43] A. Anand, J. Small, D. Peroulis, and X. Liu, "Theory and design of octave tunable filters with lumped tuning elements", *IEEE Transactions on Microwave Theory and Techniques*, vol. 61, no. 12, pp. 4353–4364, Dec. 2013, ISSN: 0018-9480. DOI: 10.1109/TMTT.2013.2287674.

[44] C. A. Balanis, *Antenna Theory: Analysis and Design*, 3rd. Wiley, 2005.

[45] J. J. Luther, S. Ebadi, and X. Gong, "Extraction of equivalent circuit model parameters of the feedless rectangular microstrip patch", in *2013 IEEE Antennas and Propagation Society International Symposium (APSURSI)*, Jul. 2013, pp. 302–303. DOI: 10.1109/APS.2013.6710812.

[46] A. Ludwig, "The definition of cross polarization", *IEEE Transactions on Antennas and Propagation*, vol. 21, no. 1, pp. 116–119, Jan. 1973, ISSN: 0018-926X. DOI: 10.1109/TAP.1973.1140406.

[47] I. Rouissi, J. M. Floc'h, H. Rmili, and H. Trabelsi, "Design of a frequency reconfigurable patch antenna using capacitive loading and varactor diode", in *2015 9th European Conference on Antennas and Propagation (EuCAP)*, May 2015, pp. 1–4.

[48] I. Rouissi, J. M. Floc'H, H. Rmili, H. Trabelsi, and A. Sharaiha, "Study of reconfigurable square patch antenna using capacitive loading", in *2014 Loughborough Antennas and Propagation Conference (LAPC)*, Nov. 2014, pp. 263–266. DOI: 10.1109/LAPC.2014.6996372.

[49] H. Tateno, S. Saito, and Y. Kimura, "A frequency-tunable varactor-loaded single-layer ring microstrip antenna with a bias circuit on the backside of the ground plane", in *2016 IEEE International Symposium on Antennas and*

Propagation (APSURSI), Jun. 2016, pp. 829–830. DOI: 10.1109/APS.2016.7696123.

[50] B. Babakhani and S. K. Sharma, "Investigations on frequency agile microstrip patch antenna loaded with varactor diode", in *2013 IEEE Antennas and Propagation Society International Symposium (APSURSI)*, Jul. 2013, pp. 664–665. DOI: 10.1109/APS.2013.6710992.

[51] R. B. Waterhouse and N. V. Shuley, "Full characterisation of varactor-loaded, probe-fed, rectangular, microstrip patch antennas", *IEE Proceedings - Microwaves, Antennas and Propagation*, vol. 141, no. 5, pp. 367–373, Oct. 1994, ISSN: 1350-2417. DOI: 10.1049/ip-map:19941305.

[52] K. Chang, *Microwave Solid-State Circuits and Applications*. Wiley, 1994.

[53] Skyworks, *SMV1405 to SMV1430 series: Plastic packaged abrupt junction tuning varactors*, http://www.skyworksinc.com/uploads/documents/SMV1405_1430_Series_200068V.pdf, Accessed 2017-05-12.

[54] B. Easter and R. J. Roberts, "Radiation from half-wavelength open-circuit microstrip resonators", *Electronics Letters*, vol. 6, no. 18, pp. 573–574, Sep. 1970, ISSN: 0013-5194. DOI: 10.1049/el:19700398.

[55] E. J. Denlinger, "Radiation from microstrip resonators (correspondence)", *IEEE Transactions on Microwave Theory and Techniques*, vol. 17, no. 4, pp. 235–236, Apr. 1969, ISSN: 0018-9480. DOI: 10.1109/TMTT.1969.1126937.

[56] ATM Microwave, http://www.atmmicrowave.com/wp-content/uploads/150-441-em-nf-br.pdf, 20 Nov. 2017.

Appendix A

List of Acronyms

- **AC** - alternating current
- **AUT** - antenna under test
- **DC** - direct current
- **HFSS** - High-Frequency Structure Simulator
- **LNA** - low-noise amplifier
- **MWO** - Microwave Office
- **PCB** - printed circuit board
- **PIFA** - planar inverted F antenna
- **PNA** - performance network analyzer
- **RF** - radio frequency
- **RIL** - Radar Innovations Lab
- **RLC** - resistor-inductor-capacitor
- **SIW** - substrate-integrated waveguide

- **SWaP-C** - size, weight, power consumption, and cost